

Block Copolymers beneath the Surface: Measuring and Modeling Complex Morphology at the Subdomain Scale

Abhiram Reddy, Xueyan Feng, Edwin L. Thomas,* and Gregory M. Grason*



Cite This: <https://doi.org/10.1021/acs.macromol.1c00958>



Read Online

ACCESS |



Metrics & More

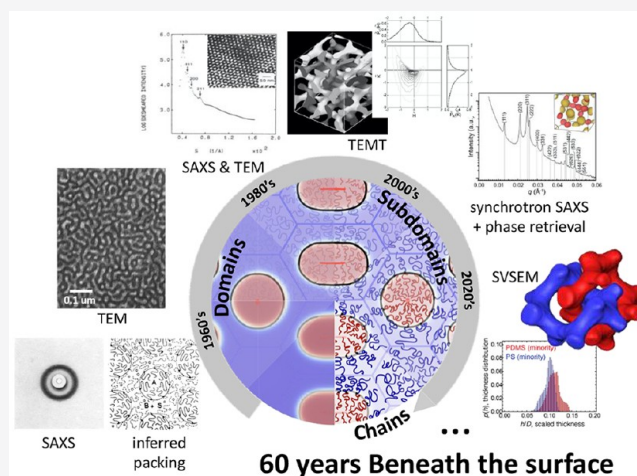


Article Recommendations



Supporting Information

ABSTRACT: Block copolymer (BCP) melts are a paradigm for pluripotent molecular assembly, yielding a complex and expanding array of variable domain shapes and symmetries from a fairly simple and highly expandable class of molecular designs. This Perspective addresses recent advances in the ability to model and measure features of domain morphology that go beyond the now canonical metrics of D spacing, space group, and domain topology. Such subdomain features have long been the focus of theories seeking to explain and understand mechanisms of equilibrium structure formation in block copolymer melts, from inhomogeneous curvatures of an intermaterial dividing surface to variable domain thickness. Quantitative metrics of variable subdomain geometry, or packing frustration, are central to theoretical models of complex BCP phase formation, from bicontinuous networks to complex (e.g., Frank–Kasper) crystals, and new experimental methods bring the possibility of their quantitative tests into reach. Here we not only review generic approaches to quantify local domain morphologies that both connect directly to thermodynamic models of BCP assembly but also generalize to domains of arbitrary shape and topology. We then overview experimental methods for characterizing BCP morphology, focusing on recent advances that make accessible detailed and quantitative metrics of fine features of subdomain geometry. Beyond even the critical comparison between detailed predictive models and experimental measurements of complex BCP assembly, validation of these advances lays the foundation to “mold” morphology in BCP assemblies at ever finer subdomain scale, through controlled architectures and processing pathways.



I. INTRODUCTION

Block copolymer (BCP) melts are a prototypical system for understanding and exploiting self-assembly in soft matter. The reasons for this are widely known and often celebrated. On one hand, their molecular design is versatile and extendable to seemingly limitless combinations of block chemistry, broadened by an array of architectural variations, all made accessible by advances in controlled polymerization techniques.^{1–3} At the same time, the thermodynamics that drive their assembly into fascinating and often useful nanostructured morphologies is generic, pitting the entropy of random-walking chain configurations against generic enthalpic tendencies to microphase separate unlike chemical units.⁴ Hence, a vast range of chemically distinct BCP systems can all be effectively mapped onto a common “universal” model whose equilibrium assembly is characterized by a relatively small number of effective parameters.⁵ The broad success of self-consistent-field (SCF) theory in accurately modeling observed BCP assembly, when combined with the array of experimental methods available for characterizing morphologies on the typical length scales of chains (~ 10 – 100 nm) and the ability to create precise

nanoscale structures for a host of technological applications^{6–8} (e.g., membranes, batteries, and lithographic templates), accounts in large part for the long-term and continuing research interest in BCP⁹ as a “laboratory for self-assembly”.¹⁰

Much progress has been made in the past six decades to understand the link between molecular structure and local interactions to the equilibrium patterns of BCP domains. Some of the earliest studies of BCPs^{11–17} used polarizing optical microscopy (POM), small-angle X-ray scattering (SAXS), and transmission electron microscopy (TEM) to show the existence of periodic nanostructured domains of alternating composition. These observations focused on somewhat coarse descriptions of the domain morphologies: their basic topologies and symmetric

Received: April 30, 2021

Revised: August 4, 2021

shapes of the intermaterial dividing surfaces (IMDS), i.e., the canonical layer-, cylinder-, or sphere-like domains; and the characteristic length scale of the alternating periodic pattern or *D*-spacing.

Early theoretical work pioneered by Meier,¹⁸ and more extensively by Helfand,^{19–21} developed statistical SCF approaches to probe the thermodynamics governing the selection of the size and shapes of the three canonical microphase-separated domains. These theories neglected, to a first approximation, the thermodynamics that determine multi-domain periodicity by, for example, assuming spherical domains occupy perfectly spherical volumes irrespective of their periodic arrangement, now known as the unit-cell approximation (UCA) of domains. Theoretically, a major breakthrough came with Leibler's weak-segregation mean-field theory for diblock melts near the order–disorder transition (ODT).²² Weak segregation is defined by the condition that the product of the Flory–Huggins parameter χ and degree of polymerization N is close to the mean-field ODT value of 10.495. Sufficiently close to the ODT, mean-field equilibrium morphologies are well approximated as superposed plane-wave modulations in compositions. As a reciprocal space approach, weak segregation theory provided a prediction of not only the optimal domain size and topology but also the periodic supradomain symmetry. For example, this theory predicts that 3D body-centered-cubic (BCC) and 2D hexagonal lattices are the thermodynamically stable arrangements of spherical and cylindrical domains, respectively, for linear diblocks melts near the ODT. Notably, this focus on the reciprocal space structure of domain morphologies is well suited to small-angle scattering studies of BCP morphologies. Indeed, comparing the ratios of the wavevectors of the first few reflections in a radially averaged scattering profile to what is expected for the radially averaged Fourier transform of 1D layers, hexagonal cylinders, and BCC spheres has become a primary, albeit indirect (and sometimes erroneous), means to assess the domain topology and shape, in the absence of direct real-space imaging.

The discovery of the bicontinuous double-diamond²³ phase (originally observed for star block copolymers and later re-examined and found to be the double gyroid²⁴) in the region of the phase diagram intermediate to lamella and cylinders complicated the overly simplistic picture of BCP morphologies as standard lattice packings of spherical, cylindrical, and layered objects. For one, the interpenetrating double-network topology of bicontinuous network morphologies—double-gyroid (DG), double-diamond (DD), and double-primitive (DP), the O70 and O52^{25,26}—is far more complex, with one domain (usually the matrix) forming an undulating, saddle-like layer surface “slab” that is interspersed between two intercatenated tubular networks (usually composed of the minority component) that meet in the n -valent connections (e.g., trivalent for DG). The highly complex geometry and topology of these domains pose challenges for properly identifying the morphology in SAXS and TEM experiments. Likewise, the subtle structure of these morphologies posed challenges to early theories that attempted, for example, to compare the thermodynamic stability of DG to DD.^{27–30}

As we detail below, BCP morphologies can be decomposed into a set of local molecular environments, each of which is composed of a narrow wedge-like volume with a tapered geometry, i.e., subdomains. Segregated blocks partition within each wedge into subregions of like material divided by a local patch of the IMDS, with the taper of wedge-like subdomains

reflecting the local curvature of the IMDS. Such wedge-like regions become arbitrarily narrow with increasing segregation strength (i.e., for large χN), which simultaneously drives down the IMDS area per chain, while increasing the domain thickness. Early theories treated the canonical morphologies in the UCA,^{21,31} layers, and perfectly symmetric cylinders and spheres, which can each be decomposed into a single subdomain shape. Unlike this simplistic picture, network morphologies, like the DG, cannot be described by a UCA and cannot be tiled by a single local molecular motif. Or put another way, even at the first level of approximation for network phases one necessarily needs a set of wedge-like volumes, shapes, and extensions that vary substantially within the domain in order that the structure occupy volume at constant density throughout the phase. This conflict between constant density and a thermodynamically preferred local BCP “shape motif” is commonly known as packing frustration.^{32–34}

Based on a picture put forward by Matsen and Bates,^{32,35} packing frustration has been posited to be fundamental to symmetry and topology selection of the bicontinuous network phases (and indeed, to some extent, for all nonlamellar phases). Specifically, it was proposed that the particular geometry of chain packing at the center of the nodal junctions between tubular domains in bicontinuous phases introduced regions of especially high stretching of the minority blocks and, further, that this degree of frustration can be intuitively connected to the number of struts joining at a node. In this picture, it is not possible to separate the effects of domain topology (i.e., 3-valent nodes for DG vs 4-valent nodes for DD) and crystallographic symmetry (i.e., body-centered cubic for DG vs primitive cubic for DD).

Not coincidentally, the role of packing frustration to select interdomain packing symmetry has also reemerged in the context of the discovery of complex sphere phases of BCP. Crystalline arrangement of space-filling BCP domains requires them to deform away from simple, perfectly symmetric shapes like idealized cylinders and spheres.³⁶ Heuristically, this has been pictured as domains that conform to lower-symmetry polyhedral cells^{33,37,38} that can tile the lattice without gaps, e.g., the Voronoi cells of the BCC or face-centered-cubic (FCC) lattice. It then becomes intuitive that BCP chains that stretch toward the edges and vertices (corners) extend further than the ones that stretch toward the faces of these polyhedral “cages”. Optimizing the free energy cost of this packing frustration in spherical domains has been linked to the stability of Frank–Kasper (FK) phases over the canonical BCC sphere phase, as observed in an ever increasing range of BCP systems.^{39–44} FK phases were first observed in intermetallic A–B alloys,^{45,46} and unlike the simpler BCC or FCC arrangements, these FK phases include multiple populations of sphere domains, each of which occupies a volume characterized by a distinct point group symmetry.³⁷ Theoretical models and SCF calculations predict that sphere-like domains in FK phases of BCP are indeed significantly warped away from spherical shape,^{38,47–50} leading to pronounced variations in the IMDS shapes and volumes of different domains. Crucially, much like arguments made for the stability of DG phases over other bicontinuous networks, theoretical arguments and models suggest that the optimal selection among competing crystalline arrangements of sphere domains can be cast in terms of minimization of the cost of packing frustration.^{33,34,38}

Packing frustration is intrinsic to structure and thermodynamics of complex BCP phases like triply periodic, bicontinuous

networks and low-symmetry sphere phases (not to mention the plethora of phases present in terpolymers or other more complex multiblock architectures²). This argues that a key aspect of the thermodynamic selection of the ordered BCP arrangement takes place at what we define as the subdomain scale, which is characterized by variations in the local shapes and thicknesses of domains. Notwithstanding its importance to BCP thermodynamics, packing frustration remains a somewhat poorly defined concept and one that is rarely, if ever, quantified by direct experimental study. This is all the more surprising since modern techniques of SCF theory have made detailed predictions for the spatial distributions of subdomain shape and shape variations of BCP domains for several decades. Even so, it has remained unclear precisely what are the essential metrics needed to capture packing frustration at the intradomain scale and how these might vary from one domain type to another (e.g., networks vs spheres). That is to say, for example, by what measures is the DG morphology “less frustrated” than its competitor the DD? And, even for a fixed domain topology like DG, by how much can measures of packing frustration and subdomain inhomogeneity vary with thermodynamic parameters like segregation strength, block composition, and chain polydispersity, not to mention nonequilibrium parameters like thermal or solvent processing? Experimental BCP morphologies are difficult to achieve in strict thermodynamic equilibrium, and the implications of nonequilibrium processing for the comparison of experimental measurements to idealized symmetries and shapes of equilibrium domains computed by theory remain relatively poorly understood.

Even more problematic than this definitional ambiguity of meaningful measures of frustration is the fact that most experimental probes of BCP morphology are inadequate for capturing structural variations at the subdomain scale needed to connect to any theoretical definition. Characterization of frustration and subdomain variation in complex phases requires 3D real-space data, with resolution on length scales smaller (by a factor of about 5) than the domains themselves and is therefore typically on the order of a few nanometers. Simultaneously, to distinguish between intrinsic variation in an “ideally formed” structure (i.e., as predicted by SCF) and inevitable spatial fluctuations away from that ideal form requires experimental characterization to be performed over statistically large and meaningful sample volumes and without distortions that are specific to its processing pathway.

In this Perspective, we revisit the concept of packing frustration and the notion of subdomain morphology in BCP assemblies more broadly. Our aim is, first, to describe recent advances for defining generic and thermodynamically meaningful metrics of subdomain morphology, which in principle allow one to extract information about the distribution of molecular environments in an arbitrary BCP phase. We focus on features of the local shape of BCP packing, as characterized in the surface geometry and topology of the IMDS, as well as metrics of the domain thickness and corresponding chain extension that quantify entropic costs of uniformly filling BCP domains. Second, we aim to survey experimental approaches to characterize BCP morphology and their ability to extract quantifiable measures of packing frustration and subdomain morphology at the level of resolution needed to compare to and test theoretical models. The explosion of recent interest in molecular shapes and packing mechanisms that promote FK phases, as well as the long-standing interest in the factors that give rise to bicontinuous networks in BCP and soft matter more

broadly, argues that a better, more quantitative, approach to frustration may be the key to unlocking a host yet undiscovered morphologies and engineering their features at an ever finer subdomain size. For the purposes of clarity, most of the discussion will focus on understanding subdomain considerations for the simplest class of molecules, namely linear diblock copolymers, although clearly extensions of these concepts and methods have application to more complex chain architectures and compositions, as we briefly highlight at the end of this Perspective.

The remainder of this Perspective is organized as follows. In [section II](#), we give an overview of metrics of subdomain morphology, focusing first on the measures of variable IMDS geometry, and then approaches to quantify domain thickness and chain extension. As examples, we will primarily illustrate these metrics and their corresponding thermodynamic interpretation using domain structure from SCF predictions, but we will also give examples where the same metrics can be applied to experimental data. In [section III](#), we describe various experimental approaches to quantifying subdomain morphology, beginning with early characterization approaches to the gross morphological signatures of BCP, and, in particular, focus on recent advances and newly developing techniques for capturing yet unmeasured aspects of chain packing in experimental systems. In [section IV](#), we discuss some key challenges for quantifying and predicting morphological features of BCP assembly at the subdomain scale. In [section V](#), we conclude with some remarks about frontiers for extending our view of and control over of subdomain features of BCP morphologies to an ever finer and quantitative scale. Finally, we note that the [Supporting Information](#) provides a description of algorithms used to compute local thicknesses via the medial analysis described and implemented below for BCP data sets (both computational and experimental), with the software available at an online repository via [10.7275/vqe1-sm17](https://doi.org/10.7275/vqe1-sm17).

II. METRICS OF SUBDOMAIN MORPHOLOGY AND CHAIN PACKING

II.A. Subdomain Decomposition of Morphology: Preliminaries. In this section we overview geometrical concepts for measuring the morphologies of BCP assembly at the subdomain scale. In particular, we focus on metrics of the morphology that capture variation in the local packing environment of different chains. While lamellar morphologies permit uniform subdomain shapes, all other morphologies, namely complex morphologies such as bicontinuous networks and low-symmetry sphere packings, require variation of subdomain motifs.³⁴ For the purposes of clarity, we focus primarily on the case of linear AB diblock copolymers (dBCP), although, as we highlight in the conclusion, these concepts generalize to the considerably larger class of phase morphologies for more complex block and multiblock architectures. Our aim is to describe the key geometrical features of the BCP domain shapes that carry information about the thermodynamics of their melt assembly and the consequences of packing frustration.

Our perspective is largely informed by the strong-stretching limit (SSL) of dBCP melts.³¹ This is a theoretical limit of the SCF mean-field theory in which segregation strength is taken to be infinitely large, or formally, it is an asymptotic limit of SCF as $\chi N \rightarrow \infty$.^{51,52} The SSL was developed by Semenov^{30,31,53–56} and advanced by Milner^{27,29,57} and others⁵⁸ in its application to BCP domains and polymeric brushes more broadly. It has the great conceptual advantage of reducing the BCP thermody-

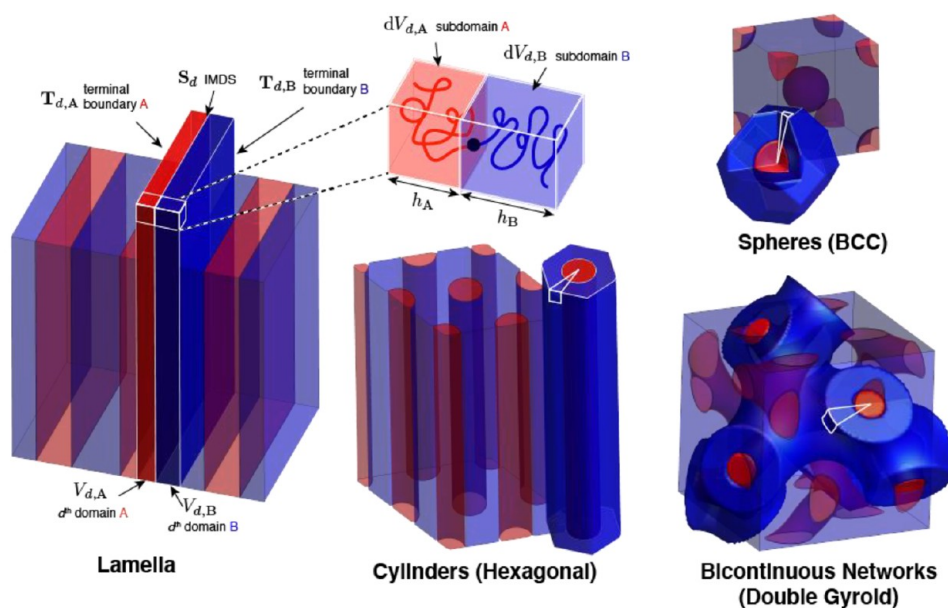


Figure 1. Domains and subdomains of BCP morphologies. The four most common domain topologies of AB diblock copolymers: lamella, cylinders, spheres, and bicontinuous networks. Each topology is shown in terms of a spatially periodic pattern of compositions with red/blue highlighting spatial regions where the local majority composition in A/B segment type, and boundaries between these A- and B-rich regions are separated by intermaterial dividing surfaces (IMDSs), which also defines the positions of junctions between blocks. A single domain, the volume corresponding to chains that associate to a common IMDS, is highlighted as an opaque region of each morphology. Each domain is further subdivided into a series of subdomains, which correspond to the infinitesimal, wedge-like, volumes of chains that associate to a common point (or patch) of the IMDS, highlighted in white in each case. The collection of subdomains are composed of brush-like domains extending away from the IMDS up to the terminal boundaries, surfaces which delineate the contact between opposing domains (or subdomains). Although opposing brushes always interpenetrate to some degree, the terminal boundaries can nevertheless be defined as 2D surfaces in terms of the boundaries of the association map that describes the probability of a chain segment passing through a given point having its junction associated with points on the IMDSs.

namics to a largely geometric competition between two physical effects: surface energy between unlike blocks and entropic costs of chain stretching. In the SSL, the interfaces between unlike domains, which we call intermaterial dividing surfaces (IMDSs), become arbitrarily narrow in comparison to the domain size. The relatively large cost of interblock repulsions in this limit causes chains to crowd the IMDS at high density to reduce the (lateral) area per chain exposure to unlike blocks.⁵ Because the melt maintains a constant density, high areal density at the IMDS leads to brush-like domains composed of highly stretched blocks on either side of the IMDS. Analysis of the entropy of these brush domains is simplified by large block extension because it implies that, to a first approximation, fluctuations around the statistically dominant configuration, the “classical trajectory”, can be neglected.⁵¹ Likewise, the effect of interpenetration between the “tips” of opposing like-polymer brushes on the SSL domain free energies can be ignored at this same level of approximation.⁵⁹ Of course, both approximations can be relaxed, and their effects may be systematically incorporated as one in a series of corrections to the SSL.^{51,52,54} A salient feature of SSL is that it facilitates thermodynamically precise and quantitative definitions of “chain packing”, which might otherwise be considered vague, or purely heuristic, concepts.

While metrics of subdomain morphology are perhaps best framed by the SSL theory of dBCP, in this discussion we aim to present these geometrical measures in a way that applies to realistic physical scenarios, notwithstanding the limiting and often unrealistic approximations of this theoretical idealization. Notably, we overview geometrical abstractions of the BCP domains that can be applied to real systems, given morphological data at the suitable scale and resolution. In section III, we

will focus on the requirements needed and available experimental techniques for acquiring such data. Our primary assumption is that the microphase-separated melt morphology can be characterized in terms of a set of composition fields $\phi_\alpha(\mathbf{x})$ that describe the mean local volume fraction of monomer type α at point \mathbf{x} throughout the 3D volume of the melt (e.g., for linear AB diblocks $\alpha = A$ or B). This type of data is readily available from numerical SCF computations^{50,60} or suitably coarse-grained simulations of chain models. Additionally, it can be inferred to some extent from measurements of image contrast in various electron microscopy techniques or other approaches (see section III).

Before proceeding to describe metrics of subdomain morphology, we first define the key terminology and geometric objects that are used in our characterization. While notions of “domain shape” and “packing frustration” are widely employed in discussions of BCP morphology, they are typically invoked somewhat vaguely and often in rather qualitative terms or instead overly specific scenarios whose generalizations to other situations (e.g., morphologies) remain unclear. For example, what is meant when we describe the “thickness” of a domain in the bicontinuous DG morphology? With this context in mind, we define subdomain morphology in specific terms that (i) can, in principle, be characterized quantitatively by physical observables, (ii) provide a meaningful connection to the underlying chain packing thermodynamics, and (iii) can be generalized to morphologies of arbitrary shape and topology.

For the purposes of this discussion, we describe this analysis as a subdomain decomposition of BCP morphology. This decomposition is summarized schematically in Figure 1. The essential idea is to divide up a physical configuration of

microphase-separated BCP melts into distinct and specific regions (volumes), whose geometry can be analyzed via quantitative metrics that correlate directly with the free energy of chain packing in those structures and its local variation throughout a given morphology. At the coarsest level, this begins by dividing a BCP melt into distinct domains, a term which we give a specific topological meaning. Domains are volumes occupied by the dBCP chains (both components) that all associate to a common IMDS. We then further refine this definition to a pair of subdomains as the volumes occupied by the respective dBCP blocks that associate to a specific point (i.e., an infinitesimal areal patch) on the IMDS.

Operationally, the subdomain decomposition can be performed as follows. Given a microphase-separated BCP melt within some predefined total volume V , the set of IMDSs of the domains may be determined from the level sets of the composition fields. Specifically, for an AB dBCP, these are the 2D sets of points S_d where the unlike composition fields are equal, $\phi_A(S_d) = \phi_B(S_d) = 1/2$. While this condition strictly may not be satisfied for extremely weakly segregated melts (e.g., for which the notion of IMDS not well suited), it is achieved under practically all experimentally relevant conditions where BCP microdomains form. Depending on the assembly topology, e.g., whether cylinders, layers, spheres, or networks, these IMDSs will split into a set of M disconnected surfaces, $S_{d,i}$ which we then can label with the domain index $d = 1, \dots, M$, according to each connected surface in V . Hence, there is one domain for every sphere and cylinder in the assembly, while notably, each lamellar “double layer” corresponds to two domains by this count. Given the set of IMDSs, we can define volumes $V_{d,A}$ and $V_{d,B}$ associated with A and B portions of domain d as follows (see Figure 1). The domain volume $V_{d,i}$ corresponds to the set of points such that $\phi_i(\mathbf{x}) > 1/2$ (i.e., \mathbf{x} is in a i -type “brush” region), and the AB junctions of chains passing through \mathbf{x} are the most likely to lie on S_d among all IMDSs. In this sense, we refer to the points $\mathbf{x} \in V_{d,\alpha}$ as associated to the common IMDS at S_d . The union of $V_{d,A}$ and $V_{d,B}$ then defines the d th domain of the melt.

A subdomain can be defined by choosing a point $\mathbf{x}_{I,d} \in S_d$ and considering a local patch of the IMDS at of $\mathbf{x}_{I,d}$ surface area dA of domain d . The subdomains $dV_{d,\alpha}$ are then defined as the volumes of points in $V_{d,\alpha}$ that associate to the IMDS at $\mathbf{x}_{I,d}$ (i.e., these are points where chain junctions are closest to $\mathbf{x}_{I,d}$ among all IMDS points). Graphically, subdomains are wedge-like volumes that extend away from the IMDS into the brush regions on either side of the interface (see examples highlight in white, in Figure 1). Notice that a subdomain is infinitesimal in lateral width but extends to finite dimension along the chains. This is motivated by the fact that in the SSL the area per chain and extent of chain fluctuations transverse to its mean trajectory become arbitrarily small when compared to the mean extension as $\chi N \rightarrow \infty$.^{29,51} Therefore, from this SSL perspective, the finite volume of entire domains should be considered to include a collection of wedge-like subdomain volumes, each of which can be thought to incorporate one (or more) BCP chain volumes.

Finally, we define the terminal boundaries $T_{d,\alpha}$ as the surfaces swept out by the “outer edges” of subdomains of both types. For example, consider the points in $dV_{d,A}$ that extend away from the IMDS of the lamellar domain in Figure 1. At its outer edge, which we call the terminal boundary, $dV_{d,A}$ meets another subdomain, say $dV_{d+1,A}$, corresponding to the neighbor domain $d + 1$. The set of outer edges, or termini, of $dV_{d,A}$ forms the 2D (generally nonplanar) terminal surface $T_{d,A}$; in this example, it

constitutes the boundary between two like domains, $V_{d,A}$ and $V_{d+1,A}$.

Notice that this definition of terminal boundaries does not require any specific assumptions about interpenetration of the brushes. Instead, one can think of these terminal surfaces as analogues to the continental divide along a ridge of the Rocky Mountains. On either side of the ridge, rain and snowmelt flow down toward distinct coasts of the North American continent. Likewise, the terminal boundaries correspond to invisible boundaries that divide opposing brush regions according to the condition that it is equally likely that a chain at that point on the terminal boundary associates to more than one IMDS points. As we illustrate below, this definition provides a natural and generic means to decompose a packing of compact domains (e.g., spheres and cylinders) into cellular shapes that are topologically equivalent to more familiar Voronoi tessellations of crystal packings, but whose shapes reflect the actual physical locations of chains and therefore differ substantially from those cellular polyhedral (e.g., unlike strictly planar Voronoi cells, terminal surfaces in general may have curved shapes). Crudely speaking, we can think of the terminal points as labeling the furthest reaches of chain stretching away from an IMDS.

Importantly, we note that in most (i.e., nonlamellar) domain types there is an “inner” terminal surface, where the subdomain termini contact other subvolumes from the same domain, but those subdomains are associated with distinct points on the same IMDS. As a natural example, consider the inner (core) subdomain in the hexagonally packed cylinder phase, where it is commonly assumed that the chain termini should bunch along the 1D axis through the center of the domain. More generally, this inner terminal surface will be also 2D, which is perhaps easiest to envision supposing a distorted cylindrical domain, whose IMDS cross section is elliptical rather than circular (see discussion of Figure 8 below). In this case, one expects that the inner terminal boundary will be a planar 2D strip. Crossing from bottom to top, this strip delineates regions of the domain that where chains associate to the bottom and top portion of the IMDS. Below, we show that while this definition is quite natural and generalizes to any domain shape, it leads us to revisit previous assumptions about packing frustration in complex domains like DG, where the geometries of both the “inner” and “outer” terminal boundaries are far from intuitive. Crucially, the inner terminal boundaries distinctly need *not* be limited to the usually assumed points (spheres), straight lines (cylinders), skeletal graphs (networks) or parallel planes (lamellae).

In summary, the subdomain decomposition results in the following geometrical objects from a given BCP melt configuration: (i) IMDS (S_d)—a connected 2D surface for each domain $d = 1, \dots, N_d$ in the melt; (ii) domain volumes ($V_{d,i}$)—connected volumes of like components, where chains associate to a common IMDS (one per each material type i for each domain d); (iii) subdomain volumes ($dV_{d,i}$)—(infinitesimal) wedge-like volumes of like components for which chains are associated with a common point on a common IMDS, $\mathbf{x}_{I,d} \in S_d$ (two component subvolumes per point on each IMDS); (iv) terminal boundaries ($T_{d,i}$)—2D surfaces (not necessarily smooth) swept out by the outer/inner edges (termini) of subdomains and adjacent to at least one terminal of distinct subdomain (two surfaces with points associated with points on the IMDS $\mathbf{x}_{I,d} \in S_d$). With these specific definitions in mind, we now proceed to describe examples for analyzing these features and describing their connection to BCP assembly for complex domains. We first focus on the surface geometry of the

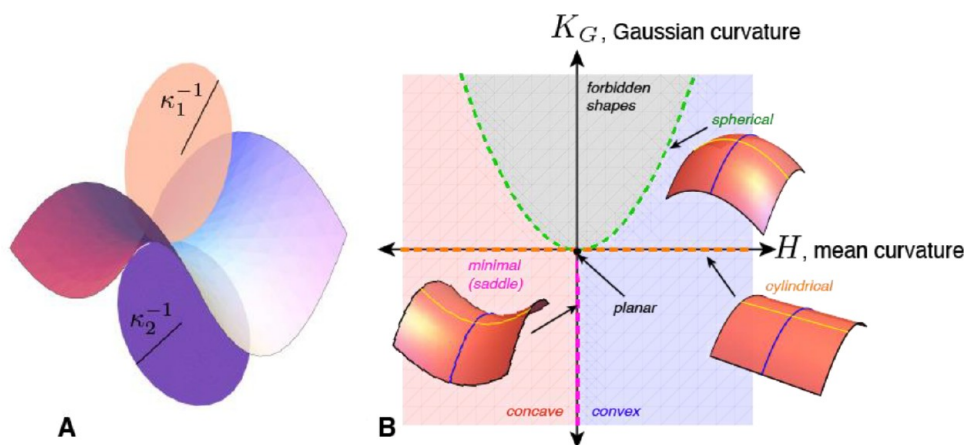


Figure 2. Local metrics of surface shape. (A) Schematic of the local curvature measurement from a 2D surface, shown here as a saddle-like surface, with discs highlighting the curvatures κ_1 and κ_2 measured in two perpendicular directions in the tangent plane of the surface. The orthogonal directions corresponding to the maximal and minimal values of curvature are known as principal curvature directions, and the corresponding curvatures are the principal curvatures of the surface at that point. (B) “Curvature space” of possible 2D surfaces in terms of the mean curvature and Gaussian curvature (eq 1). The dashed lines highlight characteristic classes of shape: spherical, cylindrical, and minimal saddles ($H = 0$ and negative K_G). No shapes exist in the gray parabolic region bound by spherical geometry.

IMDS shape and then describe a generic approach to quantify chain stretching via geometric proxies of the terminal boundary geometry.

II.B. IMDS Geometry: Fingerprints of Surface Shape.

We now describe the metrics of IMDS shape and their connections to BCP assembly thermodynamics. Our key focus is on complex morphologies where these local motifs vary from place to place at the subdomain scale, indicating packing geometries of BCP chains which likewise vary throughout the assembly. We begin with a general discussion of IMDS geometry and its connections to BCP thermodynamics and packing but then focus on the particular case of the bicontinuous DG network as a salient example.

As a two-dimensional surface embedded in three Euclidean dimensions, the IMDS can be characterized by a number of quantities. Some of these are global quantities like the total area or the surface topology (i.e., number of distinct domains and genus), while other quantities of interest for subdomain characterization are local,^{61,62} such as the local orientation of the IMDS (its normal vector \hat{N}) and its curvatures. The analysis of 2D surface curvature is described elsewhere in much greater depth. Here we overview its rudimentary features.

Consider a curve at given point \mathbf{x} on a surface and in direction \hat{v} tangent to the surface at that point (i.e., $\hat{v} \perp \hat{N}$). If r_c is the radius of the circle that just “kisses” this curve at its point of contact with the surface, then the normal curvature along \hat{v} at \mathbf{x} is $\kappa_{\hat{v}}(\mathbf{x}) = r_c^{-1}$. Because the IMDS is 2D, this curvature can be measured in two independent directions at every point. Therefore, we can consider a second direction \hat{u} not only tangent to the surface but also perpendicular to the initial direction \hat{v} with corresponding curvature, $\kappa_{\hat{u}}$. It can be shown that for every direction there is a special set of directions, i.e., a choice of \hat{v} and \hat{u} , such that the curvatures $\kappa_{\hat{v}}$ and $\kappa_{\hat{u}}$ are respectively maximal and minimal. Those directions are known as the principal curvature directions, and the curvatures, which we denote as κ_1 and κ_2 , are known as the principal curvatures (see Figure 2A). The principal curvatures and directions fully characterize the local shape of the surface, and these can be easily computed via a range of numerical techniques, given either an analytical representation of an IMDS shape or instead a discrete approximation, e.g., a triangulated mesh of the $\phi_A(S_d) =$

$\phi_B(S_d) = 1/2$ isocontour from, for example, an experimental 3D reconstruction of the IMDS. Physical properties of physical interfaces, like the IMDS, depend on two rotationally invariant measures of curvature, which are themselves derived from the principal curvatures

$$H = \frac{\kappa_1 + \kappa_2}{2} \quad \text{and} \quad K_G = \kappa_1 \kappa_2 \quad (1)$$

where H and K_G are known as the mean and Gaussian curvatures. Note that the signs of principal and mean curvatures are dependent on the convention used for defining the surface normal, i.e., pointing “outward” or “inward”. Here, we take the intuitive definition such that $H > 0$ for cylinders and spheres. Examples of the local surface shape can be mapped on 2D plane spanned by H and K_G , where standard surface shapes, like planes ($H = K_G = 0$), cylinders ($H > 0, K_G = 0$), and spheres ($H^2 = K_G$), can be visualized by locus of points in “curvature space” (see Figure 2B). Bicontinuous network shapes like DG and DD are characterized by regions of saddle-like surface shapes, corresponding to principal curvatures of opposite sign and $K_G < 0$. Note that no surfaces exist where Gaussian curvature exceeds the spherical limit, i.e., $K_G > H^2$.

For complex domain shapes and, most notably, for the bicontinuous phases like DG and DD phases, IMDS shapes are characterized by spatially varying patterns of curvature.⁶³ As an example, consider the basic unit of the DG IMDS shown in Figure 3A, which envelopes a single node of one of the two gyroid networks. There are 16 nodes per body-centered-cubic unit cell, located at Wyckoff positions 16b of the $Ia\bar{3}d$ space group,⁶⁴ and each nodal region corresponds to a 3-connected tubular IMDS region, as highlighted in Figure 3A. The IMDS of one of the two gyroid networks can be constructed by combinations of translation and rotation of this unit. This basic nodal unit has a D_3 (aka $.3.2$ in Hermann–Mauguin notation) point symmetry: one 3-fold axis along a $\langle 111 \rangle$ direction with three perpendicular 2-fold axes along $\langle \bar{1}\bar{1}0 \rangle$ directions. The 3-fold axes of these units are rotated by $\pm 70.5^\circ$ between adjacent connected nodes. The nodal units of the second network in the DG are generated by inversion, and thus the two independent networks are enantiomorphic. Figure 3B,C shows the spatial distributions of respective mean and Gaussian

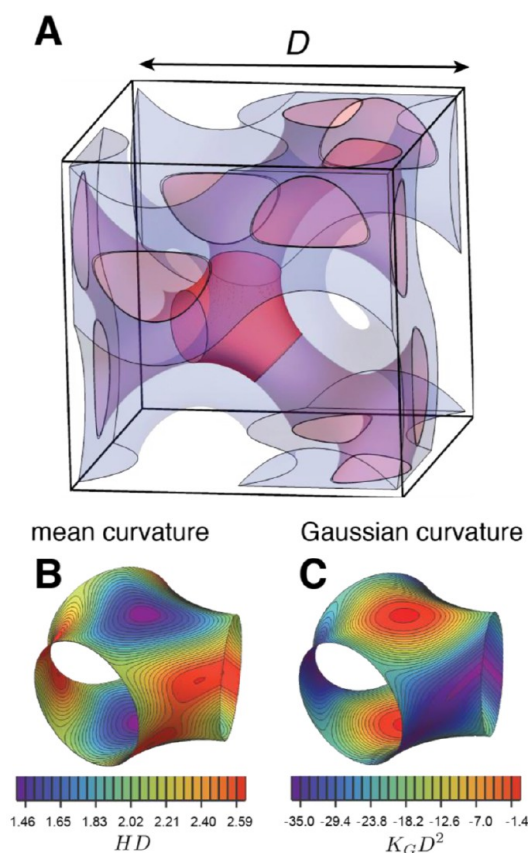


Figure 3. Curvature maps on DG IMDS. (A) A nodal unit of a DG domain, corresponding to a 3-fold IMDS region shown in opaque red, excised from the semitransparent single-gyroid IMDS. Notably, the complete cubic double-gyroid IMDS can be constructed from rotation, translation, and inversion of the nodal unit. Here, one of the two gyroid domains is shown, within the semitransparent blue region. (B, C) Examples of the mean and Gaussian curvature distributions on the nodal unit, whose shape is described by a level set model enclosing 30% of the total volume. Clearly visible are nearly planar regions (H and K_G closest to zero) above and below the plane of 3-fold symmetry and the saddle-like “elbow” (K_G most negative) that adjoin neighboring struts of network.

curvatures on the nodal unit (within one of the two single gyroid network domains) from a level set model of a 30% minority volume fraction DG.⁶⁵ The Gaussian curvature maps roughly delineate two characteristic regions on the nodal unit: a nearly planar region above and below the node centered about and perpendicular to the 3-fold axis where K_G nearly vanishes; and three saddle-like regions in the “elbow joints” that connect pairs of adjoining tubular struts where K_G is most negative. This general pattern of Gaussian curvature is largely preserved for other realizations of IMDS shapes of DG, say, from SCFT predictions, mathematical models, or experimental tomographic reconstructions. Note that certain features of the curvature map vary considerably, notably, the degree to which H varies over the surface and its correlation with local values of K_G . We show below that the spatial map curvature over this nodal unit serves an important “morphological fingerprint” for comparisons between theory and experiment.

How are these local measures of IMDS shape related to the structure and thermodynamics of the underlying BCP chain packing? Here, we review two heuristic concepts and their connection to local curvatures: area-minimizing surfaces and

area distributions. In the regime of sufficiently strongly segregated BCP domains, thermodynamics derives from two dominant contributions: the enthalpic cost of interdomain contact and the entropic cost of Gaussian chain stretching in the brush domains.^{29,31} In well-segregated domains, the interfacial region over which unlike monomers come into contact becomes much narrower than the overall domain thickness, so that the former cost takes the form of a surface energy per unit area $\gamma \propto k_B T \chi^{1/2} \rho_0 a$, where ρ_0^{-1} and a are the respective statistical volumes and lengths of segments in the melt.⁵ Momentarily putting aside the cost of chain stretching, one might expect as a first approximation that BCP morphologies correspond to domains shapes that purely minimize the surface energy cost of unlike domain contact

$$F_{\text{int}} = \gamma \sum_d A_d \quad (2)$$

where A_d is the area of IMDS of domain d . Hence, minimizing the interaction energy corresponds to minimizing the areas of IMDSs. Of course, the variation of IMDS shapes cannot be arbitrary due to the brush-like domains on either side of the interface. As a first approximation, one might expect to account for this simply by considering only IMDS which fixes the volumes of these domains on either side of the 2D surface, due to the fixed volume fraction of unlike blocks composing those domains. In this “unhooked chain” approximation, IMDS shapes could be thought of as emulsions of unlike fluids, ignoring the additional consideration of chain connectivity to the surface, and mathematically, the volume constraint enters through a uniform pressure difference ΔP acting across the interface. Optimal shapes then correspond to the Young–Laplace law:

$$H = \frac{\Delta P}{\gamma} = \text{const} \quad (3)$$

Thus, purely area-minimizing surfaces (subject to constraints on total or relative volume) correspond to the condition of constant-mean curvature (CMC). On the basis of the thermodynamic cost of IMDS area, it was previously proposed, therefore, that CMC surfaces should serve as natural models for BCP morphologies.⁶⁶ For example, neglecting any shape perturbations introduced by anisotropic domain packings (see section II.C), the IMDS shapes of the three canonical morphologies (i.e., in the UCA) of spheres, cylinders, and layers are all CMC surfaces. Beyond these phases, the CMC model of IMDS shape was instrumental in early interpretations of bicontinuous, triply periodic network morphologies like DD and DG. Such network phases are associated with the cubic minimal surfaces, the diamond (D) and gyroid (G) surfaces,^{67,68} which are surfaces that have $H = 0$ everywhere and partition space into two interconnected “labyrinths” of equal volume. Both the minimal D and G surfaces have an associated family of CMC variants^{63,69–71} that enclose different volume fractions of the two types of domains: a slab-like matrix phase surrounding the undulating minimal surface and two interpenetrating tubular networks, which meet at 3- or 4-coordinated junctions (nodes), and remain as connected networks for a wide range of volume fractions for the DG and DD morphologies, respectively. Notably, these minimal surfaces belong to a much broader class of triply periodic minimal surfaces (TPMS), including cubic and noncubic surfaces. The area-minimization properties of TPMS and their CMC cousins and their underlying connection to the formation of associated sponge-like morphologies in a range of

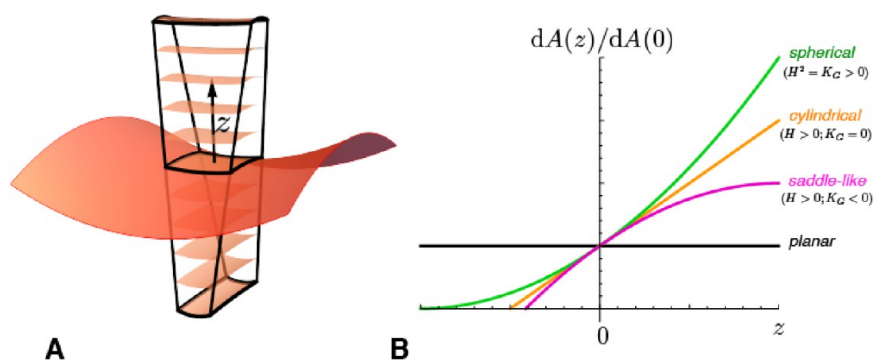


Figure 4. Area distribution and Steiner's law. (A) Schematic of the area distribution corresponding local surface patches extended normally as distance z away for a reference surface, here shown as a saddle-like surface. Steiner's law (eq 4) relates the area of the surface patch at z , $dA(z)$, to the area of the reference patch at $z = 0$. (B) Plots of corresponding area distributions for reference surfaces characteristic of IMDSs of BCP morphologies: planar ($H = 0$, $K_G = 0$), cylindrical ($H > 0$, $K_G = 0$), spherical ($H^2 = K_G > 0$), and saddle-like ($K_G < 0$). The regions of $z > 0$ give a model of outer, convex corona of the curved domain, while the $z < 0$ describes its inner, concave core. Here, we plot cylindrical, spherical, and saddle surfaces with a common value of mean curvature, highlighting differences due to Gaussian curvature.

lyotropic and liquid crystalline systems,^{72,73} are areas of long-standing interest in self-assembling soft and biological materials beyond BCP.

The existence of CMC surfaces with the correct topology and variable volume fractions of bicontinuous networks morphologies of BCP likely would seem to imply that area minimization is the prevailing thermodynamic drive that controls BCP assembly.⁶⁶ Of course, this heuristic picture does not account for the competing effects of the entropic penalty of chains extending away from the interface. Indeed, the role of the IMDS shape on chain packing in the domain volumes underlies the second heuristic concept—area distributions of brush domains. Next, we consider a subdomain volume associated with a particular point on the IMDS, $\mathbf{x}_{i,d} \in S_{i,b}$ which is the location of the interblock junction. The strong-stretching approximation assumes that chain trajectories extend, on average, from the junction point along straight lines away from that interface.²⁹ We define the linear distance z of that trajectory of the i block away from the IDMS, which spans from $z = 0$ at the IDMS to $z = h_i$, the total thickness, or “height”, of the subdomain volume. As shown schematically in Figure 4A, the distribution of volume in this subdomain can then be described by the volume element dz $dA(z)$ where $dA(z)$ is the area of the wedge-like subdomain transverse to the mean trajectory, and the total volume of the α block portion of the wedge is simply the integration of this volume element along z , $dV_\alpha = \int_0^{h_i} dz dA(z)$. The simplest, and most commonly invoked, assumption of BCP chain packing assumes normal stretching, that is, subdomains that extend along the local IMDS normal $\hat{\mathbf{N}}$. Under this assumption of normal extension, the area distribution in the subvolumes follow a simple geometric form, known as Steiner's formula,^{72,74} which relates the area element at z to the area element at the IMDS dA_0

$$dA(z) = dA_0(1 + 2Hz + K_G z^2) \quad (4)$$

where H and K_G are the mean and Gaussian curvatures of the IMDS at the associating point \mathbf{x}_i .

Steiner's formula provides a convenient and intuitive proxy for comparing the distinct packing geometries of BCP domains, purely in terms of local curvature measures of the IMDS. (Although, it is important to clarify that this strict connection holds only for normal extension, which need not be case for an actual BCP domain.) For $H < 0$ ($H > 0$) the geometry is concave (convex), meaning that the available area to the chains in the

subdomain decreases (increases) with distance from the IMDS, as on the inside (outside) of a sphere or cylinder. For cylinders, the area varies strictly linearly, while for spheres, which have $K_G = H^2 > 0$, the area increases quadratically from inside to outside along the normal trajectory. The locally saddle-like shapes of the tubular IMDS of the bicontinuous phases like DG and DD are described by negative curvature $K_G < 0$, leading to negative quadratic term in $dA(z)$. Hence, even for the convex, matrix domain where $H > 0$, the area of these “saddle wedges” increases more slowly with z than cylinders of equivalent mean curvature, and for wedges exceeding a height H/K_G the area distribution actually becomes nonmonotonic with distance from IDMS. Figure 4B shows examples of the area distribution versus height.

A corollary of the Steiner formula for the area distribution is a lesser known condition for the relationship between the curvatures of a base surface and a surface of constant z , i.e., the surface “pushed out” by a constant thickness z along the normals, sometimes called a parallel surface.^{62,75} The local curvatures of this constant- z surface are simply

$$H(z) = \frac{H_0 + K_{G,0}z}{1 + 2H_0z + K_{G,0}z^2}; \quad K_G(z) = \frac{K_{G,0}}{1 + 2H_0z + K_{G,0}z^2} \quad (5)$$

where H_0 and $K_{G,0}$ are the mean and Gaussian curvature of the $z = 0$ surface.

These formulas, in combination with the assumption of uniform height in one of the blocks, provide an alternative heuristic model for the IMDS shape distribution and one that sharply contrasts to the CMC shapes for bicontinuous DG and DD. Notably, it is commonly expected (though not strictly proven) that the entropy cost of block extension should favor uniform height, and the cost of any nonuniform extension required by the domain geometry in combination with the requirement for uniform melt density is associated with packing frustration. In this context, Matsen and Bates^{32,35} suggested that the complex network phases are most acutely frustrated in the minority subdomains interior to the tubular IMDSs, based on apparently nonuniform cross-sectional shapes (we return to measures of subdomain thickness below). Following this line of reasoning, assuming not only that the variation of the tubular block height is unavoidable but also that the matrix block nevertheless strongly favors uniform stretching, one arrives at the so-called constant matrix thickness (CMT) model of IMDS

shape. In this model, matrix blocks are assumed to stretch along the local normal to a constant height h_{CMT} , and the surface swept out by the matrix block subvolumes, i.e., the terminal boundary, is assumed to be a triply periodic minimal surface (G or D) that threads through the middle of the slab-like matrix domain. This implies the terminal boundary of matrix block has zero mean curvature ($h_{\text{CMT}} = 0$), so from eq 5 we have the following linear relationship between mean and Gaussian curvature for CMT models of bicontinuous morphologies:

$$H = -K_G h_{\text{CMT}} \quad (6)$$

As tubular interfaces are characterized by negative K_G (except at certain points), CMT shape implies variable mean curvature, in direct contrast to the CMC canonical domain shapes for which H is uniform and area is minimized for fixed volume (fraction). A deviation of IMDS curvatures from CMC shapes is consistent with SCFT studies of DG and DD morphologies by Matsen,⁷⁶ at least for a limited range of intermediate segregation conditions of linear AB diblocks.

To better visualize the complex curvatures of IMDS shapes for complex morphologies, and following the experimental analysis of Jinnai, Spontak, Hashimoto, and co-workers⁷⁷ (see discussion of IMDS shape characterization below), it is useful to analyze the distributions of mean and Gaussian curvatures plotted in the H and K_G plane, as shown in Figure 2A. Notably, although curvature distributions for IMDSs from complex bicontinuous networks are necessarily variable, even in an ideal equilibrium structure, the two heuristic models of CMC vs CMT shapes, which represent optimal geometries for minimal IMDS areas vs uniform matrix thickness, provide a simple way to frame and interpret the curvature distributions. For CMC shapes, curvature distributions belong to a vertical line of constant H but with variable K_G , while for CMT shapes H and K_G fall along a diagonal line $K_G \propto -H$.

Given the framing provided by these two heuristic models, we then compare the curvature distributions extracted from SCF for bicontinuous DG in Figure 5. The simple shapes of the CMC versus CMT distributions in the H and K_G plane provide a graphical means by which one can assess whether the IMDS shape is more CMC-like vs more CMT-like. For example, in Figure 5A and in ref 78, we compared the curvature distributions for increasing segregation strength, showing that at weak segregation distributions tended more toward the CMC case, whereas increasing to intermediate and eventually strong segregation shows a tendency of these distributions to skew toward a more diagonal distribution consistent with CMT-like shapes. On the basis of the heuristic discussion above, this suggests that a relatively weak segregation, the structure of the diffuse IMDS is dominated by area minimization, and with little perturbation due to chain entropy. The tendency toward more CMT-like shapes at stronger degrees of segregation is consistent with emergence of a thermodynamic balance between area minimization at the IMDS and the countervailing forces of chain stretching in the brush volumes.

In Figures 5B,C, we also show for a fixed (high) segregation strength the effect of variable compositions f and for variable conformational asymmetry, or the ratio of statistical segment lengths $\epsilon = a_A/a_B$, a complex spectrum IMDS “curvature fingerprints”. That is, there is not a “standard” DG motif for equilibrium BCP assemblies, but instead, each IMDS exhibits variation at the subdomain scale whose details trace back to underlying features of the molecular constituents. For this range of conditions, the DG IMDS curvature distributions are

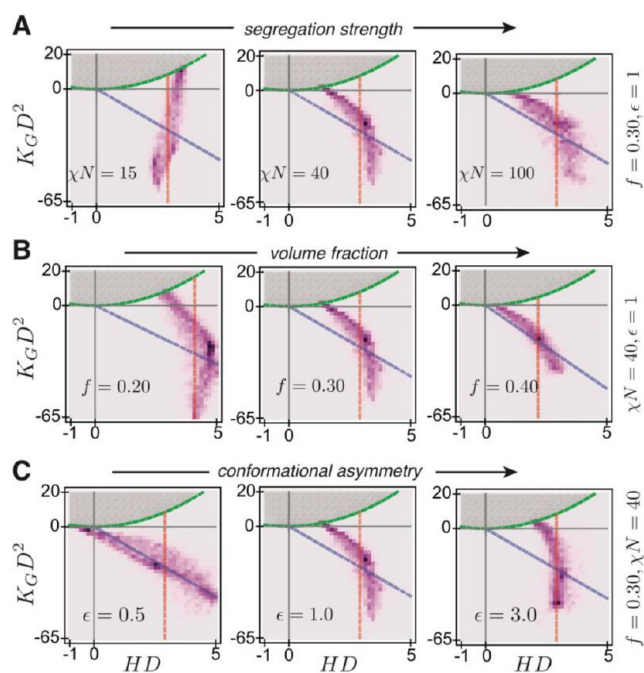


Figure 5. Curvature fingerprints of BCP double gyroids (A–C) show distributions of IMDS shape from DG domains of linear AB diblock melts predicted by SCF, plotted in the H and K_G curvature landscape of Figure 2. Rows compare curvature distributions of systematically varied parameters: (A) shows (left to right) increasing segregation strength χN for fixed volume fraction and conformational symmetric; (B) shows (left to right) segments shows increasing volume fraction f of the tubular domain for fixed segregation strength and conformational symmetric segments; and (C) shows (left to right) increasing conformational asymmetry $\epsilon = a_A/a_B$ for fixed volume fraction and segregation strength. For each case, we show the locus of curvature for the constant mean curvature (CMC) surface and constant-matrix thickness (CMT) surface of the same volume fraction as dashed red and blue lines, respectively. Note the middle column of each row shows the same reference conditions, $f = 0.3$, $\chi N = 40$, and $\epsilon = 1$.

predicted to exhibit characteristic patterns which loosely correspond to the two spatial regions highlighted in Figure 3B,C, i.e., the saddle-like elbows and the quasi-planar elements. Roughly speaking, while the curvature distributions do not follow strictly CMT or CMC distributions, they do tend to localize along a 1D curve in H and K_G space, which looks rather a bit like a “hockey stick” pattern: two approximately linear regions meeting at a common point. We note that flatter ($K_G \rightarrow 0$) regions follow the lower slope, diagonal relationship of the CMT-like surfaces, while the saddle-like regions (more negative K_G) tend somewhat toward more H-vertical, CMC-like surfaces. Furthermore, the tendency toward more CMT-like surfaces also grows with volume fraction of the minority component f , suggesting that as the matrix domain in the DG phase narrows on average, the more it tends to resist thickness variations.

The apparent coexistence between more CMT- and CMC-like regions on the same IMDS (e.g., $\epsilon = 1$ and $f = 0.3$) implies that thermodynamic tendencies of area minimization and optimal chain packing need not be distributed uniformly for complex domains. For the case of the DG phase, these patterns suggest that the prerogatives of IMDS area minimization are more operative in the saddle-like elbows of the nodal unite, while the tendency toward CMT-like packing may be stronger in the quasi-lamellar regions of the IMDS that run orthogonal to the 3-

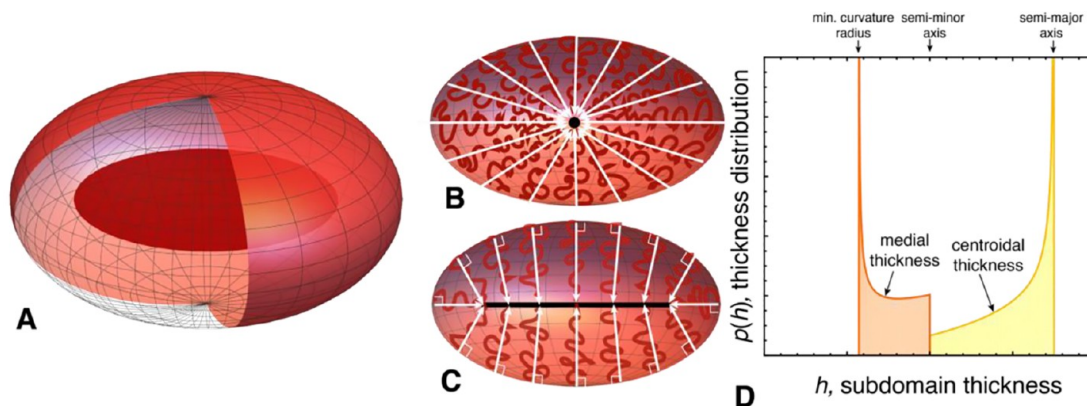


Figure 6. Centroidal vs medial thickness of ellipsoid. (A) An ellipsoidal model of an IMDS shape, which is partially cut away to reveal its inner medial surface, a central disc normal to axis of revolution (semiminor axis). (B, C) Centroidal thickness and medial thickness, respectively, measured in the cross section of the ellipsoid. In the former (centroidal) the thickness h is measured from the bounding surface (i.e., IMDS) to the centroid of the volume, while in the latter (medial) the thickness extends normally away from boundary surface, up to the medial surface, a 1D line in section, shown as black. (D) Comparison of the normalized distributions of centroid and medial thickness h for the ellipsoid. In (B) and (C), cartoons (red) schematically depict the chain packing motifs associated with different thickness measures, suggesting a generically lower entropic cost for medial stretching.

fold axis of the node. To more directly assess how the countervailing drives of chain stretching operating on either side of the IMDS vary throughout the DG domain, we turn in the next section to metrics of the thickness distribution in nonuniform domains.

II.C. Terminal Geometry and Domain Thickness: Where the Domain Ends. In the foregoing section, we described the geometrical measures of IMDS shape and their connections to the thermodynamics of microdomain formation. We now turn to consider aspects of chain packing that are “beneath the surface”, within the like-material component regions of BCP domains away from the IMDS. Here, the central questions to consider are, for a given morphology, what is the physically meaningful notion of thickness of a domain that describes how far chains reach into a domain and which measures best capture variation of the thickness in complex domain shapes and packings? Notably, the specific structure of chains arrayed within these chemically homogeneous domains are essentially invisible to the most common experimental techniques (see discussion in section III). Although the specific structure of chain packing is far less accessible to experiments than the IMDS itself, it is no less critical to the thermodynamics of the BCP assembly, particularly when it comes to predicting and understanding why some complex morphologies appear and others do not. Thus, we focus on measures of the domain thickness and local extension of chains that can be inferred from the composition field of unlike domains and the IMDS, i.e., without specific data on the chain configurations themselves.

To clarify our meaning of domain thickness, we return to the terminology introduced above in section II.A, where subdomains describe the wedge-like volumes of chains that associate to a particular point on a particular IMDS. On either side of that IMDS, chains extend away from their interblock junctions into brush-like domains of like material. If we imagine following the extension of the chain along the contour of the subdomain, we eventually encounter chains from an opposing brush, i.e., chains that associate to some other distant point on an IMDS (which could belong to the same or a different domain). The point along the subdomain contour where its segments are equally likely to belong to some other subdomain marks the terminal boundary, essentially the geometric “end” of the

subdomain. We define the local thickness of this portion of the domain (belonging to one of the polymeric blocks) as the distance between the terminal point and its corresponding point on the IMDS, where the chain junctions lie.

While chain ends are in fact distributed throughout the volume of the subdomain and there is always some degree of brush interpenetration even in well-segregated samples, such a local thickness measure has the clear advantage that this quantity enters directly in the SST description of BCP thermodynamics in the leading order entropic cost of chain stretching in the brushes. The coupling between entropy and 3D packing of chains is arguably made most transparent in what is known as the parabolic brush theory⁷⁹ for the entropy in the SSL, which takes the form for the domain^{5,56}

$$F_{\text{st}}^{(d,\alpha)} = \left(\frac{3\pi^2\rho_0}{8N_\alpha^2 a_\alpha^2} \right) \int_{V_{d,\alpha}} dV z^2 = \left(\frac{3\pi^2\rho_0}{8N_\alpha^2 a_\alpha^2} \right) \int_{A_{d,\alpha}} \int_0^{h_{d,\alpha}} dz dA_{d,\alpha}(z) z^2 \quad (7)$$

where N_α and a_α are the respective number and statistical length of α -type segments, and ρ_0^{-1} is their (assumed) common volume. In this formulation, the parabolic brush entropy “measures” the mean-square distance along the trajectories away from the IMDSs, averaged over the volumes of those brush domains (of each block), up to its maximal distance, $h_{d,\alpha}$. Hence, these heights $h_{d,\alpha}$ which we call the subdomain thicknesses, are the most directly relevant measures of thickness from the point of view of the SSL thermodynamics of chain packing. With this in mind the natural question becomes given a set of BCP domain shapes, specified by a set of corresponding IMDSs; how do we extract subdomain thicknesses $h_{d,\alpha}$ i.e., without direct access to the chain configurations themselves?

At first glance, the notion of subdomain thickness for BCP seems fairly intuitive. On the inside of an IMDS (say for a cylinder of spherical domain), chains extend some distance toward the “center” or “midpoint” of that volume, while on the outside chains stretch up to a “halfway” point between opposing brushes meeting from two neighbor domains. Despite their

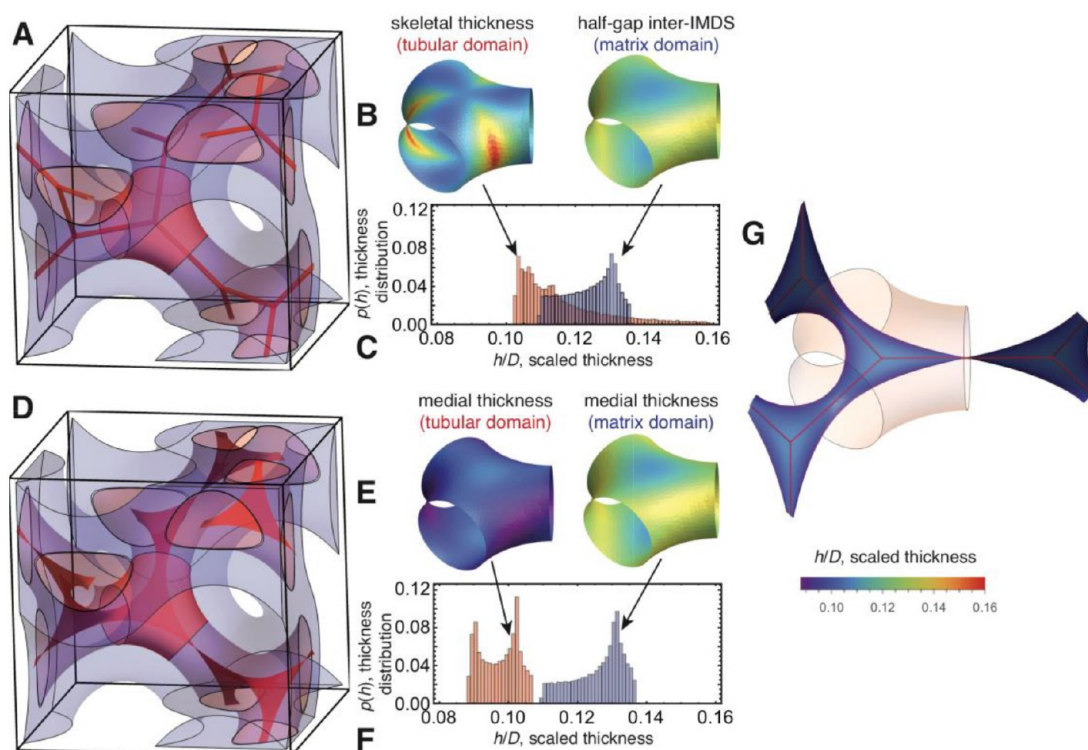


Figure 7. Skeletal vs medial thickness of tubular network domains. (A) A unit cell of the cubic DG, highlighting the skeletal graph (red line) of that threads through one of the single gyroids, with a single nodal unit of the IMDS highlighted as in Figure 3. Here again, we consider the $f = 0.3$ level set model of the gyroid IMDS. (B) Distribution of local skeletal thickness, h , measured from the IMDS to the closest point on the skeleton. The histogram in (C) compares the thickness distributions from the skeletal ansatz for the inner domain (red) to the thickness distribution of the outer (matrix) domain (blue), which in this plot is computed as a half the distance from a point on the IMDS to its closest point on the other IMDS. For comparison, (D) shows the “medial web” corresponding to the interior medial surface (dark red) within the IMDS of the same single gyroid domain as (A). (E) shows the medial thickness distribution from the IDMS to its corresponding point on the medial web, shown in (G). The color scale is shown via the same scaled thickness in (B), (E), and (G), highlighting clearly that the largest skeletal thickness corresponding to the shortest medial thickness regions. (F) plots the normalized medial thickness for inner (red) and outer (blue) domains. Comparison of (C) to (F) shows that medial thicknesses are considerably less disperse and shorter, on average, than skeletal thicknesses.

intuitive appeal, these notions run into ambiguity as soon as one tries to account for local variations of domain shape required from space-filling BCP assemblies.

To illustrate this point, and to introduce a generic framework for defining subdomain thickness from IMDS shapes, consider the interior to an ellipsoidal domain shown schematically in Figure 6A. This shape could approximate the oblate shape of quasi-spherical domains in, say, a FK phase as we describe below, but for now we simply ask the following question: given such a convex, but anisotropic IMDS shape, how should one estimate its thickness? As outlined above, the notion of domain thickness depends on the location of the terminal boundary, that is, the locus of points that define the furthest reaches of subdomains extending away from the IMDS into the interior of this domain.

Arguably the simplest assumption for this terminal boundary, and one that is often assumed for the interior of convex domains, such as spheres and cylinders, is what we call the centroidal ansatz.^{29,33} In this ansatz, the terminal boundary is the point-like centroid of volume of convex domains (e.g., Figure 6B) or the line-like centroid of cross-sectional area for quasi-cylindrical domains. For perfectly symmetrical, spherical or circular, IMDS shapes, this is quite reasonable as all chains would have to extend the same distance to the central point or 1D axis from the IMDS. However, constraints on the packing on spheroidal or cylindrical BCP at constant density always require some perturbation from perfect spherical or cylindrical IMDS symmetry. Moreover,

asymmetric IMDS shapes become a symptom, if not a feature, of complex spheroidal phases such as FK phases. Hence, a realistic description of chain packing in convex BCP domains must account for anisotropic domain shapes that depart from spherical or cylindrical. Considering the simple example of the ellipsoidal domain, it is intuitive to see that the centroidal ansatz would assume that subdomains must vary in their extension, with relatively longer (shorter) thickness extending from the high-curvature (low-curvature) points on the IMDS to the center point, a distribution which corresponds to the yellow thickness histogram in Figure 6D. It is also intuitive that the more anisotropic the domain shape becomes, the more pronounced is the asymmetry between the largest and smallest local thickness value if the terminal boundary is fixed to the centroid. From a thermodynamic point of view, such asymmetric stretching becomes unfavorable relative to a more uniform distribution of the chain entropy.

This dilemma motivates a second terminal packing motif, which we denote as the medial ansatz. This ansatz is formally connected to what is known as the medial set of a surface (embedded in three Euclidean dimensions), a concept developed in the field of computational geometry.^{80–83} Mathematically, the medial set (or sometimes it is called medial skeleton or medial axis) is the set of points equidistant to two or more points on a boundary surface (or set of bounding surfaces). To visualize this, consider a point interior to the ellipsoidal

domain in Figure 6. The distance to the closest point on the boundary surface extends along the normal of that surface at the closest point. As we consider the points distributed along a common normal vector, they all have to the same closest point on the boundary surface, until we reach a point that is equally distant to another point coming from the opposite side of the boundary surface. For the oblate ellipsoid, as shown in the cross section in Figure 6C, these points lie on the mirror plane that bisects the ellipsoid (perpendicular to the semiminor axis), and the set of those points constitute a flat 2D surface—a disk. Notice that medial points corresponding to the high-curvature rims of the ellipsoid occur where the local normals of the boundary surface focus and intersect, forming a circular edge of this medial set.

If we consider the distances from the boundary surface to the medial surface of the ellipsoid, we find a medial thickness distribution given by the orange histogram in Figure 6D. Comparison to the (yellow) centroidal thickness distribution shows the obvious conclusion that for each point on the IMDS the medial thickness is strictly less than the centroidal thickness for the same corresponding point. We further note that the medial thickness is less than or equal to the so-called focal thickness defined by the thickness h_f , given by the height at which according to Steiner's law; $dA(h_f) = 0$.⁷⁴ It can be shown that the medial set construction not only generates a local thickness, but it also tessellates the entire domain into a set of space-filling subdomains. That is, within the infinitesimal wedge-like subvolumes that extend from the bounding IMDS along its normal, all points up to the medial thickness are associated in the sense that they are closest to the same point on the boundary.

Hence, we propose here that the medial mapping provides a natural and generic model of chain stretching along the normal on either side of an arbitrarily shaped IMDS. Schröder-Turk, Hyde, and co-workers^{73,84} first proposed the medial thickness as a physical metric of inhomogeneous thickness for low molar mass lyotropic examples of the bicontinuous phases.⁸⁵ Here, we extend those insights to the asymmetric packing constraints in multiple domain BCP morphologies, for both network and non-network morphologies. Indeed, since both centroidal and medial ansatzes provide space-filling motifs, it is straightforward to argue that the entropic cost of stretching in the latter should be generically lower than the former for the same domain shape. That is, not only are medial chain packings possible for arbitrary domain shapes, they very likely provide a more realistic description of the optimal free energy configurations. Taken together, this suggests that the medial thickness provides the most natural and generic metric for chain packing in BCP domains.

In the remainder of this section, we give two demonstrations of the implications of medial geometry of BCP domains by comparing it to other previously invoked and, while arguably more intuitive, less physically realistic notions of domain thickness. First, we consider how the medial geometry of bicontinuous phases, like DG and DD, revises the heuristic notion of packing frustration, principally for the blocks that constitute the interior of the tubular network domains. Second, we consider the medial geometry of the “outer blocks” in various periodic packings of sphere-like domains and revise the standard notion that each sphere-like domain occupies a polyhedral cell-like volume. We refer the reader to the Supporting Information where we present in some detail the workflow involved and instructions to obtain prerequisite data structures necessary to compute medial surfaces via two different algorithms starting

from either BCP composition fields or IMDS shape directly, as input. It also contains links to source data repository where we host our software used to compute medial surfaces for analysis shown in Figures 7, 9, and 20.

II.C.1. Skeletal vs Medial Packing in Bicontinuous Tubular Networks. Understanding the nature of chain packing in the complex bicontinuous phases, like DG and DD, has been central to rationalizing their thermodynamic stability in the BCP phase diagram. Notwithstanding the near-optimal IMDS area properties of tubular DG and DD phases described above (or at least for their CMC variants), a central question has been: how does one deal with the inhomogeneous molecular environments required by the complex geometry of these phases and the constraints of uniform density?

To appreciate the problem of packing within tubular network phases, it is useful to recall the anatomy of these phases. Here, we focus our description on the DG phase (see Figure 7), but this anatomy generalizes to other double network phases, such as the DD and DP structures. On the basis of the definition of domains given above, an infinite triply periodic (cubic) structure of DG phase includes only two domains (see Figure 1). These domains are separated by a saddle-like terminal surface that divides the two matrix blocks at contact between their opposing brushes and confines the two independent minority domains into two equal volumes. To a good approximation, this outer terminal surface has the shape of the triply periodic G minimal surface. The IMDSs within either domain have the form of two tubular surfaces that interconnect in a network of 3-coordinated nodes. These tubular surfaces have the same topology and general shape as the CMC variants of gyroid surfaces.⁶⁹ The topology of each network can be abstracted to a skeleton of bonds (skeletal graph) that thread within the tubular struts from the center of one 3-coordinated node to the next.^{64,67} The nodes (or vertices) of each of the two skeletons, each a single gyroid (SG) network, are situated at eight of the 16b Wyckoff positions of the $Ia\bar{3}d$ cubic space group of DG (the other SG skeleton spans on the other eight positions). This skeleton captures the topology of the tubular domains of the DG in the sense that characterizes all of the equivalent (noncontractible) loops that can be formed while staying within the same tubular domain volume. For example, the single gyroid skeleton is classified as (10,3)-a net in terms of its smallest nontrivial loop, a 10-strut path from one 3-valent node to the next. Likewise, the diamond network, which composes the skeletons of the DD phase, is categorized as a (6,4) net.⁸⁶

Beyond this topological property, these skeletons have been used for characterizing the packing geometry of the double network morphologies, although it must be noted that they do not strictly encode geometrical properties of the domains, so that one should consider their use as morphological metrics with care. The skeletons seemingly approximate the “centers” of the tubular domains and therefore are often invoked to construct an intuitive generalization of the centroidal ansatz of convex domains, which we call here the skeletal ansatz,⁷⁴ in which the blocks extend from the IMDS to a terminal boundary that is confined to this 1D graph (see Figure 7A–C). For example, SSL calculations by Milner and Olmsted²⁹ and Lihtkman and Semenov³⁰ consider the free energy of DG and DD morphologies where subdomains of minor blocks terminate on these skeletal graphs. Notably, these SSL calculations predict that the free energies of the DG and DD phases always exceed competitor phases (e.g., lamella and hexagonal cylinders) over

the full range of conditions for diblock melts and are therefore not equilibrium phases according to existing SSL theory.

The high free energy of the DG and DD phases based on this skeletal ansatz is consistent with a heuristic picture that the interior of the tubular domains introduces excess chain stretching due to requirement of the chains to reach from the IMDS all the way to the n -valent nodes where bonds of the skeletal graph join. See, for example, Figure 7B which shows the spatial distribution of distances from the IMDS to the skeleton for the tubular block of DG (the figure shows the 3-fold nodal unit of the IMDS in Figure 3). In Figure 7C, we compare the skeletal thickness distribution of this tubular block to the matrix block, which we measure as 1/2 of the distance from a point on the IMDS to the closest point on the IMDS of the other network (note that the midpoints between these IMDS to IMDS separations roughly approximate the G minimal surface). Indeed, the skeletal thickness distribution of the block within the tubes is larger on average and more disperse than the matrix thickness distribution of the block outside the IMDS, seemingly confirming the idea that key “problem” for the DG is primarily packing within the interior of the tubular junction, which is most often (e.g., for linear AB diblocks) the minority component block.

Employing the medial measurement of subdomain thickness paints a qualitatively different picture of packing frustration in bicontinuous network phases and one, which we argue, more accurately reflects the physical constraints of chain packing and thermodynamics of these phases. Figure 7D shows the medial surfaces computed from the two IMDSs of the DG phase (from a 30% minority level set model). This includes the terminal boundary of the matrix phase, which roughly follows the gyroid minimal surface and divides the two domains at the extreme of the outer brushes. The interior of each tubular (SG) network is described by a medial surface that maps out the “midpoint” on the interior of that domain. Notably, these are not 1D sets (although the 1D skeletons lie within the medial surface), but a 2D, web-like surface that threads through each network. These interior medial surfaces spread out into quasi-triangular “webs” that span the plane of the 3-coordinated nodes of the skeleton (see Figure 7G). Between two webs on adjacent nodes of the single gyroid the tangent planes define a dihedral angle which rotates by $\pm 70.5^\circ$ as one progresses along the skeletal graph, where the rotation sense is constant for a given SG network and defines its chirality.⁷⁴

The web-like appearance of the medial surfaces interior to the tubular IMDS encodes a simple fact: polymeric blocks need not extend all the way to the 1D skeletons of the network, but instead need only to extend to this medial web to fill the “middle” of the tubular domains. The implications of this fact are most easily seen by comparing the inner domain thickness distributions of the skeletal graph vs the medial subdomains in spatial maps of thickness in Figures 7B,E and corresponding histograms in Figures 7C,F. Simply put, the medial measure of subdomain thickness is reduced (relative the skeletal one) by a large and substantive margin (20% for this particular composition) leading to a far more comparable mean thickness between the matrix and tubular domains in this medial ansatz. This thickness reduction largely comes from the three saddle-like regions of the IMDS that span between the quasi-cylindrical shaped portions that enclose adjacent struts, since subdomains need only to extend to the 1D edges of the triangular web of the medial surface, as opposed to the full distance to the skeletal node. In this way, surface regions of maximal thickness of the

skeletal ansatz actually correspond to the regions of minimal thickness in the medial ansatz, and vice versa, as shown in the spatial map of skeletal and medial thickness of the tubular domain in Figures 7B,E.

The reduced chain stretching required for medial in comparison with skeletal packing of BCP chains argues that the former is far more likely to describe a thermodynamically stable chain packing. Moreover, it suggests that previous heuristic views, not to mention prior SSL calculations, have significantly overestimated the cost of packing frustration in the DG and other bicontinuous phases. It remains to be understood how sensitive the predictions of the stability window of DG in the limit will be to this more modest degree of chain stretching suggestion by the medial thickness of tubular networks and, as we address in section III, how experimental methods can ultimately map the chain trajectories away from both sides of the IMDS.

II.C.2. Voronoi vs Medial Cells of Sphere and Cylinder Phases. For the bicontinuous phases packing frustration is most commonly associated with minority blocks that compose the interior of the tubular domains. Spherical or cylindrical volumes cannot tile space without interstitial gaps. Hence, frustration in these sphere and cylinder morphologies is heuristically associated with the shape of the outer subdomain component (most often the majority component), although as we see below, the consequences of this frustration are distributed to the inner domain packing as well. To maintain uniform polymer density, the outer brushes of the domains must conform to lower than spherical (or cylindrical) symmetry environments that derive from their crystallographic packings. The shapes of the terminal boundaries are most often approximated as the Voronoi cells (VC) of points that define the particular crystal structure.^{29,33,37,87} These polyhedral volumes enclosed by VCs are defined as the region closest to a given point, known as the generators of the Voronoi cells.⁸⁸ Intuitively, BCP chains are frustrated by the fact that, unlike for an ideally spherical domain, coronal blocks have to extend further into the corners of these polyhedral regions than they do to reach the planar walls. However, like the skeletal graphs of network phases, Voronoi cells can correctly capture the topologies and gross shapes of different sphere-like or cylinder-like domain packings but do not, in general, offer an accurate model of variable subdomain thickness in BCP domains, either core or coronal.

Voronoi cells are constructed from the set of perpendicular planes that bisect any pair of generating points: the cell bounds all points that are closer to its generating point than to any of the other generating points sites in the set.⁸⁸ This results in a convex polyhedral volume whose bounds are defined by the intersections of those planes surrounding the site. Note that generating points of Voronoi cells need not be periodic. In the context of equilibrium models of BCP phases, in which sphere- or cylinder-like domains are arrayed periodically, generating points are most often taken as point distributions that model a given crystal structure. A simple 2D example of this is the hexagonal cell of the hexagonal point lattice (see schematic in Figure 8A), which creates a hexagonal Voronoi cell via the set of edges separating the point from each of its six nearest neighbors. An 3D example is a BCC lattice (Figure 8B). Here the Voronoi cell is a 14-sided truncated octahedron: 8 (larger) hexagonal faces from nearest neighbors along the $\langle 111 \rangle$ directions and 6 (smaller) square faces from next-nearest neighbors along $\langle 100 \rangle$ directions.

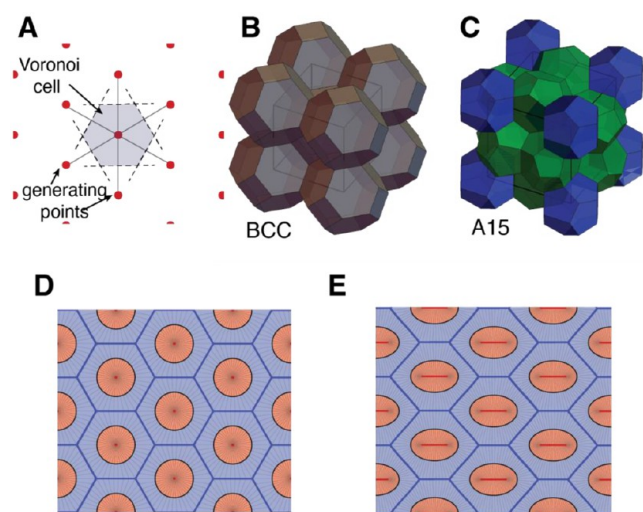


Figure 8. Cellular models of domain shapes (A) show Voronoi cells from a generating set of hexagonal lattice points. (B, C) Voronoi cells corresponding to cubic crystals, BCC and A15, respectively, formed by sphere-like domains of BCP. While BCC possesses only a single cell type, a 14-sided truncated octahedron, the Frank–Kasper A15 has two symmetry-inequivalent cells, deriving from two distinct Wyckoff positions: 12-sided cells (Z12) shown in blue, and 14-sided cells (Z14) shown in green. (D, E) Medial surfaces for circular and elliptical IMDSs shapes (shown as black lines), respectively, arrayed on a hexagonal lattice. The inner medial sets are shown in dark red (a dot and line for circular and elliptical domains, respectively), while the outer “medial cells” are shown as dark blue. Notably, the medial cells of circular domains are identical with Voronoi cells but significantly differ from Voronoi cells for elliptical domains.

It is commonly thought that distinct spherical BCP domains are enclosed with the Voronoi cells of the corresponding crystal structure.^{34,37} Specifically, in the nomenclature that we have introduced above, this assumes faces of Voronoi cells define the terminal boundaries of the corona domains, planar regions where opposing brushes from neighbor sphere-like domains meet. However, it is important to note that Voronoi cells define only the volumes of space closest to a point (i.e., the generating Wyckoff point of the cell) and as such encode no information about the size and shape of objects packed at those points. The Euclidean distance to the spherical domain centers (Wyckoff sites), upon which the Voronoi–Wyckoff tessellation is derived, is in general a poor proxy for this association to one domain or another.

To illustrate this point, we consider a simple 2D examples of two types of domains arrayed on a hexagonal lattice in Figures 8D and 8E, whose IMDS shapes are circular and elliptical, respectively. The Voronoi cells associated with the lattice points at the centers of both types of domains, isotropic and anisotropic, are identical honeycombs of regular hexagons, as is Figure 8A. Hence, in the case of elliptical IMDS in Figure 8E, the shape of the Voronoi cell does not reflect the anisotropic shape of the domains packed at the lattice points (in general, these are Wyckoff positions). This would be an unrealistic model of for the terminal boundaries as it reflects no information about the relative distance of points in the cells to the IMDS. In short, Voronoi cells, which lack information about the relative volumes and shape of the domains occupying different sites of the crystal packing, in general provide an inaccurate model of boundaries between neighboring coronal domain brushes in the matrix.

While the distance from the domain centers is insufficient to define boundaries between them, we argue here that the distance of points in the coronal domains to the IMDSs themselves should be closely correlated to association to one domain over another. This follows from the heuristic notion that for a chain with a segment at given point entropy favors it to be associated with the closest point on the nearest IMDS because this presumably requires the least stretching. Those boundaries that divide space into the volumes that are closest to the IMDSs of distinct domains are precisely the medial surfaces of the coronal domains of the lattice. Thus, we argue that the medial geometry on the outside of convex domains, such as those of sphere and cylinder phases, provides a more accurate physical picture of chain packing, and a more meaningful measure of subdomain thickness, than can be captured through the shapes of Voronoi cells of the same lattice. Returning to our example of the 2D domain packings in Figures 8D,E, we see that the medial cells distort in shape to reflect changes in local distance from IMDS in anisotropic elliptical domains.

Beyond this simplistic example, it is crucial to point out that BCP domain shapes in these complex crystals are far from spherical. In terms of the symmetries, the space group of a crystalline model of BCP structure implies that objects at occupied Wyckoff position conform to certain point group symmetry (i.e., a set of symmetries from inversion, mirror, rotation, and improper rotation). Provided that they conform to these point symmetries, the shape of the IMDS and the distributions of the underlying chains that occupy each position are free to vary from spherical. Indeed, the IMDS of these domains can be strongly warped away from spherical shape, indicating that the association map (which describes the probability of chains to associate their junctions to the IMDS) are far from isotropically distributed around the domain center.

Where might the difference between the Voronoi cell vs medial cell geometry be significant? Precisely when the domains assembled at different sites in the crystal structure differ in size (i.e., volume) and shape. This is the situation that arises in Frank–Kasper (FK) phases of BCP, which have recently drawn immense interest in BCP^{39,40,42–44} and other amphiphilic assemblies.^{41,89–92} The spherical domains in canonical BCP crystal phases, such as the BCC phase (space group $Im\bar{3}m$ with Wyckoff site 2a occupied), sit at symmetry-equivalent positions and are therefore described by identical copies of the same convex domain, albeit with the IMDS warped somewhat into a locally polyhedral shape commensurate with the particular point group of the Wyckoff site. In contrast, FK phases possess multiple, symmetry-inequivalent positions.⁴⁶ For example, the A15 phase (space group $Pm\bar{3}n$) has two sets of occupied positions per primitive cubic unit cell: one site at the corners and another at the center of the unit cell (Wyckoff positions 2a) as well as three pairs of points arrayed on the faces of the unit cell (Wyckoff positions 6c). The Voronoi cells of A15 are shown in Figure 8C. The structure of a particular FK phase (there are many variants) is often classified in terms of the Voronoi cells of the Wyckoff sites (known as FK polyhedra⁹³) and the number of faces of the cell. In A15, one cell type (Wyckoff position 2a) known as Z12 has 12 pentagonal faces and point group symmetry $m\bar{3}$. (blue cells in Figure 8C), while the second cell type (Wyckoff position 6c), known as Z14, has 12 pentagonal faces plus two hexagonal faces and has point group symmetry $4\bar{m}.2$. (green cells in Figure 8C). Given the rather different shapes of these two local environments in A15, it should not be expected that the quasi-spherical domains that occupy these

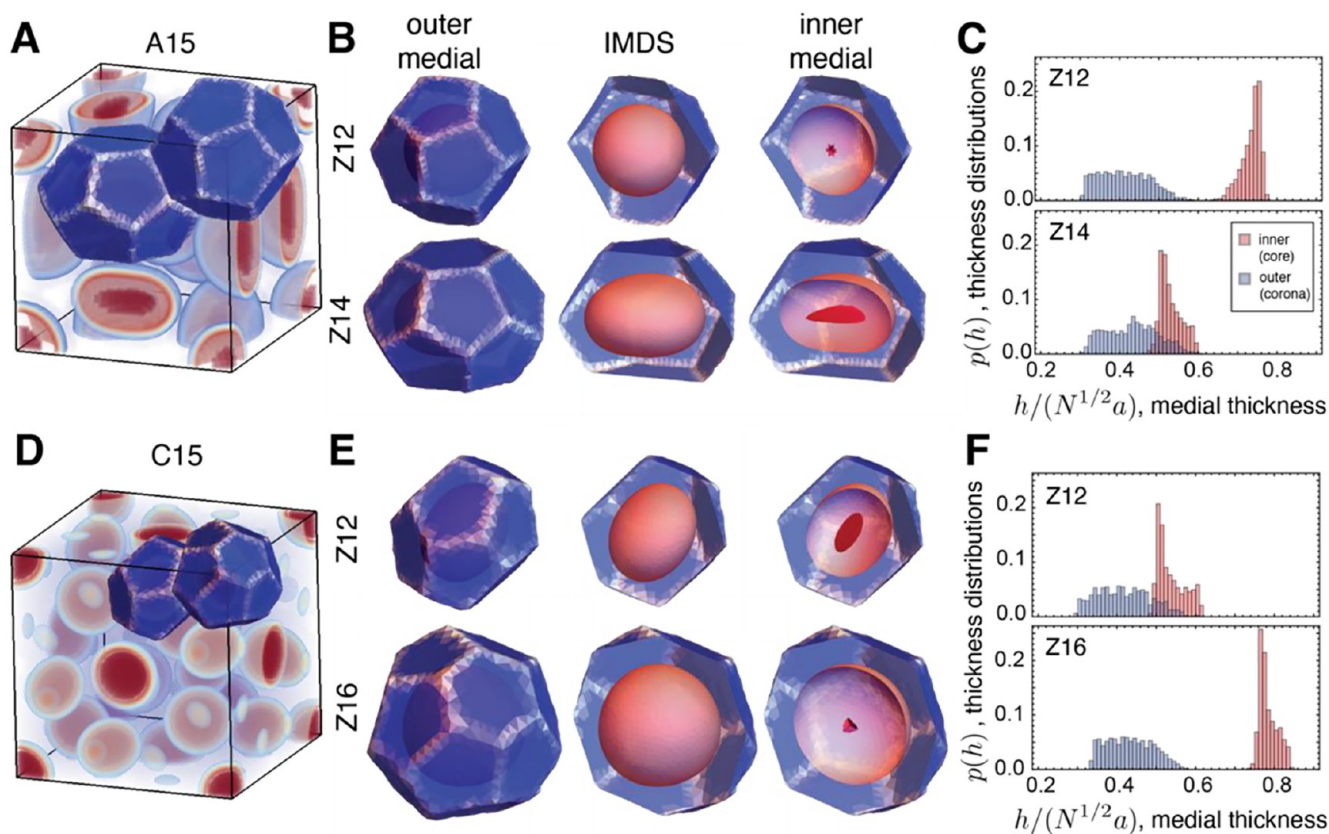


Figure 9. Medial decompositions of BCP Frank–Kasper phases. (A, B) The outer (blue) and inner (red) medial surfaces computed from IMDSs (pink) of the A15 phases predicted by SCF, $f = 0.29$, $\chi N = 40$, and $\epsilon = 1$. (D, E) The same for the C15 phase, at the same conditions. (A) and (D) highlight the outer medial “cells” of one of each type of the inequivalent positions in both crystal structures, with 1D edges highlighted as white facets. (B, E) Individual cell types partially cut through their centers to reveal the IMDS shapes interior to outer cells and then the medial sets interior to those domains. All cells are cut along the $\langle 100 \rangle$ direction. (C, F) Histograms of medial thickness for domains in A15 and C15, respectively.

distinct positions would be nearly identical, despite the fact that thermodynamics favors a uniform local IMDS curvature and domain thickness. Likewise, in the σ phase, where there are five types of symmetry-inequivalent sites occupied in the $P42/mmm$ space group, each of those distinct sites must be occupied with domains adhering to the requisite point group symmetry of the site. Note that the difference in point group symmetry of these occupied domains allows for some difference in the shapes of those domains, but point symmetries do not place constraints on the relative volumes of those domains

Indeed, previous theories and rationalizations have attempted to relate the stability of distinct competing FK phases to the shape asymmetry of the distinct positions, quantifying asymmetry in terms of distinct geometric measures of the “cell shapes” (e.g., area and second moment).^{37,47,94} However, it is not entirely clear which cellular shapes to compare.⁹⁵ Bates and co-workers³⁷ noted that (i) Voronoi–Wyckoff cells in competitor BCP FK phases have unlike volumes at symmetry-inequivalent sites and (ii) volume asymmetry may lead to average measures of cell shape that are in fact more symmetric equal volume cells. Thus, they conjectured that equilibrium FK phases are facilitated by molecular exchange between distinct sphere-like domains. Notably this is something that atomic alloys can only do to a very limited extent, say, via electron exchange.⁹⁶ Indeed, SST calculations, based on the so-called “diblock foam model”, have predicted that relaxation to asymmetric volumes between cellular regions of symmetry-inequivalent positions in FK phases leads to lower free energies

than for equal volume domains. Furthermore, these shapes are even more asymmetric in volume than the Voronoi cells, by roughly a factor of 2 throughout the competitor phases.³⁸ This enhanced volume asymmetry of symmetry-inequivalent spherical domains of FK phases agrees quantitatively with SCFT calculations. For example, volumes of the Z12 and Z14 Voronoi–Wyckoff cells of the A15 lattice differ by only 3%, while the corresponding volumes of the equilibrium domains according to the diblock foam model and SCFT have a larger, nearly 15%, difference in volume. This tendency to “inflate” the larger domains at the expense of the smaller ones is analogous the coarsening of a dry foam, except in the diblock foam, larger volume asymmetries are ultimately restrained by the entropic penalty of chain stretching for fixed molecular weight with increasing domain volume.

To compare the accuracy of the medial surfaces and to capture the terminal boundary and domain thickness of sphere-like domains, in Figure 9 we consider SCFT predictions of A15 and C15, two types of FK phases, both with two different cell types. The thermodynamic stability of FK phases relative to BCC in diblock melts is understood to derive from large elastic asymmetry between the different blocks,^{33,38,97} conditions that can be achieved for diblock miktoarm (or “mixed arm”) stars with more coronal block arms than core arms or instead for conformationally asymmetric linear diblocks with shorter segments in the coronal B blocks relative to core A blocks (i.e., $\epsilon = a_A/a_B > 1$). For each phase we consider, conditions of conformationally symmetric and conformationally asymmetric

diblocks to highlight the changes in subdomain morphology that accompany the change in thermodynamic stability. Medial surfaces are computed from the IMDS shapes derived from converged SCFT solutions via the methods summarized in the [Supporting Information](#) (and supporting software).

In [Table 1](#), we consider the relative volumes enclosed by the different cells (i.e., Voronoi vs medial cells) and compare relative

Table 1. Comparison of Volume Ratios in FK Domains to Cellular Models

structure (domain ratio)	Voronoi cells	medial cells (SCF, $\epsilon_p = 1$)	occupied vol (SCF, $\epsilon_p = 1$)	medial cells (SCF, $\epsilon_p = 3$)	occupied vol (SCF, $\epsilon_p = 3$)
A15 (Z14/Z12)	1.03	1.27	1.27	1.17	1.19
C15 (Z16/Z12)	1.23	1.25	1.33	1.33	1.42

volumes occupied by the inner A blocks at each Wyckoff position computed for A15 and C15 for conformational symmetric and asymmetric cases. For all cases, medial cells better match the true volume occupied per spherical domain and, as stated above, generically reflect the greater volume asymmetry of those domains in comparison to the Voronoi cells (e.g., Voronoi cells of A15 are only 3% different in volume, but spherical domain volumes differ in excess of 20%). It is worth noting, however, that while medial cell volumes track closer to the true occupied domain volumes of C15 than Voronoi cells, they still fall systematically below, indicating that medial sets are really only a proxy for the terminal boundaries derived from

IMDS shape and do not strictly derive from consideration of interdomain contact, as described at the start of this section.

For closer comparison on the changes in the cell geometry, we superpose outer cell boundaries with the polar order parameter \mathbf{p}_B of the segments of outer B block from SCF solutions A15 phase in [Figure 10](#). This orientational order parameter gives the mean vector orientation of B segments (with vectors pointing from the “alpha” free end toward the junction to the “omega” free end along the backbone) at every point in space. As this orientational distribution derives from the distribution of chain configurations itself, following ref 98, it can be directly computed from mean-field SCF solutions for ordered BCP phases. The terminal boundaries between adjacent cells correspond to separatrices, that is, dividing boundaries in this flux field, that delineate regions where chains associate to alternate IMDSs. [Figure 10](#) shows this order parameter map on a cut through the Z12 and Z14 cells of A15. Notably, it is clear that the flux trajectories through the walls of the Voronoi cells are clearly nonzero (flowing from Z14 to Z12), implying that faces of the Voronoi cells do not correspond well with the true terminal boundary, whereas the medial cell boundaries line up clearly with the boundaries between divergence regions of chain flux at the interface between opposing brushes between Z12 and Z14.

Lastly, we point out the subdomain thickness measures provided by the medial surfaces. Notably, for conformationally symmetric diblocks, the IMDS shapes of certain sphere-like domains of FK phases become greatly distorted into highly oblate, “discoidal”, shapes. For example, from the results shown in [Figure 9](#), the IMDS of the Z14 cells of A15 have roughly an oblate discoidal shape with a semimajor/semiminor access ratio of ~ 1.5 . For C15, the Z12 domains have similarly oblate IMDS

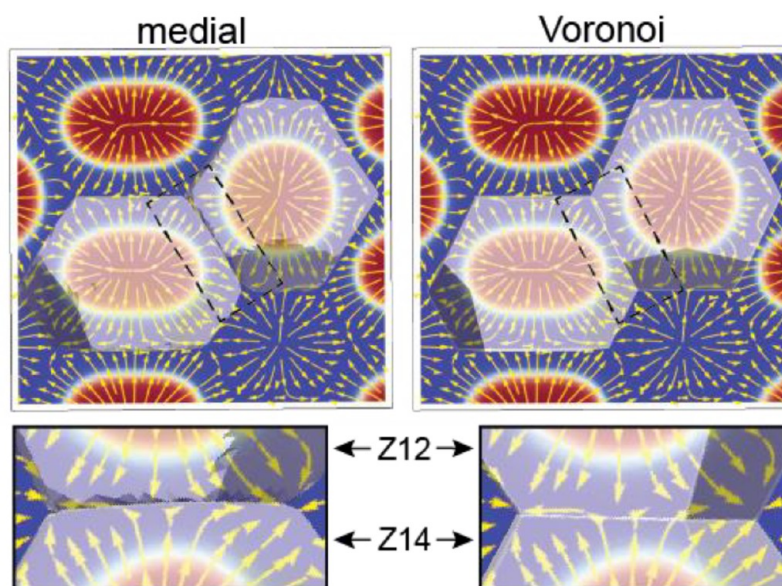


Figure 10. Chain orientation in A15 cells. Schematics show the stream plot (yellow) of vector order parameter in a (100) face of the A15 unit cell from SCF predictions at $f = 0.29$, $\chi N = 40$, and $\epsilon = 1$. Vectors, computed by using methods of ref 98, indicate the mean orientation (in-plane components) of chains at different positions (note that magnitude of polar order is not shown), while the color scale indicates the local composition field, with red and blue regions corresponding respectively to majority A and B segments. Superposed on vector order are the (outer) medial and Voronoi cells of one Z14 (lower left) and one Z12 (upper right), whose faces are shown as transparent white to allow for view of the underlying vector order. The highlight region in the black rectangle is shown at a larger scale below each, highlighting the fact that the “flux” pattern of chain orientation terminates on the medial cell walls between Z14 and Z14, but the flux pattern penetrates the walls of the corresponding Voronoi cells. The comparison highlights that Voronoi cells poorly capture true terminal boundaries between distinct coronal domains, while medial surfaces defined with respect to the IMDS serve as a much better proxy for the cellular volumes that enclose sphere-like BCP domains.

shapes. This shape is not unlike the oblate ellipsoidal example given in Figure 6, and indeed we find for these high aspect ratio domains that the interior medial boundary spreads out in that the domain as is visible for the respective Z14 and Z12 domains shown for A15 and C15 in Figures 9B and 9D. This feature indicates that these discoidal domains possess quasi-lamellar regions surrounded by high-curvature, quasi-toroidal, rims. In contrast, for the relatively spherical domains (e.g., Z12 of A15 and Z16 of C15) the inner medial surfaces bunch into fairly compact regions near the domain center (though not strictly points).

Hence, the medial perspective casts a wholly new light on the nature of packing frustration in the FK phases of BCP, in which the constituent domain shapes can be broken down into these two crude categories of quasi-spherical vs quasi-discoidal domains. The implications of this more complex subdomain shape distribution on the thermodynamic stability of FK phases (i.e., which of these competitor phases is stable; when and why are they favored over the canonical BCC packing?) remain to be explored.

III. MEASUREMENTS OF BCP MORPHOLOGY: FROM SUPRADOMAIN PERIODICITY TO SUBDOMAIN GEOMETRY

III.A. Early Observations of BCP Morphology. Anionic “living” polymers were first synthesized by Szwarc, Levy, and Milkovich in 1956, including the first block copolymers made by using polystyrene (PS) and polyisoprene (PI).⁹⁹ A few years later, Richards and Szwarc synthesized hydrophobic–hydrophilic BCPs based on PS and poly(ethylene oxide) (PEO).¹⁰⁰ These BCPs displayed curious optical texture and solution viscosity changes when a small amount of a nonsolvent for either block was added to the initially homogeneous clear solution. This prompted structural investigations of similar block copolymers at the CNRS in Strasbourg, France, in the Skoulios group starting in 1960.^{11–13} These studies revealed the similarity of lyotropic solutions of di- and triblock PS–PEO and PEO–PS–PEO copolymers to those of other low molar mass amphiphilic molecules under study at the CNRS. Morphological characterization of the BCPs in concentrated solution by POM and SAXS using both hydrophobic and hydrophilic solvents showed that the gel-like samples had birefringent textures similar to those known for lyotropic liquid crystals. SAXS revealed sets of Bragg peaks quite analogous to those already known for both lyotropic and thermotropic liquid crystals. The characteristic Bragg peak sequences suggested that, depending on BCP molecular weight (MW) and solution composition, periodic structures of 1D lamellae, 2D hexagonally packed cylinders,¹² and 3D (face-centered) cubic packed spheres¹⁴ could form. Figure 11 is the first published schematic of a BCP domain structure¹² showing the imagined (since as yet there was no direct structural observation at the required length scale) domain structure for cylindrical and lamellar phases for a concentrated PS–PEO diblock in either a PEO-preferential hydrophilic solvent (left) or a PS-preferential hydrophobic solvent (right). In the case where the solvent is entirely selective to the PS block, the stereoregular and hence crystallizable PEO block was found to undergo crystallization, and the proposed domain structure was that of chain-folded PEO lamellae alternating with noncrystalline solvent-swollen PS block layers.

These initial BCP structural investigations suggested that, as was the case with soap amphiphiles, by appropriate choice of preferential solvent(s) and concentration the sequence of

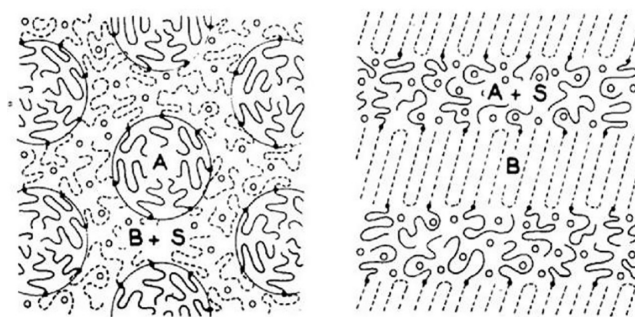


Figure 11. The first published BCP domain schematic (adapted from ref 13). The A block is PS, the B block is PEO, and the solvent is designated as S. (left) A hydrophilic solvent swells the B block and the A blocks aggregate into cylindrical domains packed on a hexagonal lattice. A hydrophobic solvent swells the A block, and the crystallizable B block forms thin chain-folded lamellae alternating with solvent-swollen A layers.

domain types from spheres to cylinders to lamellae to inverted cylinders to inverted spheres could be accessed. Skoulios suggested that BCPs could be thought of as “high molecular weight liquid crystals”.¹⁰¹ The early PS–PEO BCPs were of low MW and were studied in solution, enabling clear resolution in q vector (SAXS) with multiple Bragg peaks from the good long-range order. However, as of 1966, no one had directly observed the actual shapes and sizes of the supposed block domains, only inferring their presence, their mutual separation distances, and their likely shapes based on the textures seen in POM and from the sets of Bragg peaks observed in SAXS patterns.

With length scales of the domain dimensions and domain periodicities in the range of tens to hundreds of nanometers, optical microscopy could only detect the presence of birefringence in the supposed hexagonal cylinder and lamellar systems (and its absence in the hypothesized cubic sphere systems) due to the optical anisotropy of the domains and presumably also in part to the anisotropic orientation of the chains within these domains. It was not until 1966 that Vanzo¹⁰² working at Dow employed TEM of chromium shadowed silicon monoxide 2 stage poly(vinyl alcohol) surface replicas to demonstrate direct evidence of a lamellar structure in a high-MW polystyrene–polybutadiene (PS–PB) diblock (see images in Figure 12). However, since the technique used could only image the alternating layers at the sample surface and at unknown viewing angles, it was not possible to positively determine the individual layer thicknesses or the identity of a particular layer.

Structure–property relations for much higher MW samples that exhibited greatly enhanced mechanical properties were of strong interest to industry (e.g., Dow, BASF, and Geon). Some very high-MW samples also exhibited iridescent colors in solution and in dried films, which were thought to be due to some type of cholesteric liquid crystalline phase¹⁰² but later understood to be an effect of a photonic crystal structure (see e.g. ref 103). Shortly after Kato’s use of osmium tetroxide (OsO_4) to stain and fix PB latex particles,¹⁰⁴ three research groups published TEM micrographs of PS–PB block copolymers by microtoming melt-pressed samples and preparing thin solvent cast films.^{15–17} TEM images (see Figures 13A–D) showed that a microphase-separated morphology was clearly present as the high atomic number OsO_4 stain rendered the PB domains dark and the relatively unstained PS domains appeared bright. In specimens made by melt pressing or rapid solvent

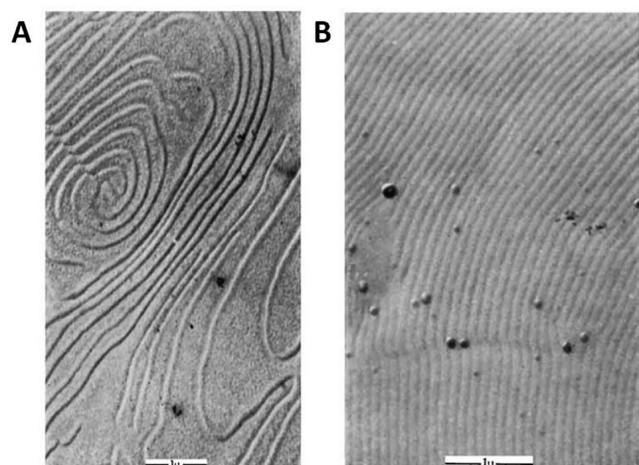


Figure 12. Surface replica of dried PS–PB film with (left) parallel lamellae showing growth spirals and surface steps and (right) edge-on lamellae (adapted from ref 102).

casting, the domain ordering was generally poor, resulting in highly overlapped 2D projections of irregularly shaped domains in TEM images. The desirable optical transparency of PS–PB–PS samples compared to the opaqueness of PS–PB blends of the same composition was attributed to the small PB “islands” in a PS matrix (Figure 13C). Very slow (28 days!) solvent casting of a 60/40 composition PS–PB diblock resulted in several micrometer diameter lamellar grains (Figure 13D).

Matsuo, Sagae, and Asai¹⁰⁵ also used solvent processing conditions that resulted in good long-range order, and their TEM images allowed clear visualization of the spherical and cylindrical domain interfaces (the IMDS) for the first time (Figure 14). Thus, researchers were now able to “see” the actual domain structure (composition distributions in real space) and could correlate the sizes and shapes of the domains to the particular block and its MW, noting that domain size increased with increased MW.¹⁷ Rapidly thereafter, many groups around the world conducted additional investigations to correlate the strong dependence of mechanical properties on the volume fraction, geometry, and topology of the BCP domains in a host of BCPs with varying composition, MW, and block number (diblocks, triblocks, and quatrablocks) and confirmed the three distinct types of domain structures: the canonical spheres, cylinders, and lamellae.¹⁰¹ These early studies suggested that it was only necessary to perform SAXS on the solvent containing or dry sample and TEM on a thin, dry piece of a specimen

(either a rapidly evaporated thin film or a slowly evaporated thicker film followed by microtoming and staining a thin section) to readily distinguish the domain shapes, periodicities, and topologies (0D spheres, 1D cylinders, and 2D continuous layers). The 3D domain shape was inferred via the TEM 2D image projections. Hence, the stripe patterns which could be interpreted either as lamellae or as transverse views of cylinders, and likewise, circular patterns as either spheres or axial views of cylinders were further identified by viewing many differently oriented grains (both views of cylinders are evident in Figure 14B). The subsequent introduction of TEM goniometer sample stages allowed analysis of a given region of the specimen at multiple tilt angles allowing distinction between the possible domain types.

The microtomed TEM sections as well as spin-coated solvent cast films are typically 30–100 nm in thickness with lateral areas spanning a grid square of perhaps 5000 μm^2 . The spatial resolution (in x and y) of the TEM instruments available in the 1960–1980 time frame was a few Angstroms, more than sufficient for domain visualization. Current TEM tools have resolution less than an angstrom, but the practical lateral resolution of TEM images is normally limited to ~ 1 nm due to several factors including the finite width of the IMDS, the projection of the composition profile through the specimen thickness, detrimental mechanical distortions from the microtoming process, preferential domain swelling via staining, and electron beam damage (which causes mass loss and is another source of dimensional changes of the specimen). With typical domain sizes of BCP in the 2–100 nm range, lateral resolution is still usually quite sufficient to assign a domain shape, but since typical specimen thicknesses (along z) can contain a few or tens of domains, the TEM images often display highly overlapped and complex projections that are hard (or nearly impossible) to uniquely interpret, let alone precise, the detailed IMDS curvatures and intradomain features. The introduction of TEM tomography (TEM-T; see section III.C.2) enabled more quantitative 3D visualization of the domains via the use of a large number of 2D projections taken as a systematic function of specimen tilt.

As researchers developed better sample preparation methods (in particular by using a neutral solvent and very slow evaporation, followed by high-temperature, long-time annealing; see section IV.A), this led to greatly improved long-range domain order corresponding to larger grains and fewer defects. Such samples enabled more quantitative SAXS studies from the greater number of Bragg peaks, helping to quantify how lattice periodicities and domain dimensions scaled with MW.^{17,106,107}

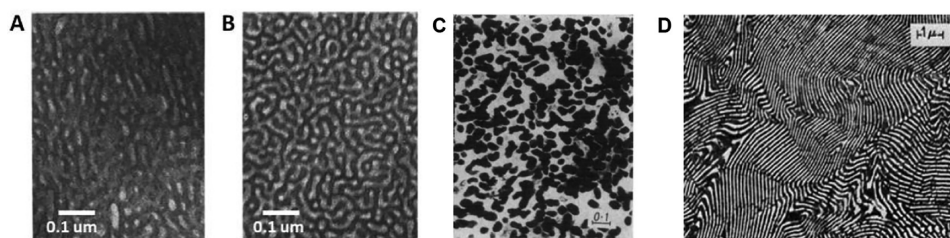


Figure 13. The first published bright-field TEM images of BCPs. (A) Microtomed thin section and (B) solution cast thin film of a PS–PB–PS triblock copolymer with 68% PS (adapted from ref 16). (C) Microtomed section of melt-pressed PSPBPS having PB “islands” in a 60% PS content (adapted from ref 15). These samples only have short-range order and exhibit irregular domain shapes and significant overlap of structural features in the 2D image projections, limiting interpretation (D). Microtomed section of very slow solvent cast high-MW (612 kg/mol) PS–PB lamellar film that showed a blue color (adapted from ref 17).

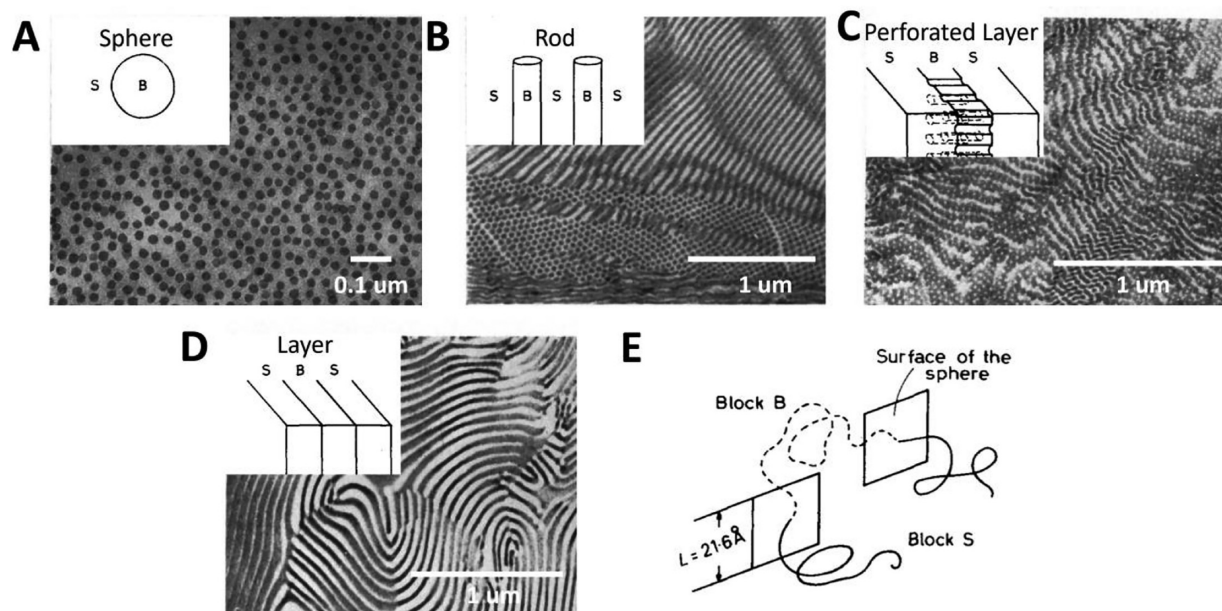


Figure 14. Bright-field TEM observation of ultrathin section solvent-free BCP with different domain morphologies with schematic diagrams of morphologies (adapted from ref 105). (A) Sphere morphology in polystyrene-*b*-polybutadiene-*b*-polystyrene (SBS, S/B = 80/20, mole ratio). (B) Cylinder morphology in polybutadiene-*b*-polystyrene-*b*-polybutadiene (BSB, S/B = 60/40, mole ratio). (C) Perforated layer morphology in an “ionic” (i.e., random block) copolymer (S/B = 60/40, mole ratio). (D) Layered morphology in SBS (S/B = 40/60, mole ratio). (E) Schematic diagram of effective area (L^2) occupied by one block chain which protrudes through the surface of the sphere of SBS BCP in (A).

Combining TEM and SAXS became the “gold standard” for identification of the morphology and quantification of its basic structure (i.e., D -spacing). Based on these approaches, schematic views of bulk, solvent-free BCP domain morphologies, including spheres, cylinders, and layers (and even a report of perforated layers “punched sheet”;¹⁰⁵ see Figure 14C) emerged by the late 1960s. While such idealized schematics did not address interdomain order and intradomain variability, they did envision several underlying concepts for subdomain chain packing, such as the interfacial area per chain (see Figure 14E) in analogy to the interfacial area per soap molecule, long recognized as an important quantity determining the selection of domain shape in lyotropic systems.

Scattering approaches, however, need samples possessing excellent long-range structural order to provide a sufficient number of Fourier components to distinguish the crystallographic space group and, in combination with recent developments of Fourier inversion (see section III.B), the detailed real space structure of the domain shapes. For example, in the early years, the 3D packing arrangement of spherical domains was thought to be FCC based on the nondefinitive analysis of only three relatively broad Bragg peaks (with q values in the ratio of $\sqrt{3}$, $\sqrt{4}$, and $\sqrt{8}$ ¹⁴) along with the intuitive notion that the minority component would take on a sphere-like shape and would likely assemble into a close-packed structure. Generally, BCP samples with spherical domain morphologies had quite poor long-range order, making a definitive assignment to a specific crystalline packing arrangement rather problematic and yielding no direct information about the precise IMDS shape. Leibler’s weak segregation theory,²² and subsequent extension to stronger segregation conditions by Ohta and Kawasaki,¹⁰⁸ predicted BCC packing of spherical domains. In 1987, a tilt goniometer stage equipped TEM and a very well ordered sample of polystyrene-*b*-polybutadiene BCP³⁶ allowed definitive imaging data for a tilt series from the [100] to the [111] and

to the [110] projections, uniquely matching the expected projected domain patterns and directions of tilt axes and degree of tilt for a BCC packing with the $Im\bar{3}m$ space group with the domain centers located on the two BCC lattice sites: Wyckoff site 2a (0,0,0) and (1/2, 1/2, 1/2). Notably in this work, heuristic arguments about the thermodynamics of packing malleable spherical domains were put forward to rationalize the selection of BCC over FCC and simple cubic lattices, which were later substantiated by more detailed strong-segregation theory²⁷ and then extended to consideration of complex FK phases.^{33,38,47} While the projected patterns in TEM satisfied those expected from cubic symmetry of BCC packed spheres, the precise 3D shape of the IMDS between domains was not directly measurable in the projections.

III.B. Beyond the Classical Morphologies. While exploring a series of PS–PI block copolymers with a novel type of star diblock architecture, an entirely new, 3D interconnected network microdomain morphology was discovered.^{23,109,110} The 3D continuity of both components was apparent not only from all the various TEM projections but also from the high value of the elastic modulus (stemming from the glassy PS subdomain continuity) and the high gas permeability (arising from the PI subdomain continuity). The initial publication described the structure as the ordered bicontinuous structure (OBS) without being able to specify a precise domain shape, unit cell, and space group.¹⁰⁹

Furthermore detailed analysis of both the real space projections and the reciprocal space scattering pattern suggested that (again in analogy with lyotropic liquid crystals) the new microdomain structure was based on the $Pn\bar{3}m$ cubic space group (similar to the structural assignment of a bicontinuous lipid–water phase based on characterization by SAXS).¹¹¹ Evidence from the relative positions of the four low- q Bragg peaks and especially from electron micrographs and their associated (albeit crude due to limited computational power and

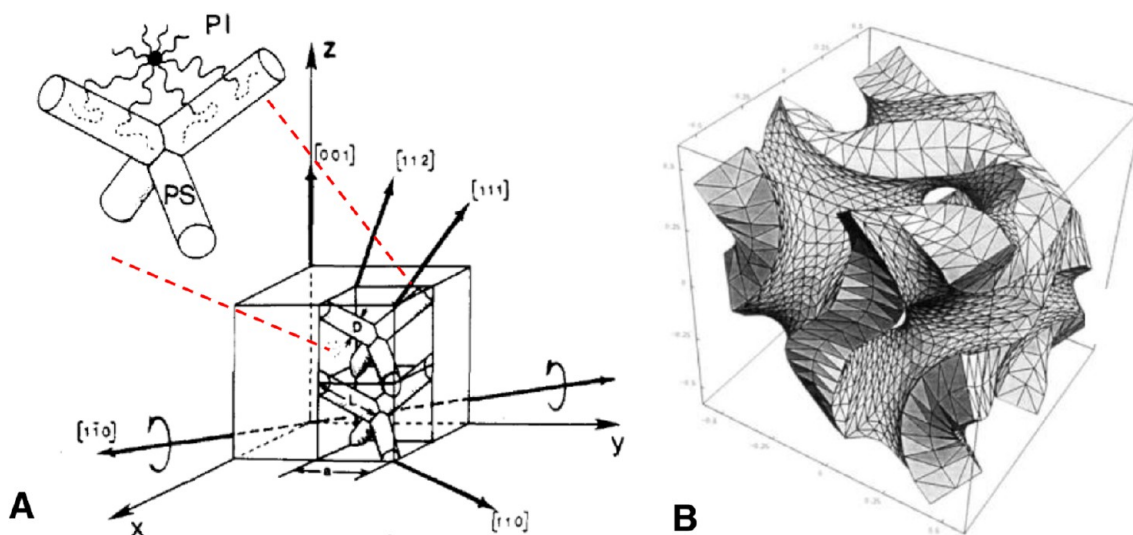


Figure 15. The first schematic models of cubic tubular network phases of BCP. (A) The double-diamond structure with space group $Pn\bar{3}m$ is composed of two interpenetrating diamond networks with tetrahedral nodes (adapted from ref 23). (B) The double-gyroid structure with space group $Ia\bar{3}d$ is composed of two interpenetrating networks with trihedral nodes (adapted from ref 112). The schematic shows the G TPMS with a constant matrix thickness (CMT) of the majority component. The two independent interpenetrating labyrinthine gyroid networks containing the minority block are the empty channels.

modeling software at the time) computer-generated simulations (see Figure 16A) pointed to two interwoven minority PS block

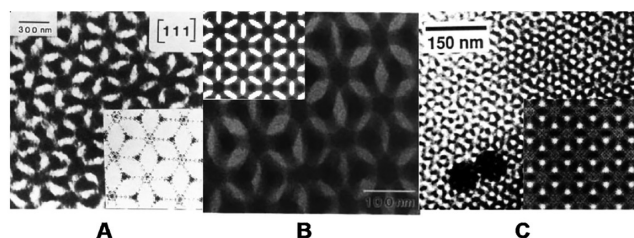


Figure 16. Bright-field TEM images from three different PS–PI BCPs taken along the $[111]$ “wagon wheel” projection direction and associated simulations. (A) Miktoarm star with 27 vol % PS using the ASU Multislice model compared to OBDD structure by a set of six equispaced points along $[111]$ struts (adapted from ref 23). (B) 1988 diblock with 62 vol % PS comparison using TEMsim employing a DD CMC surfaces (adapted from ref 66). (C) 1994 linear diblock with 33 vol % PS using TEMsim based on a CMT G TPMS model (adapted from ref 112). Attribution of OBDD morphology in (A) and (B) was later reevaluated and concluded to be DG.

networks, each network having tetrahedrally connected PS units in diamond symmetry, with the OBS now renamed the ordered bicontinuous double diamond (OBDD).²³ However, while the matches in real and reciprocal space were seemingly quite close to the experimental data, due to the limitation of SAXS peak resolution using a 1D line-focus laboratory Kratky camera and as a consequence of the similarity of high-symmetry projections of a cubic tubular network structure, the published OBDD structure, although based on both reciprocal and real space data, turned out to be misidentified.²⁴ The error in assignment of the bicontinuous structure was not realized until about a decade later with the discovery of another bicontinuous tubular network structure occurring in a simple linear PS–PI diblock with similar composition.¹¹² This new phase, initially called the gyroid*, was also bicontinuous, composed of two interpenetrating, trihedrally

connected minority component block networks with space group $Ia\bar{3}d$. The strong similarity of the high-symmetry TEM images and the similar ratio of the first pair of allowed Fourier peaks (OBDD: $\sqrt{3}/\sqrt{2} = 1.23$ vs DG: $\sqrt{8}/\sqrt{6} = 1.15$, a difference of only 6%) of the new linear diblock DG phase to the older star diblock OBDD phase suggested that the star diblock structural assignment should be checked. A re-examination of the original star diblock sample with a fine spot-focus X-ray beam enabled superior resolution and showed the ratio of Fourier peaks was a better match with the $Ia\bar{3}d$ space group (DG) as opposed to the $Pn\bar{3}m$ space group (DD).²⁴ An improved domain structural model based on using the gyroid TPMS as the terminal surface of the outer PI blocks with the PS channel domains defined by constructing a constant thickness PI majority subdomain structure is shown in Figure 15B. Image simulations using TEMsim software developed at the MSRI in Berkeley¹¹³ showed that the three highest symmetry experimental TEM projections (the $[100]$, $[111]$, and $[110]$) corresponded well to those of the DG model, including the characteristic “wagon wheel” pattern imaged when viewing along the $[111]$ direction (Figure 16).

The ambiguity in assigning the domain morphology of bicontinuous cubic networks in BCP derives from not only just the limits of the characterization methods but also the need to rely on prior knowledge of the assumed phase structure, i.e., 3D spatial models of the domain composition, since both the TEM and SAXS data miss certain critical information about the 3D composition profile. For TEM, this derives from the 2D projection through a finite thickness of a 3D structure, while for scattering, this derives from loss of phase information about the interfering waves, the loss of wavevector direction uniqueness (e.g., radial averaging from a polygrain sample), and damping of Fourier amplitudes at higher wavevector (g_{hkl}^* which carry information about the fine scale details of domain shape). With a well-established prior model of the BCP morphology, it is often possible to “fill in the gaps” from this missing structural information, but this is obviously problematic for distinction between similar structures and impossible to do for previously

unknown morphologies. This points out the need for 3D tomographic reconstruction of such complex morphologies so as to be able to unambiguously distinguish the detailed shapes, topologies, and geometries of the domains.

Notably, the ambiguity in experimental assignment of DG as the stable network morphology of diblocks nearly parallel the theoretical understanding. After the apparent experimental observation of OBDD, strong segregation theories were constructed to consider the most favorable bicontinuous cubic network,^{27,53} but did not consider DG as a candidate morphology in the first such calculations, and hence initially pointed to DD as most stable network morphology at the boundary between cylinders and lamella. The equilibrium stability of DG was not assessed until 1994 when Matsen and Schick motivated by its recent experimental observation¹¹² and armed with a powerful spectral implementation of SCFT demonstrated that DG was equilibrium network phase for linear diblock melts at weak and intermediate segregation strength.⁶⁰ Subsequent SSL calculations^{28,29,56} then reassessed the bicontinuous morphologies and found that DG was the lowest free energy among them, although the predicted free energy of all bicontinuous phases exceeded classical morphology competitors. The question of theoretical stability of the DG, or other bicontinuous networks, in the $\chi N \rightarrow \infty$ limit remains a matter of continued debate to this day.^{9,114}

III.C. Methods for Precise 3D Structure Determination: from Supradomain Symmetry to Subodomains. As we have seen, the appearance of complex tubular network phases as well as the Frank–Kasper sphere phases has made it imperative to create a true 3D reconstruction of a periodic structure to correctly and more fully understand the structure, especially since we are interested in not just identifying the structure but quantitatively addressing why a specific type of BCP molecule assembles into a particular structure. Thus, further analysis of for example, the distributions of curvatures over the IMDS and the distribution of various measures of domain thickness are very useful for critical comparison to and testing of various theoretical models. Structural feature resolution in all of the experimental characterization techniques depends on having excellent specimen long-range order and hence the ability to reliably measure and include the weaker higher order (high frequency) reflections via improving signal strength by the contribution of scattering from many coherent unit cells. The known physical constraints for reconstruction include the electron density of each component, molecular weight, and volume fraction of each block. Presuming a very well ordered specimen, a precise 3D experimental representation of the structure at the scale of 3–100 nm can currently be accessed three ways: (1) by Fourier inversion of the SAXS scattering pattern, (2) by “back-projection” of a large set of systematic TEM 2D projections, and (3) by registration of a stack of images obtained via sequential ion beam slicing of the specimen and scanning secondary electron beam imaging of each newly ion milled surface. Next we highlight each of these approaches.

III.C.1. Small-Angle X-ray Crystallography. In recent years, soft matter researchers have adopted the traditional approach¹¹⁵ of wide-angle X-ray crystallography via Fourier synthesis to create 3D reconstructions of periodic soft matter structures, where due to the increased length scales, small-angle rather than wide-angle scattering data are acquired.¹¹⁶ Small-angle X-ray crystallography (SAXC) normally uses a synchrotron X-ray beam enabling a fine probe (~ 100 – $500 \mu\text{m}$ diameter) along with a multiaxis sample goniometer to obtain diffraction data.

There are two particularly useful types of samples: fine powders and large single crystal grains. For an isotropic, fine grain size polycrystalline powder sample, the spherically averaged 1D scans of $I(q)$ data include superposition of signals coming not only from different peaks having the same or nearly the same $|q|$ vectors but also from unit cells in many grains having a wide range of local environments which often leads to peak broadening. Alternatively, employing a very small X-ray beam along with a large single grain specimen and goniometer stage enables quantitative measurements of each individual Bragg peak. SAXS patterns are often recorded from samples having a mixture of grain sizes and partial orientation and so exhibit arced, spotty Bragg rings and include a strong asymmetric scattering background arising from limited long-range order, compositional fluctuations, and the presence of various types of sample distortions and defects. The scattering pattern in reciprocal space is the product of the Fourier transform of the real space electron density composition and its complex conjugate:

$$I(\mathbf{q}) = \left| \int dV e^{i\mathbf{q}\cdot\mathbf{x}} \phi(\mathbf{x}) \right|^2 \quad (8)$$

A real space electron density map then requires “inverting” $I(\mathbf{q})$ to recover the real space composition field, $\phi(\mathbf{x})$. However, while the scattering amplitude of a peak can be simply extracted from the background corrected peak intensity, the information about the phases of the scattered waves is lost. These phases essentially have to be inferred; this is generally known as the “phase retrieval” problem.^{117,118}

To obtain a successful, high-fidelity reconstruction, SAXC experiments need many well-resolved, independent reflections to converge on a real space structure. Real space structures can be obtained via many approaches. One method which depends on prior assumption of a solution takes the direct measurement of the Fourier component amplitude, A_{hkl} , from the square root of the experimental intensities of the Bragg peaks and pairs each peak with the phase of simulated peaks based on a numerical Fourier transform of a hypothetical prior real space model(s). Another more recent approach uses a computational algorithm to confront the phase retrieval problem with reduced bias. Here we focus on one such approach, called SUPERFLIP,^{116,119} which has recently been applied to complex sphere phases of BCP.^{41–43,120}

In this approach, peak amplitudes, widths, and q values of the Fourier components are assigned again from the experimental intensities. In applications to BCP structure, as well as similar morphologies of soft lyotropic assemblies, the space group, directions, and orientations of unit cell parameters are also chosen as inputs based on agreement with the apparent set of allowed peaks. Then the algorithm initially assigns random phases to each peak, with families of peaks sharing the same phase according to the input space group symmetry. A trial real space reconstruction is made by Fourier inversion, and in locations where the electron voxel densities are unphysical (i.e., negative), the program flips the sign of the particular reconstruction voxel. Next, this new electron density distribution is Fourier transformed back to \mathbf{q} space, and the peak amplitudes are compared against the experimentally extracted values. A new reciprocal space representation of the structure with the transformed phases and the original input Fourier amplitudes is then again back-transformed to real space, and any negative voxels are again flipped in sign. The process continues until possible convergence. Typically, thousands of inputs are

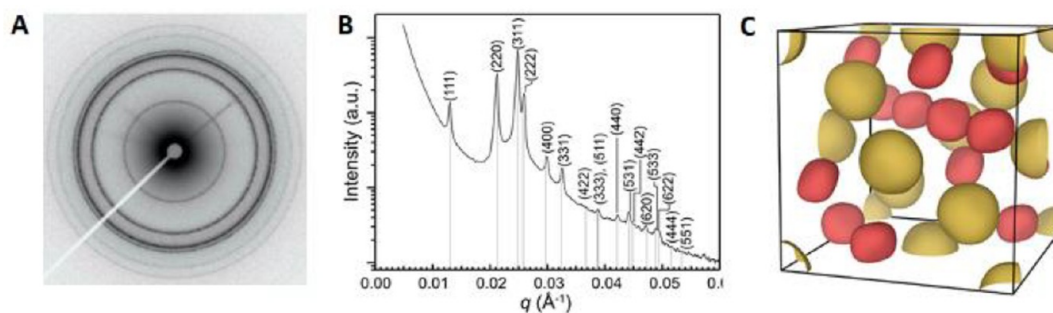


Figure 17. 3D X-ray reconstruction of BCP crystal. (A) SAXS powder pattern for a PS–PB and hPB blend; (B) the circularly averaged radial $I(q)$ vs q plot. 10000 trial runs starting with random phases and retaining the original amplitudes converged 70 times. (C) The 90% isosurface of the minority PB domains for the assumed $Fd\bar{3}m$ space group of the Frank–Kasper C15 phase, from the “average Fourier image” of converged phase solution (figures adapted from ref 42).

run, yielding ~ 50 – 100 converged solutions, each of which has the measured Fourier amplitudes and a set of phases whose real-space structure has non-negative electron density. Note that the phases of any given Fourier mode may not be identically assigned in each of the distinct converged solutions.

An example of such a construction is shown Figure 17 for a FK C15 phase formed in a blend of PS–PB BCP and PB homopolymer.⁴² The SAXS powder pattern indicates the sample consists of a nearly isotropic set of small grains. There is strong diffuse scattering at low q between 0.02 – 0.03 \AA^{-1} . The SUPERFLIP reconstruction was based on assuming the $Fd\bar{3}m$ space group for the input peak amplitude data for most (but not all) of the index peaks in the radially averaged synchrotron SAXS pattern shown in Figures 17A,B. Isocontours of electron density (90% of the maximum value) are shown as yellow and red domains corresponding to the Z16 and Z12 sites of the FK C15 structure. The significant apparent size and shape asymmetry of these domains are consistent with their attribution as the core region of sphere-like domains, arrayed on the distinct Wyckoff sites 8a and 16d of the $Fd\bar{3}m$ space group.

At present, these SUPERFLIP reconstructions are largely used as “consistency checks” for the gross topology of BCP domains, as opposed to quantitative metrics of subdomain shape (i.e., distributions of domain thicknesses and IMDS curvatures). While it may be possible to extend Fourier inversion methods for direct comparison with theoretical predictions, careful consideration of the prior assumptions and the exclusion of incoherent scattering contributions would need to be assessed.

III.C.2. TEM Tomography. The first transmission electron microscopy tomography (TEM) reconstruction of any BCP structure was done by Spontak et al. in 1988 on hexagonally packed cylinders.¹²¹ A DG structure was first analyzed by TEM using a binary diblock blend, again by the Spontak group¹²² and a triblock BCP melt in 1997.¹²³ TEMT uses a series of 2D projection images taken at various intervals of specimen tilt to create a 3D reconstruction of the sample via a back-projection algorithm without any prior assumptions on structural symmetry.¹²⁴ Details of this method relevant to soft matter are given in a review by Jinnai, Spontak, and Nishi.¹²⁵ The reconstructions of the DG were unprecedented and broadly confirmed the expected trihedrally connected interpenetrating network morphology. Looking back at the first reconstructions, one notices that apart from visualizing the network topology, the technique, as practiced at that time, did not provide sufficient fidelity to enable the extraction of subdomain information. This was principally due to the use of large tilt increments between images in the tilt series along with a limited tilt range. Such

limitations cause degradation of the reconstruction (principally along the sample thickness direction) due to the information that is not included in the back-projection algorithm, over-sampling of low-frequency Fourier components, and under-sampling of the higher frequencies.

A much improved DG reconstruction was done a few years later by the Jinnai, Spontak, and Hashimoto team^{77,126} using smaller increment tilt angles and a larger range of tilt. This 3D reconstruction permitted, for the first time, measurement of the IMDS curvature, node functionality, Euler characteristic, and associated topological genus value. Since this pioneering work, many other BCP structures have been investigated by TEMT, including the rediscovery and validation of the OBDD (see Figure 18) in a number of BCP systems including BCP blends¹²⁷

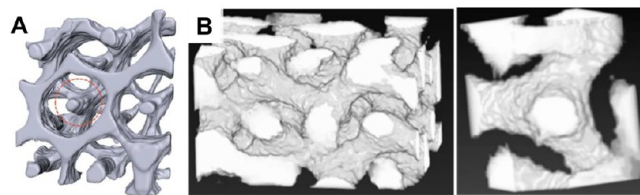


Figure 18. TEMT 3D reconstructions of the double-diamond structure. (A) A syndiotactic PP–PS diblock with the 46% sPP block comprising the two tetrahedral networks (adapted from ref 128). (B) DD structure in a ternary blend of three PS–PI diblocks (adapted from ref 127).

as well as fascinating order–order thermotropic transformations between the DD and DG in diblocks of polystyrene and syndiotactic polypropylene.^{128,129}

While current TEMT methodology can ascertain the 3D connectivity of complex structures, there are limitations on the fidelity of the reconstructed structure, particularly the detailed shape of the IMDS and the associated subdomain thicknesses. These limitations include the detrimental influence of the “missing wedge” of information in the reconstruction due to the inability to acquire 2D projections of the thin sample over the full tilt angle due to the geometric limitations of the microscope goniometer stage and multiple scattering at high tilt angles since the beam path along the projection direction grows with tilt (i.e., as secant of angle). Additionally, as mentioned previously, distortions occur due to microtoming of the thin section, and there can be substantial electron beam specimen damage and associated dimensional changes due to the requirement to record hundreds of consecutive images of a single area. Because of the thin sample and high magnification used, the statistical

sampling is limited since a volume typically containing only tens to hundreds of unit cells is reconstructed. A comparison of different experimental techniques used to measure the supra- and subunit cell structural information (curvature of the IMDS) to geometric models of DG (i.e., CMT vs CMC shapes) is discussed in the next section (see Figure 21).

III.C.3. SVSEM Tomography. Another real-space approach, which works very well for BCPs, that does not depend on phase retrieval or suffer from loss of information in the “missing wedge” is slice and view scanning electron microscopy (SVSEM), also known as focused ion beam-scanning electron microscopy (FIB-SEM). Here a dual ion beam, electron beam instrument is used to alternatively slice a thin (e.g., ~ 3 nm) slice from a bulk specimen by using the ion beam, followed by using the electron beam to capture a low voltage secondary electron image of the near-surface region of the newly exposed sample surface. The next image is made by again using the ion beam to slice off a thin planar section and acquiring another secondary electron image of the newly exposed surface region. The main influence of the researcher on the data is only in the segmentation (binarization) of the images which is constrained by the known volume fractions of the two components. Computer registration of a large number (hundreds to thousands) of images results in a quite large volume 3D reconstruction. For BCP structures with unit cells on scale of 50 nm or more with feature sizes >10 nm, the SVSEM technique can provide excellent structural information for critical comparison to theory.^{78,130,131}

Figure 19 shows an example of a 3D SVSEM reconstruction created by registration of a stack of 214 image slices of a polystyrene–polydimethylsiloxane (PS–PDMS) that forms the DD structure. The DD sample¹³² was cast from a PS–PDMS

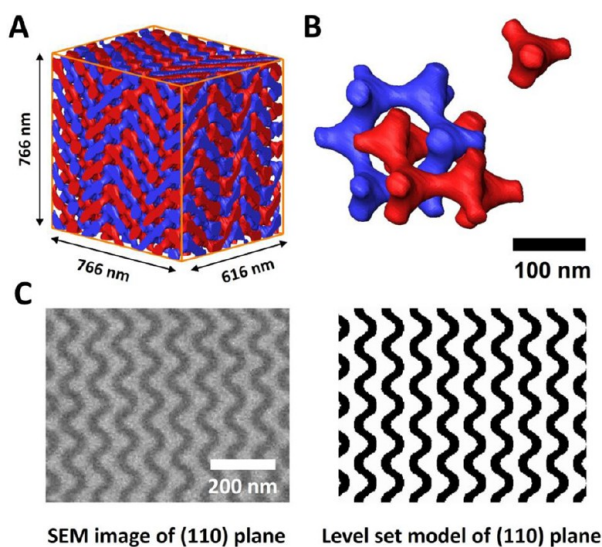


Figure 19. Slice and view tomography of a 51–35 kg/mol PS–PDMS DD. (A) Portion of the reconstruction containing ~ 500 unit cells. (B) A cropped region showing a portion of the two interpenetrating $6-4^6$ networks. The PDMS tubular networks within the reconstruction are rendered into color, and the PS matrix is rendered to be transparent. A cropped tetrapodal node is shown at the upper right. (C) SEM image of a (110) plane within the structure and the corresponding image based on a level set model of the DD. The 40 vol % PDMS block is much brighter than the dark PS block regions due to the increased secondary electron signal from the Si and O atoms in PDMS.

(51 kg/mol for PS block and 35 kg/mol for PDMS block) 5 wt % chloroform solution. The acquisition and SVSEM analysis of DD follow the procedure reported in ref 78. An enlarged region of the structure (Figure 19B) shows the fundamental $6-4^6$ catenated loop structure of the two independent diamond networks. Unlike in TEM, where each image is a projection through the entire film thickness (~ 100 nm) and for complex 3D network structures always involves substantial overlap of the fine scale features, in SVSEM, by using a low keV electron beam, each image approximates a near 2D slice of the 3D structure. This allows very detailed comparison of data sets with 3D models of a given structure made from SCFT computations, level set, CMC, or CMT models of the structure based on the known component volume fractions. Figure 19C shows the raw SEM image and the corresponding level set model for a (110) plane of the DD structure. Moreover, one can produce synchronized systematic slice by slice sequences for critical comparison of data and model not only for the fundamental unit cell structure but also for defects, for example coherent growth twin boundaries that occur in the DG phase.¹³¹

In the SVSEM reconstructions (Figure 19), the IMDS is taken as the locus of points where the bright (PDMS) voxels meet the dark (PS) voxels as determined by the image segmentation. Importantly, ion and electron beam damage are minimal as a given specimen region is only exposed once for slicing and once for imaging. Furthermore, unlike scattering methods that provide only Fourier component amplitudes (and need assumptions on the phase information about a given hkl Bragg peak), performing a 3D FFT of a reconstruction containing an array of coherent unit cells directly yields both amplitude and phase information about every peak as well as “off-peak” scattering, which gives information about distortions of the structure at the interunit cell scale. Furthermore, by appropriate placement of a set of Bragg filters to select peaks, followed by inverse Fourier transformation with both experimental amplitude and phase information, an improved, higher resolution 3D structure can be created with greater signal-to-noise ratio due to the statistical averaging over a $N_x \times N_y \times N_z$ array of coherent unit cells. Notably the fidelity of this average image is improved by the especially large volume of data acquired with good long-range sample order. While the voxel dimensions compared to that of the unit cell suggest a nominal linear sampling rate of many tens of voxels per unit cell, Fourier averaging effectively superposes the signals of the $N_x \times N_y \times N_z$ coherent cells into a single domain, enhancing the resolution in the averaged structure. This same diffraction data can be used to unambiguously determine the space group by using the diffraction vectors, allowed peaks, and their phases. Moreover, one can choose a single grain region of interest from within the large reconstructed volume that excludes any defects. To correctly compare the 3D FFT of the SVSEM reconstruction to SAXS diffraction, the grayscale intensity of the 3D reconstruction needs to be linearly proportional to the electron density of the sample. This reciprocal space information can also be compared with Fourier information generated by using specific theoretical models.

Bragg filtered SVSEM data can be used to analyze subdomain morphological metrics of IMDS shape and domain thickness. Figure 20 shows analyses of the DG morphology obtained as described in ref 78. Notably, this method does not require any prior assumptions about the space group, and in particular, it was observed that the PS–PDMS DG studied in ref 78 exhibits a triclinic variant of the idealized cubic DG morphology, which

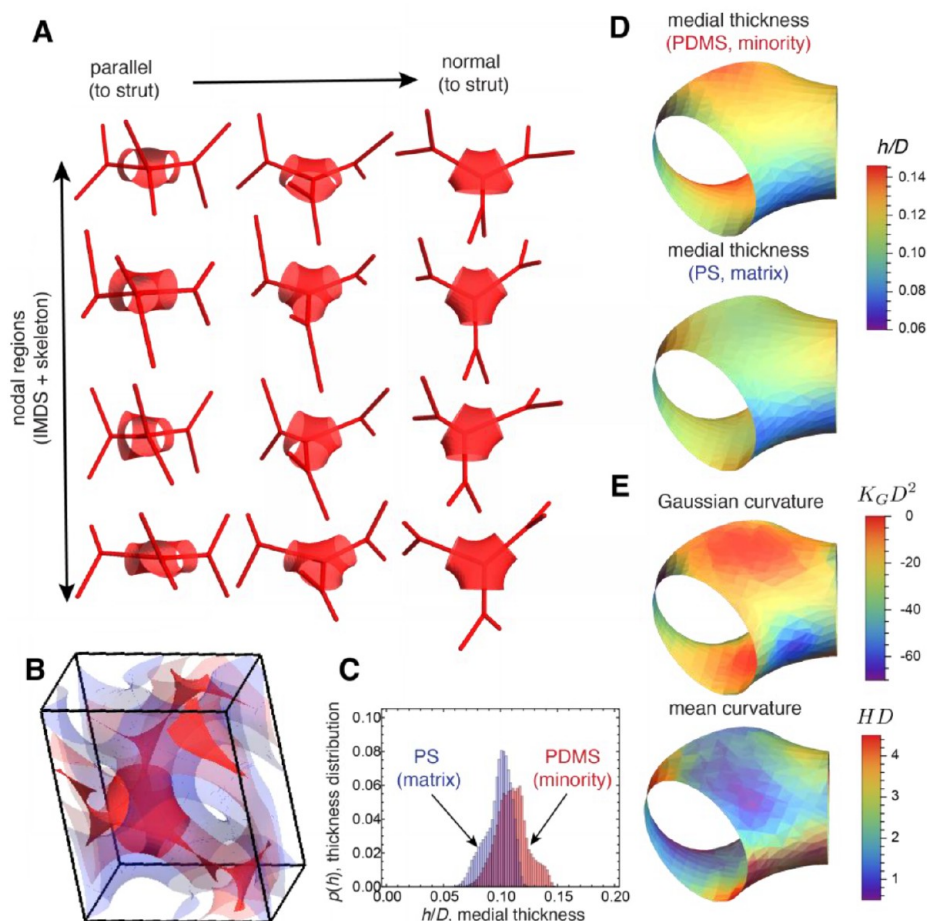


Figure 20. Subdomain distortions and morphological metrics from SVSEM experiments. IMDSs and associated skeletal graphs of four specific 3-valent nodal regions from Bragg-filtered PD–PDMS DG SVSEM reconstruction (ref 78), shown in different viewing perspectives in (A). The first row depicts the nodal region highlighted in (B), (D), and (E), and the remaining three rows depict the same features for its three neighboring nodes. The triclinic DG unit cell from SVSEM is shown in (B) with only one PDMS tubular network IMDS (light red) and associated medial surfaces for tubular subdomains (dark red) and matrix subdomain (light blue) and the IMDS nodal region from first row of (A), highlighted in dark red. Medial thickness distribution (for the entire Bragg filtered reconstruction) in (C) highlights the subdomain inhomogeneity for both PS and PDMS domains. Local variation medial thickness for PS and PDMS subdomains is depicted by coloring each pixel on IMDS at nodal region (D), while (E) shows the local variation in mean and Gaussian curvature for the same region.

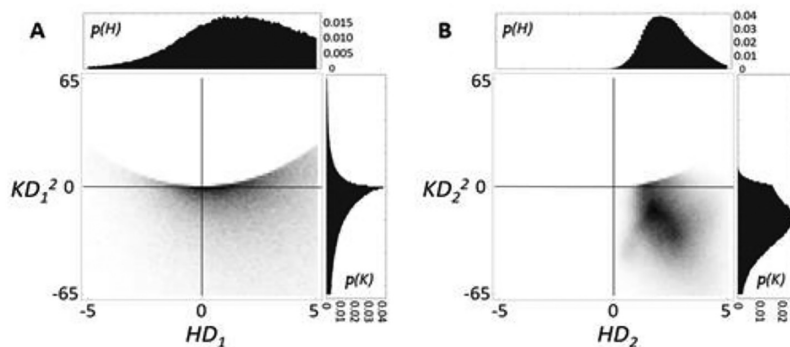


Figure 21. Gaussian (K_G) and mean (H) curvatures of the IMDS and their respective probability functions of BCP DG reconstructions from TEMT (A) and SVSEM (B). TEMT DG reconstruction is based on DG forming polystyrene-*b*-polyisoprene-*b*-polystyrene with polystyrene as the minority tubular networks (volume fraction of 32%), the averaged unit cell parameter $D_1 = 74$ nm (data from ref 77); SVSEM DG reconstruction is based on DG forming polystyrene-*b*-polydimethylsiloxane with polystyrene as the minority tubular networks (volume fraction of 40%), the averaged unit cell parameter $D_2 = 130$ nm (data from ref 78).

was attributed to stresses encountered during the non-equilibrium process of domain ordering from solution casting. Figure 20A shows the IMDS from multiple views of four

different 3-valent nodal regions from the triclinic DG in Figure 20B. SVSEM reconstruction captures both the alteration of the periodicity at the unit cell repeats and local rearrangements of

the shapes of the subdomains in the structure. Unlike the perfect cubic DG, which contains two enantiomeric sets of equivalent nodal regions associated with the Wyckoff 16b positions, in the experimental triclinic DG nodal regions are no longer equivalent and exhibit distinct and distorted shapes. Medial thickness analysis (Figures 20C,D) shows variation in block stretching in both PS and PDMS domains and spatial variations in curvature (Figure 20E). While the gross patterns of negative curvature and local thickness are similar to the idealized cubic models in Figures 3 and 7, nodal regions of PS–PDMS DG exhibit spatial fluctuations of shape far from the ideal $\sqrt{3} \times \sqrt{3} \times 2$ point group symmetry. Hence, SVSEM reconstruction provides avenues to access and quantify variability of the subdomain shapes in a way that captures the effects of distortion and domain malleability intrinsic to BCP assembly.

Beyond the purely local mapping of subdomain shape, the large volumes of SVSEM reconstruction make it possible to analyze morphological features over statistically large sample volumes. That is, in SVSEM quantitative structural information is not obtained by measurements from just a handful of unit cells in a thin TEM section but from 50–1000s of coherent unit cells within a single grain. Because of the ability of SVSEM to image over tens of cubic micrometers, data from many adjacent grains can also be acquired, greatly improving the statistical significance of the analysis while avoiding superposition of data from different sample environments.

In Figure 21, we compare the distributions of mean and Gaussian curvatures that can be measured from BCP DGs via two different tomographic techniques: TEMT in (A) and SVSEM in (B). Although there are differences in the experimental conditions and polymer chemistries for the two physical samples (i.e., the TEMT is from a OsO₄ stained, microtomed PS–PI–PS triblock, MW = 83 kg/mol with 0.32 volume fraction PI while the SVSEM sample is from a PS–PDMS with MW = 72.5 kg/mol having 0.40 volume fraction PDMS), normalization of the curvatures relative the unit cell parameters provides a useful basis of comparison for curvature measurement from two examples of nominally the same experimental DG morphology. Among other differences, it can be noted that curvature distributions measured by SVSEM reconstructions are somewhat tighter than from TEMT. In particular, the clustering of IMDS shape measurement around a quasi-1D region in H and K_G space is similar to what is found from SCFT predictions in Figure 5, although it must be noted that curvatures from SVSEM reconstructions show significantly broadened distributions from theory. It remains how much of the measured shape variability of this SVSEM can be attributed to fluctuations and distortions in the particular experimental realization of DG and how much can attributed to fundamental limits of resolution of the 3D reconstruction itself (i.e., sampling at finite voxel size over a finite 3D volume BCP sample).

IV. OUTLOOK AND FUTURE DIRECTIONS

In this Perspective, we have aimed to overview advances in the ability to experimentally measure and to theoretically model BCP morphologies at the subdomain scale and to connect the characteristic structural features to the underlying thermodynamic aspects of chain packing in complex phases. Largely for the purposes of clarity, we have focused on the presentation of the simplest of BCP designs—linear AB architectures. Next, we discuss some of the challenges and opportunities for extending and applying these concepts and methods to problems of current and future research and ultimately for understanding their

implications for material performance. We start with the need to improve processing of BCPs in 3D to achieve highly perfect structures as has been already well accomplished by directed self-assembly of thin (one domain thick films) in 2D.^{133–136}

IV.A. Processing Pathways for Near-Equilibrium BCP Morphologies. Similar to the situation in protein crystallography, where the ability to grow large, distortion-free single crystals is key to the successful high-resolution structural determination, precise and accurate measures of the subdomain features of BCP morphologies also rely on the growth of highly perfect BCP crystals. With BCPs, the crystalline order (i.e., long-range periodicity of the microdomains themselves) is strongly processing-path-dependent, indicating that resultant morphologies are likely at least slightly out-of-equilibrium for almost all BCP experimental systems at the point of measurement. The physical origins of the nonequilibrium behavior of BCP structures are well-known, stemming from the slow dynamics of high-MW chains, which maybe be both highly entangled and/or glassy at their final temperature and concentration, combined with numerous energetic barriers and slow relaxation processes associated with domain formation and rearrangement. Thus, comparison to the equilibrium structure found by theoretical computation is often (even, usually) problematic. Essential to the success of future high-resolution 3D studies and their critical comparison to computational results will be the ability to have specimen processing and sample preparation methods for morphological examination such that the structural information collected is not biased by such factors as solvent shrinkage and superposition of signals from multiple types of (variously distorted and oriented) environments. However, as is evident from most experimental studies, the high-MW specimens that are investigated are inevitably strongly segregated and therefore cannot be driven into a homogeneous disordered state by raising the temperature above their ODT due to the onset of thermal degradation. Thus, solvent casting is universally used to start from a homogeneous (dilute solution) state and to greatly accelerate the dynamics as BCP chains undergo domain formation and ordering, although this process itself presents additional challenges. First, as solvent is removed from the system, it is preferable to maintain constant relative volume fractions of the components once the system undergoes phase separation so as to avoid the ensuing shifted domain structure corresponding to alternative volume fractions, which requires a neutral solvent for BCP components. Such a neutral solvent is of course only possible for two component samples. Moreover, the onset of the disorder to order concentration (ODC) is likely preceded by the formation of molecular aggregates, in all probability, micelles of some form. The subsequent details of the nucleation and growth of the microdomain morphology from an assembly of such aggregates are still relatively poorly understood with most studies employing light scattering and SAXS vs temperature and vs polymer concentration to detect changes in the structures present in the solution. While an increase in the small-angle scattering signals the onset of structure formation, little can be inferred about the details of the structure(s) present and how these entities combine and evolve with the extent of the transformation from homogeneous solution to micellar fluid to the long-range ordered (i.e., crystalline) solid. A useful way to appreciate the various possible structural pathways is to view the “block copolymer solution phase cube”¹³⁷ that features three orthogonal axes for the equilibrium temperature T (or χN) vs BCP composition f vs BCP volume fractions ϕ , in the binary solvent-BCP phase diagram, as shown in Figure 22.

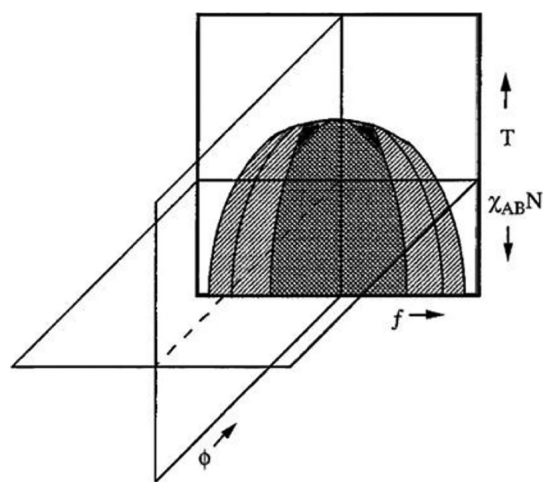


Figure 22. Schematic illustration of the block copolymer solution phase cube as a function of temperature (T), copolymer composition (f), and copolymer concentration (ϕ). The shaded plane corresponds to the melt phase map (schematic adapted from ref 138).

How the domains and ordered multidomain grains grow, for example, by the addition of individual chains and/or by addition of micelles or some type(s) of aggregate remains basically an open question. As often occurs in phase transformations, the kinetically most favored structures will likely form first and become long-lived metastable structures or (partially) transform to the more stable equilibrium structures. Low-MW and/or low- χ systems can be taken into the homogeneous disordered melt state thermally, and provided that the ordering transition is above the higher glass transition temperature (T_g) component, these systems can be studied at quasi-equilibrium without the complication of the presence of solvent. For samples prepared via the homogeneous melt route, if cooling is done slowly and avoids strong gradients, then thermal stresses (and their effects on domain morphology) can be mitigated.

Even if one can promote the correct phase (i.e., the phase that corresponds to the equilibrium state at the final concentration and temperature), distortions nearly always occur during self-assembly and growth of BCP crystals,^{78,138–140} for two essential reasons. First, unlike atomic and molecular crystals, structural building units in periodic BCP are themselves composed of large numbers of highly deformable collections of molecules. A typical triply periodic BCP phase has a unit cell that includes thousands of chains (each of which is high MW, so millions of atoms in total). Second, sample preparation most commonly involves casting a specimen from a room temperature solution, and the formation of ordered phase(s) proceeds via nucleation of small grains throughout the volume, growth of the grains along with additional grain nucleation, until grain–grain impingement forms grain boundaries. With most BCP samples, casting is in the shape of a large area thin film, so solvent evaporation occurs only in the vertical direction and generally the structure maintains its area while decreasing its thickness. Thus, the solvent-swollen structure experiences 1D shrinkage forces primarily along the normal to the film surface. Depending on the type of ordered phase and the particular local grain orientation, these shrinkage forces occur along various crystal directions. Film shrinkage can range up to the order of 500%. And even if the experiment is conducted such that the local structural relaxation time (i.e., the time required for motions of BCP molecules to adjust within their subdomain) is shorter than

the time required for the solvent to be removed, unless shrinkage is isotropic or new unit cells are grown or dissolved to allow for commensuration of the film dimensions and the evolving unit cell parameters, stresses and domain shape distortions will appear. In thicker samples, concentration gradients increase across the film thickness as the near-surface region dries and vitrifies. Because the domain structures are mechanically anisotropic, the variously oriented regions respond differently, leading to distorted unit cells having different lattice parameters and, for the 2D and 3D ordered phases, variable angles between the cell axes.

The common SAXS analysis protocol of spherical averaging of scattering patterns often masks the anisotropy present. Also, SAXS patterns are frequently only taken with the beam directed along the normal to the film surface, that is, along the principal shrinkage direction, such that often any anisotropy will not be apparent in the 2D diffraction patterns (but space group forbidden reflections of the ideal equilibrium structure can still appear). Indeed, shrinkage-induced distortions to the structure have caused misidentification of the space group.¹³⁸ The original phase assignment of a BCP sample to Schwarz's P surface (space group $Pm\bar{3}m$) was in error due to the presence of the first five forbidden Bragg peaks all induced by the solvent shrinkage distortions to the double gyroid phase (space group $Ia\bar{3}d$). Space group symmetry forbidden reflections occur due to the disruption of screw axes and glide planes. When distortions occur that break such symmetries, then the strict cancellation of phases for such peaks no longer holds, and the intensity at these peak positions is evident and can be misinterpreted as resulting from allowed Bragg peaks from an undistorted alternative space group.

A suitable question then, is to ask, “how can one determine if a BCP microdomain structure is truly indeed at equilibrium?” This leads to two additional questions: (1) Is the observed phase the correct equilibrium morphology? (2) Are the metrics of the observed structure consistent with the symmetry of the unit cell, and are these metrics isotropic with respect to location within the sample (over large supra-unit cell dimensions)? The first question can be addressed by exploring the stability of a given phase to purposeful use of a preferential solvent for one block along with rapid processing to force the occurrence of a metastable phase, followed by annealing to see if the metastable phase undergoes a transformation to the equilibrium phase. This approach does not guarantee that one is studying the equilibrium phase but if a BCP can be driven into different structures by using preferential solvents for each of the blocks, followed by annealing such that each of the two (different) preferential solvent metastable structures reverts to the same phase, which strongly suggests that the annealed structure is the equilibrium one at the annealing temperature. The second question can nowadays be addressed either by employing microfocus X-ray beams and goniometer stages available at synchrotron beamlines or by using slice and view SEM to create 3D reconstructions, followed by 3D Fourier transforms. Such approaches create a 3D view of reciprocal space and permit precise determination of the locations of Bragg peaks (and their phases) for a set of single grain volumes. Only if the measurements show equivalence of symmetry-related peaks and grain independence of \mathbf{q} vectors and peak intensities can one be sure that the structure's sub- and supraunit cell dimensions are uniform and comparable to predicted equilibrium structures.

IV.B. Mapping Molecular Architectures to Multiscale Morphologies. There continues to be rapid advances in the

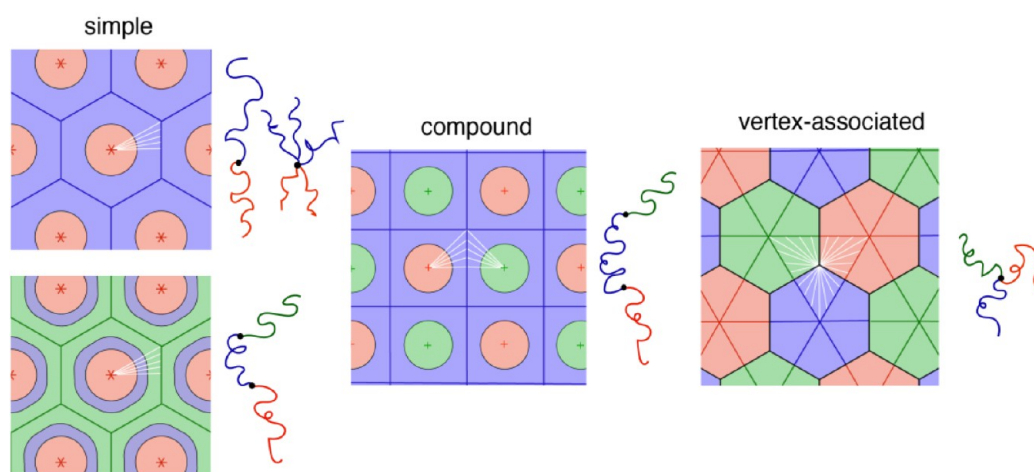


Figure 23. Subdomain geometries beyond linear diblocks. This figure illustrates 2D examples of subdomain geometries and their putative variation with molecular architecture, illustrated to the right of each. In each, terminal boundaries are illustrated as solid colored lines of corresponding blocks, and IMDSs are shown as black lines, with subdomains illustrated by regions bounded by white lines. On the left, “simple” subdomains, extend from one inner terminal boundary through one or more IMDSs to other terminal boundary. In the middle, “compound” subdomains proposed from alternating domain morphologies of AB terblocks, which extend straight from one terminal boundary (red) to an intermediate boundary (blue) where it bends toward the IMDS (and terminal boundary) of the alternate domain (green). On the right, a “vertex-associated” subdomain proposed to 2D Achimedean tiling morphologies of ABC miktoarm stars. Here, junctions are assumed to localize at the three-phase contact, and hence subdomains radiate from this line to the terminal boundaries within each domain.

ability to synthesize well-defined BCP with evermore complex architectures. The variable connectivity and additional components in more complex architectures can lead to myriad possible domain topologies, shapes and periodicities. The huge space of chemical possibilities and morphological outcomes motivates the need for rational principles that predictively map molecular characteristics to target morphologies. Considerable guidance is provided by the powerful SCFT approaches. For one, SCFT provides a means of more rapidly screening a series of systematic molecular designs (that are both synthetically accessible and as experimentally straightforward as possible) onto a morphology map, which in turn can be used to target desirable morphology dependent properties. Additionally, SCFT predictions provide a detailed “molecular microscopic” for equilibrium configurations of BCP molecules within ordered domains. Arguably as, if not more, powerful for directing the search for more interesting and valuable molecular designs and assembled morphologies are the physical principles that can be extracted from approaches like SST, since these more directly link BCP chemical properties (e.g., composition, segment–segment interactions, and architectures) to candidate morphologies via their subdomain packing thermodynamics. Such theories have the potential to identify and greatly simplify the search through multidimensional molecular design space.

One successful example of this is Milner’s mapping⁵⁷ of conformational asymmetry (i.e., asymmetric statistical lengths a_A and a_B for an assumed common volume) and architectural asymmetry (i.e., asymmetric arm number m and n) on to a single elastic asymmetry parameter for A_mB_n “miktoarm” stars. This parameter $\epsilon = (a_A/a_B)(n/m)$ characterizes the relative magnitude of the entropic stretching from B-type to A-type subdomains, in addition to their relative weighting at unequal block volumes. Critically, for $\epsilon > 1$, theory predicts that the SSL phase boundaries are shifted away from symmetry about $f = 0.5$, reflecting a thermodynamic preference of for domain curvature toward the A block, by an amount that can be achieved equally via $a_A > a_B$ in linear diblocks and $m > n$ for conformationally symmetric miktoarm stars. This prediction has been widely

confirmed,^{97,141–145} and importantly, it paves the way to vastly expanding the composition window for stable sphere and cylinder phases via high-asymmetry architectures. Beyond control of the domain topology, SST calculations lead to the predictions that the thermodynamically stable arrangement of spheres changes for large ϵ ,^{33,38,97} from the canonical case of BCC to more complex Frank–Kasper phases, like A15 and σ . It was argued that the key factor driving this transition was the change in relative stiffness of the outer (coronal) vs inner (core) subdomains, which lead to an enhanced “warping” of subdomain shapes at larger epsilon ϵ .^{33,97} SCFT studies first showed that A15 becomes stable over BCC for architecturally asymmetric BCP,⁴⁷ which was consistent with the observation of A15 sphere phases in branched dendron diblocks by Wiesner et al.³⁹ More recently, a slew of experimental observations,^{37,40,43} followed by additional SCFT studies,⁴⁹ have found that a stable window of FK phases exists for conformationally asymmetric linear diblocks as well, confirming the predicted equivalence between architectural and conformation effects. Moreover, these studies have shown that multiple sphere phases are stable at large epsilon, leading to a generic sequence of observed phases in the SSL with increasing f , BCC \rightarrow σ \rightarrow A15 \rightarrow Hex. Notably, while many aspects of the transition from stable BCC to stable FK phase (σ or A15) have been rationalized, including through the use of SST-based calculations, a complete understanding of the evolution of subdomain morphology with elastic asymmetry and its connection with this generic sequences of equilibrium phases (for the Gaussian chain melt model) remains elusive.

Given the utility of capturing a large class of molecular variation within a single (or even a few) molecular descriptor(s), it remains desirable to expand the molecular to morphology mapping provided by this SST subdomain packing perspective to a much broader class of BCP architectures. This poses two challenges, developing sufficiently accurate and flexible approaches to account for changes in the entropic cost of strongly stretched brushes beyond the simplest cases of monodisperse linear blocks, on which the parabolic brush theory is based. For example, Pickett has developed an extension

of the parabolic brush theory to account for dendritic branching of blocks and shown that it leads to qualitatively similar effects to elastic asymmetry that drive IMDS curvature away from branched domains,¹⁴⁶ and in principle, this suggests a generalization of the ϵ parameter which accounts for multiple generations of branching.⁴⁸ More broadly, the like-component brush domains of complex BCP architectures include mixtures of different “grafts”, for example, linear blocks with free ends in the brush mixed with some fraction of loops that extend into the brush but again terminate at the IMDS. SST extensions for polydisperse brushes have been developed,¹⁴⁷ but to date these have not been exploited to study the effects of “mixed grafts” on BCP morphologies and phases.

A second challenge derives from adapting the definition and associated key “degrees of freedom” with the subdomain volumes themselves to account for alterations of the molecular designs and corresponding assembled morphologies. In Figure 23, we show schematically the classes of subdomain “types” that have been explored for distinct BCP architectures thus far. The primary focus of this Perspective has been on the simplest class of subdomains, which extend in straight trajectories from one “inner” terminal boundary through the IMDS(s) to an “outer” terminal boundary. We have left out discussion of more subtle issues associated with balance of volume fraction on either side of these wedges and questions about alternate patterns of tilted and/or kinked subdomains within this class.³³ Instead, we proposed that medial sets provide a generic (zeroth order) proxy for terminal boundaries and subdomain distributions given a known IMDS shape, features which are now measurable from careful 3D reconstruction experiments. Understanding the constraints of volume “balance” for this medial ansatz and their impacts on BCP thermodynamics constitutes another open question. Beyond details associated with variation along the subdomain, we note that introducing multiblock architectures, such as ABC terpolymers, may lead to morphologies with “nonsimple” subdomains. For example, as shown in Figure 23, alternating domains morphology of ABC triblocks have been modeled by using “compound subdomains”,⁵⁸ while Archimedean tiling phases (and even so-called “tricontinuous” networks¹⁴⁸) of ABC stars have been described by “vertex associated” subdomains,^{149–151} which junctions localized to lines of three-phase contact. These examples illustrate that notions of subdomain shapes and thicknesses are inextricably linked to constraints imposed by the chain connectivity, interdomain contact, and constant density of the melt. Hence, both theoretical and experimental metrics of the 3D subdomain morphology need to be suitably tailored to account how more complex BCP architectures “fit” within more complex domain patterns.

One possible hybrid approach toward that goal may be to exploit the molecular distributions provided by SCFT to extract directly the subdomain shapes. In principle, such distributions could be extracted from the mean-field two-point correlation of SCFT solutions⁹⁸ or, alternatively, from the patterns of “segment flux” provided from the orientational order parameters, as implied by the comparison between medial and Voronoi cells to vector order. This would obviate the need for any geometric proxies, such as the medial surfaces of IMDSs, and provide direct templates for subdomain shapes for the purposes of SST analysis and potentially a detailed map for ultimate experimental characterization that could determine the 3D spatial distributions of BCP chains within complex phases. How and whether such spatially resolved subdomain orientational

maps could be extended to experimental characterization remain an open challenge.

Beyond variation of the controlled architectures in BCP for single-component melts there remain unanswered questions about subdomain packing for two experimentally important class multicomponent BCP systems: polydisperse BCP and blends of BCP with homopolymers. To begin with, polydispersity is a realistic feature of any experimental BCP system. The question of how different types of polydispersity (e.g., polydispersity in length vs composition, multimodal vs continuous distributions) influences the assembly of BCP melts is a long-standing one¹⁵² and has received considerable study from the perspective of experiments^{106,153,154} and SCFT computations.^{155–159} However, basic questions about how different modes of dispersity alter the subdomain packing characteristics remain largely open. From the point of view of SST theory, polydispersity can be expected to alter two features of BCP assembly relative to the ideal monodisperse limit. First, dispersity of blocks within the alternate brush domains alters that entropic costs of stretching in that domain. Extensions of the parabolic brush theory for planar brushes,¹⁴⁷ for example, show that dispersity leads to segregation of relative short and longer blocks into “proximal” and “distal” regions from the IMDS. Perhaps more significant from the point of view of thermodynamics, the local entropic costs of stretching are reweighted in polydisperse brushes, with proximal and distal zones respectively experiencing greater and lesser entropic costs per unit volume filled in the brush.¹²⁷ The implications of this geometric reweighting of spatial regions near to and far from the IMDS in nonlamellar morphologies remain to be understood. Moreover, it can be intuitively expected that local variations of nominal subdomain thickness of IMDS shape within a complex morphology will tend to drive segregation of distinct species of BCP distribution to regions of the complex morphology where they “fit best”. While SCFT studies have demonstrated the effect of different models of dispersity to substantially shift phase boundaries and alter domain spacing relative to the monodisperse case,^{152,157,158} a detailed understanding of the combined effects of these distinct mechanisms of subdomain stratification to stabilize complex morphologies and alter details of subdomain shapes is far from complete.

The effect of blending of homopolymers and BCP on the subdomain packing and formation of complex phases is another question of long-standing interest. Matsen and others argued that the packing frustration within the minority (tubular) phase of network-forming diblocks could be relieved by blending in homopolymers of minority block type and enhancing their stability by localizing to “hot spots” in the morphology.^{32,76} In particular, it was suggested that high molecular weight homopolymer will not mix in the tubular block but instead fill the high-stretching interstices at the center of junctions.^{30,160} This idea is seemingly consistent with SCFT calculations,^{161–163} and subsequent experimental observation,^{164,165} which show that blends with (~10–20%) homopolymer of the minority type stabilize network phases that are not equilibrium in pure diblocks, including DD and DP networks. Recently, experimental⁴² and SCFT^{166,167} studies of sphere-forming BCP systems suggest analogous effects for Frank–Kasper sphere phases. For example, blending (core block) homopolymer to diblocks which otherwise form BCC or σ phases leads to the formation of new phases, such as C14 and C15. Like the case of networks, here it has been argued, and rationalized by SCFT, that blend stability of novel sphere phase relies on inflating the

cores of highly frustrated sphere domains (e.g., the Z12 domains of C15) and relaxing the entropic costs of brush domains in their cores. Beyond these heuristic pictures, key questions remain about how blending influences subdomain packing. Foremost among these perhaps a predictive framework to describe where the “hot spots” with a complex morphology reside and how subdomain shapes of BCP evolve as one progressive loads these regions with soft guest molecules like high-MW homopolymer. That is, can one predict and map the 3D shapes of terminal boundaries that delineate between the homopolymer guests and dry molten brushes in the blended complex phases? More critical, it remains to be understood what are the geometric features of certain complex phases that make them better “hosts” than others (e.g., can these be extracted from medial analysis as in Figure 9?). It is reasonable to expect that network morphologies benefit from homopolymer loading into their junctions if those regions are indeed a primary source of packing frustration. But at present it is not yet clear why then might some phases (e.g., DD and C14) apparently benefit more from hot-spot filling such that they overtake the frustrated phases that form in unblended state (e.g., DG and σ /BCC).

V. CONCLUDING REMARKS

In this Perspective we have overviewed advances in the ability to measure and model the complex geometries of BCP assemblies, in particular focusing on features of the morphology at the subdomain scale. We conclude with a few remarks about the prospects for resolution and validation of these “fine features” of BCP morphology and their likely importance to future research.

First, we emphasized how addressing the open questions about complex BCP structure formation presents both an opportunity and a need to clearly define quantitative metrics that capture the significant variability of subdomain shapes far beyond the initial canonical domain shapes. On one hand, for all phases but that of perfect lamellar order there is variability in the packing environment of BCPs, and assessing proper metrics of this packing, and specifically metrics that are directly comparable between experimental and modeling approaches, is essential for uncovering and refining the principles that explain how the collective assembly of malleable BCP building blocks select specific domain symmetries and topologies. Beyond the grand challenge to design specific molecules for the purposes of targeting and generating yet unrealized morphologies with valuable and exotic functions (e.g., topological photonic metamaterials^{168–171}), BCP-based assembly remains critical as a laboratory for understanding the principles of self-assembled soft matter more broadly. Despite the relative simplicity of the various molecular designs, BCPs exhibit assembly behavior that is as rich in terms of the number of distinct phases as well as their structural complexity as the ever-expanding zoo of supra-molecular building blocks available to researchers, from shape-defined liquid crystalline nematogens to synthetic biopolymer hybrids.^{172,173} Yet, unlike nearly all other types of supra-molecular building blocks, the BCP assembly has the unique advantage that it is well described by broadly validated and adaptable theoretical framework (i.e., SCFT) that can trace changes in features of the molecular design to quantitative thermodynamic and structural consequences for assembly. Notably, the underlying reasons for broad success of SCFT derive from the fact that as macromolecules, the intrachain configurational fluctuations of the chains, which is readily theoretically calculable, dominates the entropic contributions in BCP, on one hand, and other hand, their effect is to “wash out”

much of the dependence of on fine chemical details of polymeric components. In that way, SCFT is broadly adaptable to a nearly limitless array of BCP architectures yielding complex and detailed assembly predictions from a fairly simplified description of molecular building blocks and their interactions. That means, for example, detailed predictions are readily accessible for not only how chain distributions in a self-assembled morphology depend on the architecture and elastic asymmetry but also how those configurations vary from place to place within a given morphology as well as from one morphology to another (see e.g. the discussion of packing in sphere-like domains at distinct Wyckoff positions in complex phases). And while questions of the role of packing frustration on the formation of complex phase are not unique to BCP melts, the powerful lens provided by SCFT (not to mention the array of particle-based simulations and theories that complement it) arguably make these systems especially valuable for careful, critical and quantitative testing of the underlying mechanisms of complex morphology selection and connecting those mechanisms to relevant design features of the molecular building blocks.

Capitalizing on the unique potential of BCPs as a laboratory for soft matter assembly will likely rely on two changes in our approach to studying BCP morphology. This first, emphasized in section II, is a shift toward more specific and quantified metrics of morphology. As is the case in many subfields of soft matter assembly, the packing geometry of BCPs is often viewed and presented as a “fuzzy” concept. Indeed, the success of SCFT for modeling BCP assembly derives essentially from the fuzziness of molecular configurations themselves, which at first glance might seem to make sharp and precise definitions of subdomain packing impossible. Yet, we emphasize that this need not be the case. While predictions of SCFT are statistical in nature, due to the underlying configurational fluctuations of chains, that does not mean it is impossible to make notions of subdomain morphology geometrically precise, quantifiable and fully generalizable to arbitrary domains. An example of this is the concept of the association map, introduced in section II.A, that divides volumes of space into distinct domains grouped together by the likelihoods of chain association to its IMDS. Even though chain ends are distributed throughout brush domains, and opposing brush regions always interpenetrate to some extent, that does not preclude definition of a sharp terminal boundary that separates neighbor domains. Once formulated, a general construction for such a boundary then leads us naturally to think about how the 3D loci of “subdomain ends” change in more complex phases. For example, this leads one to reconsider the shapes of cellular volumes enclosing sphere-like domains in complex crystalline packings (specifically those with multiple symmetry-inequivalent Wyckoff positions), which are quite distinct from the commonly invoked Voronoi cell models. Understanding the implications of what might initially seem to be subtle differences in these fine features of the morphology lies at the heart of the thermodynamic tug of war that guides their formation.

This example of terminal boundaries of BCP domains brings us to the second imperative: closing the gap between measurement and inference in complex BCP morphologies. This theme was emphasized in section III, where we noted that from the earliest days of BCP morphology characterization researchers are led to “imagine” what is the actual arrangement of molecules given what is rather limited data on the 3D structure (i.e., SAXS and TEM measurements). In many ways, the inferred “cartoon picture” about how the molecules pack in

BCP domains has not changed much over the decades, although it is important to note the methods to make morphological measurements over multilength scales and in complex 3D configurations have advanced considerably, to the point where detailed and quantitative comparisons of the theoretical predictions of the intrinsically variable fine features of morphology are within reach. That said, there are still many key attributes of BCP morphology that, while they are critical to assembly, remain essentially “invisible” from an experimental point of view.

Closing the gap between measurement and inference will ultimately rely on new methodologies that not only image the 3D shapes of the composition of materials but also resolve the distributions of constituent chains themselves within the underlying morphology. Neutron scattering of deuterium or heavy-atom-labeled BCP specimens has provided a powerful lens into the arrangement of distinct chain portions (i.e., ends and junctions) for lamellar phases.^{174,175} Notably for any nonplanar morphology, this technique will have limited use due to aforementioned unavoidable challenges posed by the phase inversion problem of the scattering pattern (and the superposition of signals from differently oriented labeled subdomain environments). That means that when it comes to knowing where the chain ends are in a complex BCP phase like the DG, experimentalists are essentially in the dark. New real-space methods that allow one to make detailed measurements of not only the IMDS but also the currently hidden terminal boundaries are needed for a critical test of principles that connect complex and malleable BCP molecules to the complex and malleable states of structure soft matter they form. Continued advances in both spatial and temporal resolution of an ever-enriched set of BCP structures in the coming years are sure to come, bringing us closer to a direct and quantitative view to imaging inhomogeneous, malleable yet nonetheless structured block copolymer chain configurations themselves hidden beneath the surface.

■ ASSOCIATED CONTENT

SI Supporting Information

The Supporting Information is available free of charge at <https://pubs.acs.org/doi/10.1021/acs.macromol.1c00958>.

Description of the medial analysis algorithm for BCP structures (PDF)

■ AUTHOR INFORMATION

Corresponding Authors

Edwin L. Thomas – Department of Materials Science and Engineering, Texas A&M University, College Station, Texas 77843, United States; Email: elt@exchange.tamu.edu

Gregory M. Grason – Department of Polymer Science and Engineering, University of Massachusetts Amherst, Amherst, Massachusetts 01003, United States; orcid.org/0000-0001-5479-9370; Email: grason@mail.pse.umass.edu

Authors

Abhiram Reddy – Department of Polymer Science and Engineering, University of Massachusetts Amherst, Amherst, Massachusetts 01003, United States

Xueyan Feng – Department of Materials Science and Engineering, Texas A&M University, College Station, Texas 77843, United States

Complete contact information is available at:

<https://pubs.acs.org/10.1021/acs.macromol.1c00958>

Notes

The authors declare no competing financial interest.

Biographies



Abhiram Reddy is a graduate student in Polymer Science and Engineering at the University of Massachusetts, Amherst. His dissertation is on understanding molecular scale mechanisms leading to geometrically complex self-assembled morphologies such as Frank–Kasper sphere packing and triply periodic network crystals from block copolymers. He received his B.S.–M.S. in physics from National Institute for Science Education and Research, Bhubaneswar, India. He was a finalist for the Frank J. Padden Jr. award for excellence in polymer physics graduate research symposium at American Physical Society’s March Meeting in 2021.



Xueyan Feng received his B.S. degree from the Department of Chemistry, University of Science and Technology of China, in 2011 and his Ph.D. degree from the Department of Polymer Science, University of Akron, under the supervision of Prof. Stephen Z. D. Cheng in 2017. His Ph.D. research topic focused on the precise synthesis and self-assembly study of functionalized giant molecules. After graduation, he continued his research as a postdoctoral researcher at Rice University and Texas A&M University under the supervision of Prof. Edwin L. Thomas. His current research topic is focused on 3D morphological characterization of complex soft matter assemblies at both the supraunit cell level and subunit cell level.



Edwin “Ned” Thomas is Professor of Materials Science and Engineering at Texas A&M University. His research is focused on structure–property relations of soft matter by using self-assembly, 2D and 3D lithography, and direct-write techniques to create metamaterials with unprecedented optical, mechanical, and thermal properties. He joined TAMU in 2020 after a career at Rice, MIT, UMassachusetts, and UMinnesota and is a member of the National Academy of Engineering and the American Academy of Arts and Sciences.



Greg Grason is Professor of Polymer Science and Engineering at University of Massachusetts Amherst. Prior to joining UMass in 2007, he earned his Ph.D. in Physics & Astronomy from the University of Pennsylvania in 2005, followed by a postdoctoral research position at UCLA. His research is on the theory of soft matter and polymeric assemblies, focusing on complex ordering in geometrically frustrated assemblies, from block copolymers to filamentous and particulate assemblies. Dr. Grason is the recipient of the National Science Foundation CAREER Award (2010) and Sloan Fellowship (2011) and was elected as Fellow of the American Physical Society in 2021. He serves on the editorial boards of *New Journal of Physics* and *GIANT*.

ACKNOWLEDGMENTS

The authors are indebted to M. Dimitriyev, M. Mahanthappa, B. Lotz, and A. Theiry for valuable discussions and useful feedback on the manuscript. We are also grateful to acknowledge A. Avgeropoulos for providing the PS–PDMS polymer used for the DD SVSEM reconstruction. The authors also acknowledge R. Spontak and H. Jinnai for sharing previously published TEMT data. This work was supported by the US Department of Energy (DOE), Office of Basic Energy Sciences, Division of Materials Sciences and Engineering, under Award DE-SC0014599.

DEDICATION

This article is dedicated to the memory of M. Kleman.

REFERENCES

- (1) Abetz, V.; Simon, P. F. W. *Block Copolymers I*; Abetz, V., Ed.; Advances in Polymer Science; Springer-Verlag: Berlin, 2005; Vol. 189.
- (2) Bates, F. S.; Hillmyer, M. A.; Lodge, T. P.; Bates, C. M.; Delaney, K. T.; Fredrickson, G. H. Multiblock Polymers: Panacea or Pandora's Box? *Science (Washington, DC, U. S.)* **2012**, *336*, 434–440.
- (3) Polymeropoulos, G.; Zapsas, G.; Ntetsikas, K.; Bilalis, P.; Gnanou, Y.; Hadjichristidis, N. 50th Anniversary Perspective: Polymers with Complex Architectures. *Macromolecules* **2017**, *50*, 1253–1290.
- (4) Bates, F. S.; Fredrickson, G. H. Block Copolymer Thermodynamics: Theory and Experiment. *Annu. Rev. Phys. Chem.* **1990**, *41*, 525–557.
- (5) Matsen, M. W. The Standard Gaussian Model for Block Copolymer Melts. *J. Phys.: Condens. Matter* **2002**, *14*, R21–R47.
- (6) Hamley, I. W. Nanotechnology with Soft Materials. *Angew. Chem., Int. Ed.* **2003**, *42*, 1692–1712.
- (7) Jackson, E. A.; Hillmyer, M. A. Nanoporous Membranes Derived from Block Copolymers: From Drug Delivery to Water Filtration. *ACS Nano* **2010**, *4*, 3548–3553.
- (8) Bates, C. M.; Maher, M. J.; Janes, D. W.; Ellison, C. J.; Willson, C. G. Block Copolymer Lithography. *Macromolecules* **2014**, *47*, 2–12.
- (9) Lodge, T. P. Block Copolymers: Long-Term Growth with Added Value. *Macromolecules* **2020**, *53*, 2–4.
- (10) Bates, C. M.; Bates, F. S. 50th Anniversary Perspective: Block Polymers—Pure Potential. *Macromolecules* **2017**, *50*, 3–22.
- (11) Skoulios, A.; Finaz, G.; Parrod, J. Obtention De Gels Mesomorphes Dans Les Melanges De Copolymeres Sequences Styrolene-Oxyde Dethylenes Avec Differentes Solvants. *C. R. Hebd. Des Seances L Acad. Des Sci.* **1960**, *251*, 739–741.
- (12) Skoulios, A.; Finaz, G. Influence De La Nature Du Solvant Sur La Structure Des Gels Mesomorphes Dun Copolymere Sequence Styrolene-Oxyde Dethylenes. *C. R. Hebd. Des Seances L Acad. Des Sci.* **1961**, *252*, 3467.
- (13) Skoulios, A.; Finaz, G. N° 58. — La Structure Des Colloïdes d'association. VII. Caractère Amphipatique et Phases Mésomorphes Des Copolymères Séquences Styrolène — Oxyde d'éthylène. *J. Chim. Phys. Phys.-Chim. Biol.* **1962**, *59*, 473–480.
- (14) Tsovaladze, G.; Skoulios, A. La Structure Des Colloïdes d'association. *J. Chim. Phys. Phys.-Chim. Biol.* **1963**, *60*, 626–633.
- (15) Matsuo, M.; Ueno, T.; Horino, H.; Chujyo, S.; Asai, H. Fine Structures and Physical Properties of Styrene-Butadiene Block Copolymers. *Polymer* **1968**, *9*, 425–436.
- (16) Hendus, H.; Illers, K.-H.; Ropte, E. Strukturuntersuchungen an Styrol-Butadien-Styrol-Blockcopolymeren. *Colloid Polym. Sci.* **1967**, *216–217*, 110–119.
- (17) Bradford, E. B.; Vanzo, E. Ordered Structures of Styrene–Butadiene Block Copolymers in the Solid State. *J. Polym. Sci., Part A-1: Polym. Chem.* **1968**, *6*, 1661–1670.
- (18) Meier, D. J. Theory of Block Copolymers. I. Domain Formation in A-B Block Copolymers. *J. Polym. Sci., Part C: Polym. Symp.* **1969**, *26*, 81–98.
- (19) Helfand, E. Theory of Inhomogeneous Polymers: Fundamentals of the Gaussian Random-walk Model. *J. Chem. Phys.* **1975**, *62*, 999–1005.
- (20) Helfand, E. Block Copolymer Theory. III. Statistical Mechanics of the Microdomain Structure. *Macromolecules* **1975**, *8*, 552–556.
- (21) Helfand, E.; Wasserman, Z. R. Block Copolymer Theory. 5. Spherical Domains. *Macromolecules* **1978**, *11*, 960–966.
- (22) Leibler, L. Theory of Microphase Separation in Block Copolymers. *Macromolecules* **1980**, *13*, 1602–1617.
- (23) Thomas, E. L.; Alward, D. B.; Kinning, D. J.; Martin, D. C.; Handlin, D. L.; Fetters, L. J. Ordered Bicontinuous Double-Diamond Structure of Star Block Copolymers: A New Equilibrium Microdomain Morphology. *Macromolecules* **1986**, *19*, 2197–2202.
- (24) Hajduk, D. A.; Harper, P. E.; Gruner, S. M.; Honeker, C. C.; Thomas, E. L.; Fetters, L. J. A Reevaluation of Bicontinuous Cubic Phases in Starblock Copolymers. *Macromolecules* **1995**, *28*, 2570–2573.

- (25) Tyler, C. A.; Qin, J.; Bates, F. S.; Morse, D. C. SCFT Study of Nonfrustrated ABC Triblock Copolymer Melts. *Macromolecules* **2007**, *40*, 4654–4668.
- (26) Tyler, C. A.; Morse, D. C. Orthorhombic Fddd Network in Triblock and Diblock Copolymer Melts. *Phys. Rev. Lett.* **2005**, *94*, 208302.
- (27) Olmsted, P. D.; Milner, S. T. Strong-Segregation Theory of Bicontinuous Phases in Block Copolymers. *Phys. Rev. Lett.* **1994**, *72*, 829–829.
- (28) Olmsted, P. D.; Milner, S. T. Strong-Segregation Theory of Bicontinuous Phases in Block Copolymers. *Phys. Rev. Lett.* **1995**, *74*, 829–829.
- (29) Olmsted, P. D.; Milner, S. T. Strong Segregation Theory of Bicontinuous Phases in Block Copolymers. *Macromolecules* **1998**, *31*, 4011–4022.
- (30) Likhhtman, A. E.; Semenov, A. N. Theory of Microphase Separation in Block Copolymer/Homopolymer Mixtures. *Macromolecules* **1997**, *30*, 7273–7278.
- (31) Semenov, A. N. Contribution to the Theory of Microphase Layering in Block-Copolymer Melts. *J. Exp. Theor. Phys.* **1985**, *88*, 1242.
- (32) Matsen, M. W.; Bates, F. S. Origins of Complex Self-Assembly in Block Copolymers. *Macromolecules* **1996**, *29*, 7641–7644.
- (33) Grason, G. M. The Packing of Soft Materials: Molecular Asymmetry, Geometric Frustration and Optimal Lattices in Block Copolymer Melts. *Phys. Rep.* **2006**, *433*, 1–64.
- (34) Shi, A.-C. Frustration in Block Copolymer Assemblies. *J. Phys.: Condens. Matter* **2021**, *33*, 253001.
- (35) Matsen, M. W.; Bates, F. S. Introduction, I. Block Copolymer Microstructures in the Intermediate-Segregation Regime. *J. Chem. Phys.* **1997**, *106*, 2436.
- (36) Thomas, E. L.; Kinning, D. J.; Alward, D. B.; Henkee, C. S. Ordered Packing Arrangements of Spherical Micelles of Diblock Copolymers in Two and Three Dimensions. *Macromolecules* **1987**, *20*, 2934–2939.
- (37) Lee, S.; Leighton, C.; Bates, F. S. Sphericity and Symmetry Breaking in the Formation of Frank–Kasper Phases from One Component Materials. *Proc. Natl. Acad. Sci. U. S. A.* **2014**, *111*, 17723–17731.
- (38) Reddy, A.; Buckley, M. B.; Arora, A.; Bates, F. S.; Dorfman, K. D.; Grason, G. M. Stable Frank–Kasper Phases of Self-Assembled, Soft Matter Spheres. *Proc. Natl. Acad. Sci. U. S. A.* **2018**, *115*, 10233–10238.
- (39) Cho, B.-K.; Jain, A.; Gruner, S. M.; Wiesner, U. Generation Dependent Mesophase Behavior in Extended Amphiphilic Dendrons in the Shape of Macromolecular Dumbbells. *Chem. Commun. (Cambridge, U. K.)* **2005**, 2143–2145.
- (40) Lee, S.; Bluemle, M. J.; Bates, F. S. Discovery of a Frank-Kasper Phase in Sphere-Forming Block Copolymer Melts. *Science (Washington, DC, U. S.)* **2010**, *330*, 349–353.
- (41) Jayaraman, A.; Zhang, D. Y.; Dewing, B. L.; Mahanthappa, M. K. Path-Dependent Preparation of Complex Micelle Packings of a Hydrated Diblock Oligomer. *ACS Cent. Sci.* **2019**, *5*, 619–628.
- (42) Mueller, A. J.; Lindsay, A. P.; Jayaraman, A.; Lodge, T. P.; Mahanthappa, M. K.; Bates, F. S. Emergence of a C15 Laves Phase in Diblock Polymer/Homopolymer Blends. *ACS Macro Lett.* **2020**, *9*, 576–582.
- (43) Bates, M. W.; Lequieu, J.; Barbon, S. M.; Lewis, R. M.; Delaney, K. T.; Anastasaki, A.; Hawker, C. J.; Fredrickson, G. H.; Bates, C. M. Stability of the A15 Phase in Diblock Copolymer Melts. *Proc. Natl. Acad. Sci. U. S. A.* **2019**, *116*, 13194–13199.
- (44) Watanabe, M.; Asai, Y.; Suzuki, J.; Takano, A.; Matsushita, Y. Frank-Kasper A15 Phase Formed in AB_n Block-Graft Copolymers with Large Numbers of Graft Chains. *Macromolecules* **2020**, *53*, 10217–10224.
- (45) Frank, F. C.; Kasper, J. S. Complex Alloy Structures Regarded as Sphere Packings. II. Analysis and Classification of Representative Structures. *Acta Crystallogr.* **1959**, *12*, 483–499.
- (46) Shoemaker, D. P.; Shoemaker, C. B. Concerning the Relative Numbers of Atomic Coordination Types in Tetrahedrally Close Packed Metal Structures. *Acta Crystallogr., Sect. B: Struct. Sci.* **1986**, *42*, 3–11.
- (47) Grason, G. M.; DiDonna, B. A.; Kamien, R. D. Geometric Theory of Diblock Copolymer Phases. *Phys. Rev. Lett.* **2003**, *91*, 058304.
- (48) Grason, G.; Kamien, R. Self-Consistent Field Theory of Multiply Branched Block Copolymer Melts. *Phys. Rev. E* **2005**, *71*, 051801.
- (49) Xie, N.; Li, W.; Qiu, F.; Shi, A.-C. σ Phase Formed in Conformationally Asymmetric AB-Type Block Copolymers. *ACS Macro Lett.* **2014**, *3*, 906–910.
- (50) Arora, A.; Qin, J.; Morse, D. C.; Delaney, K. T.; Fredrickson, G. H.; Bates, F. S.; Dorfman, K. D. Broadly Accessible Self-Consistent Field Theory for Block Polymer Materials Discovery. *Macromolecules* **2016**, *49*, 4675–4690.
- (51) Goveas, J. L.; Milner, S. T.; Russel, W. B. Corrections to Strong-Stretching Theories. *Macromolecules* **1997**, *30*, 5541–5552.
- (52) Matsen, M. W. Strong-Segregation Limit of the Self-Consistent Field Theory for Diblock Copolymer Melts. *Eur. Phys. J. E: Soft Matter Biol. Phys.* **2010**, *33*, 297.
- (53) Likhhtman, A. E.; Semenov, A. N. Stability of the OBDD Structure for Diblock Copolymer Melts in the Strong Segregation Limit. *Macromolecules* **1994**, *27*, 3103–3106.
- (54) Likhhtman, A. E.; Semenov, A. N. An Advance in the Theory of Strongly Segregated Polymers. *Europhys. Lett.* **2000**, *51*, 307–313.
- (55) Matsen, M. W.; Barrett, C. Liquid-Crystalline Behavior of Rod-Coil Diblock Copolymers. *J. Chem. Phys.* **1998**, *109*, 4108.
- (56) Floudas, G.; Hadjichristidis, N.; Stamm, M.; Likhhtman, A. E.; Semenov, A. N. Microphase Separation in Block Copolymer/Homopolymer Blends: Theory and Experiment. *J. Chem. Phys.* **1997**, *106*, 3318–3328.
- (57) Milner, S. T. Chain Architecture and Asymmetry in Copolymer Microphases. *Macromolecules* **1994**, *27*, 2333–2335.
- (58) Phan, S.; Fredrickson, G. H. Morphology of Symmetric ABC Triblock Copolymers in the Strong Segregation Limit. *Macromolecules* **1998**, *31*, 59–63.
- (59) Witten, T. A.; Leibler, L.; Pincus, P. A. Stress Relaxation in the Lamellar Copolymer Mesophase. *Macromolecules* **1990**, *23*, 824–829.
- (60) Matsen, M. W.; Schick, M. Stable and Unstable Phases of a Diblock Copolymer Melt. *Phys. Rev. Lett.* **1994**, *72*, 2660–2663.
- (61) Kamien, R. D. The Geometry of Soft Materials: A Primer. *Rev. Mod. Phys.* **2002**, *74*, 953–971.
- (62) Hyde, S.; Ninham, B. W.; Andersson, S.; Larsson, K. K.; Landh, T.; Blum, Z.; Lidin, S. Mathematics of Curvature. In *The Language of Shape*; Elsevier: Amsterdam, 1997; pp 1–41.
- (63) Lambert, C.; Radzilowski, L.; Thomas, E. Triply Periodic Level Surfaces as Models for Cubic Tricontinuous Block Copolymer Morphologies. *Philos. Trans. R. Soc. A* **1996**, *354*, 2009–2023.
- (64) Schick, M. Avatars of the Gyroid. *Phys. A* **1998**, *251*, 1–11.
- (65) Wohlgemuth, M.; Yufa, N.; Hoffman, J.; Thomas, E. L. Triply Periodic Bicontinuous Cubic Microdomain Morphologies by Symmetries. *Macromolecules* **2001**, *34*, 6083–6089.
- (66) Thomas, E. L.; Anderson, D. M.; Henkee, C. S.; Hoffman, D. Periodic Area-Minimizing Surfaces in Block Copolymers. *Nature* **1988**, *334*, 598–601.
- (67) Schoen, A. H. Reflections Concerning Triply-Periodic Minimal Surfaces. *Interface Focus* **2012**, *2*, 658–668.
- (68) Lord, E. A.; Mackay, A. L. Periodic Minimal Surfaces of Cubic Symmetry. *Curr. Sci.*, **2003**.
- (69) Grosse-Brauckmann, K. On Gyroid Interfaces. *J. Colloid Interface Sci.* **1997**, *187*, 418.
- (70) Große-Brauckmann, K. Gyroids of Constant Mean Curvature. *Exp. Math.* **1997**, *6*, 33.
- (71) Anderson, D. M.; Davis, H. T.; Nitsche, J. C. C.; Scriven, L. E. Periodic Surfaces of Prescribed Mean Curvature. In *Advance in Chemical Physics*; Prigogine, I., Rice, S. A., Eds.; John Wiley & Sons, Inc.: 1990; pp 337–396.
- (72) Hyde, S.; Ninham, B. W.; Andersson, S.; Larsson, K.; Landh, T.; Blum, Z.; Lidin, S. Beyond Flatland: The Geometric Forms Due to Self-Assembly. In *The Language of Shape*; Elsevier: Amsterdam, 1997; pp 141–197.
- (73) Schröder-Turk, G. E.; Fogden, A.; Hyde, S. T. Bicontinuous Geometries and Molecular Self-Assembly: Comparison of Local

- Curvature and Global Packing Variations in Genus-Three Cubic, Tetragonal and Rhombohedral Surfaces. *Eur. Phys. J. B* **2006**, *54*, 509–524.
- (74) Prasad, I.; Jinnai, H.; Ho, R.-M. M.; Thomas, E. L.; Grason, G. M. Anatomy of Triply-Periodic Network Assemblies: Characterizing Skeletal and Inter-Domain Surface Geometry of Block Copolymer Gyroids. *Soft Matter* **2018**, *14*, 3612–3623.
- (75) DiDonna, B. A.; Kamien, R. D. Smectic Blue Phases: Layered Systems with High Intrinsic Curvature. *Phys. Rev. E: Stat. Phys., Plasmas, Fluids, Relat. Interdiscip. Top.* **2003**, *68*, 041703.
- (76) Matsen, M. W.; Bates, F. S. Block Copolymer Microstructures in the Intermediate-Segregation Regime. *J. Chem. Phys.* **1997**, *106*, 2436.
- (77) Jinnai, H.; Nishikawa, Y.; Spontak, R. J.; Smith, S. D.; Agard, D. A.; Hashimoto, T. Direct Measurement of Interfacial Curvature Distributions in a Bicontinuous Block Copolymer Morphology. *Phys. Rev. Lett.* **2000**, *84*, 518–521.
- (78) Feng, X.; Burke, C. J.; Zhuo, M.; Guo, H.; Yang, K.; Reddy, A.; Prasad, I.; Ho, R.-M.; Avgeropoulos, A.; Grason, G. M.; et al. Seeing Mesoatomic Distortions in Soft-Matter Crystals of a Double-Gyroid Block Copolymer. *Nature* **2019**, *575*, 175–179.
- (79) Milner, S. T.; Witten, T. A.; Cates, M. E. Theory of the Grafted Polymer Brush. *Macromolecules* **1988**, *21*, 2610–2619.
- (80) Blum, H. Biological Shape and Visual Science (Part I). *J. Theor. Biol.* **1973**, *38*, 205–287.
- (81) Nackman, L. R.; Pizer, S. M. Three-Dimensional Shape Description Using the Symmetric Axis Transform I: Theory. *IEEE Trans. Pattern Anal. Mach. Intell.* **1985**, *PAMI-7*, 187–202.
- (82) *Medial Representations: Mathematics, Algorithms and Applications*; Siddiqi, K., Pizer, S. M., Eds.; Springer Scientific: Berlin, 2008.
- (83) Nackman, L. R. Curvature Relations in Three-Dimensional Symmetric Axes. *Comput. Graph. Image Process.* **1982**, *20*, 43–57.
- (84) Schröder, G. E.; Ramsden, S. J.; Christy, A. G.; Hyde, S. T. Medial Surfaces of Hyperbolic Structures. *Eur. Phys. J. B* **2003**, *35*, 551.
- (85) Chen, H.; Jin, C. Competition Brings out the Best: Modelling the Frustration between Curvature Energy and Chain Stretching Energy of Lyotropic Liquid Crystals in Bicontinuous Cubic Phases. *Interface Focus* **2017**, *7*, 20160114.
- (86) Wells, A. F. *Three-Dimensional Nets and Polyhedra*; Wiley: New York, 1977.
- (87) Fredrickson, G. H. Noncircular Wigner-Seitz Cells in Strongly Segregated Block Copolymers. *Macromolecules* **1993**, *26*, 4351–4355.
- (88) Du, Q.; Faber, V.; Gunzburger, M. Centroidal Voronoi Tessellations: Applications and Algorithms. *SIAM Rev.* **1999**, *41*, 637–676.
- (89) Balagurusamy, V. S. K.; Ungar, G.; Percec, V.; Johansson, G. Rational Design of the First Spherical Supramolecular Dendrimers Self-Organized in a Novel Thermotropic Cubic Liquid-Crystalline Phase and the Determination of Their Shape by X-Ray Analysis. *J. Am. Chem. Soc.* **1997**, *119*, 1539–1555.
- (90) Zeng, X.; Ungar, G.; Liu, Y.; Percec, V.; Dulcey, A. E.; Hobbs, J. K. Supramolecular dendritic liquid quasicrystals. *Nature* **2004**, *428*, 157–160.
- (91) Huang, M.; Hsu, C.-H.; Wang, J.; Mei, S.; Dong, X.; Li, Y.; Li, M.; Liu, H.; Zhang, W.; Aida, T.; Zhang, W.-B.; Yue, K.; Cheng, S. Z. D. Selective Assemblies of Giant Tetrahedra via Precisely Controlled Positional Interactions. *Science (Washington, DC, U. S.)* **2015**, *348*, 424.
- (92) Kim, S. A.; Jeong, K.-J.; Yethiraj, A.; Mahanthappa, M. K. Low-Symmetry Sphere Packings of Simple Surfactant Micelles Induced by Ionic Sphericity. *Proc. Natl. Acad. Sci. U. S. A.* **2017**, *114*, 4072.
- (93) Nelson, D. R.; Spaepen, F. Polytetrahedral Order in Condensed Matter. *Solid State Phys.* **1989**, *42*, 1–90.
- (94) Zihler, P.; Kamien, R. D. Maximizing Entropy by Minimizing Area: Towards a New Principle of Self-Organization. *J. Phys. Chem. B* **2001**, *105*, 10147–10158.
- (95) Reddy, A.; Grason, G. M. A Cornerstone of Complex Crystals. *Nat. Chem.* **2019**, *11*, 865–867.
- (96) van Reuth, E. C.; Waterstrat, R. M. Atomic Ordering in Binary A L5-Type Phases. *Acta Crystallogr., Sect. B: Struct. Crystallogr. Cryst. Chem.* **1968**, *24*, 186–196.
- (97) Grason, G. M.; Kamien, R. D. *Interfaces in Diblocks: A Study of Mikroarm Copolymers*, 2004.
- (98) Prasad, I.; Seo, Y.; Hall, L. M.; Grason, G. M. Intradomain Textures in Block Copolymers: Multizone Alignment and Biaxiality. *Phys. Rev. Lett.* **2017**, *118*, 247801.
- (99) Szwarc, M.; Levy, M.; Milkovich, R. Polymerization Initiated by Electron Transfer to Monomer. A New Method of Formation of Block Polymers I. *J. Am. Chem. Soc.* **1956**, *78*, 2656–2657.
- (100) Richards, D. H.; Szwarc, M. Block Polymers of Ethylene Oxide and Its Analogues with Styrene. *Trans. Faraday Soc.* **1959**, *55*, 1644.
- (101) Skoulios, A. *Adv. Liq. Cryst.* **1975**, *1*, 169–188.
- (102) Vanzo, E. Ordered Structures of Styrene–Butadiene Block Copolymers. *J. Polym. Sci., Part A-1: Polym. Chem.* **1966**, *4*, 1727–1730.
- (103) Fink, Y.; Urbas, A. M.; Bawendi, M. G.; Joannopoulos, J. D.; Thomas, E. L. Block Copolymers as Photonic Bandgap Materials. *J. Lightwave Technol.* **1999**, *17*, 1963–1969.
- (104) Kato, K. Osmium Tetroxide Fixation of Rubber Latices. *J. Polym. Sci., Part B: Polym. Lett.* **1966**, *4*, 35–38.
- (105) Matsuo, M.; Sagae, S.; Asai, H. Fine Structures of Styrene-Butadiene Block Copolymer Films Cast from Toluene Solution. *Polymer* **1969**, *10*, 79–87.
- (106) Matsushita, Y.; Mori, K.; Saguchi, R.; Nakao, Y.; Noda, I.; Nagasawa, M. Molecular Weight Dependence of Lamellar Domain Spacing of Diblock Copolymers in Bulk. *Macromolecules* **1990**, *23*, 4313–4316.
- (107) Hashimoto, T.; Tanaka, H.; Hasegawa, H. Ordered Structure in Mixtures of a Block Copolymer and Homopolymers. 2. Effects of Molecular Weights of Homopolymers. *Macromolecules* **1990**, *23*, 4378–4386.
- (108) Ohta, T.; Kawasaki, K. Equilibrium Morphology of Block Copolymer Melts. *Macromolecules* **1986**, *19*, 2621–2632.
- (109) Alward, D. B.; Kinning, D. J.; Thomas, E. L.; Fetters, L. J. Effect of Arm Number and Arm Molecular Weight on the Solid-State Morphology of Poly(Styrene-Isoprene) Star Block Copolymers. *Macromolecules* **1986**, *19*, 215–224.
- (110) Kinning, D. J.; Thomas, E. L.; Alward, D. B.; Fetters, L. J.; Handlin, D. L. Sharpness of the Functionality-Induced Structural Transition in Poly(Styrene-Isoprene) Star Block Copolymers. *Macromolecules* **1986**, *19*, 1288–1290.
- (111) Longley, W.; McIntosh, T. J. A Bicontinuous Tetrahedral Structure in a Liquid-Crystalline Lipid. *Nature* **1983**, *303*, 612–614.
- (112) Hajduk, D. A.; Harper, P. E.; Gruner, S. M.; Honeker, C. C.; Kim, G.; Thomas, E. L.; Fetters, L. J. The Gyroid: A New Equilibrium Morphology in Weakly Segregated Diblock Copolymers. *Macromolecules* **1994**, *27*, 4063–4075.
- (113) Hoffman, D.; Hoffman, J. TEMSim Volume Projections.
- (114) Cochran, E. W.; Garcia-cervera, C. J.; Fredrickson, G. H. Stability of the Gyroid Phase in Diblock Copolymers at Strong Segregation. *Macromolecules* **2006**, *39*, 2449–2451.
- (115) Momma, K.; Izumi, F. VESTA 3 for Three-Dimensional Visualization of Crystal, Volumetric and Morphology Data. *J. Appl. Crystallogr.* **2011**, *44*, 1272–1276.
- (116) Jiang, Z.; Lee, B. Recent Advances in Small Angle X-Ray Scattering for Superlattice Study. *Appl. Phys. Rev.* **2021**, *8*, 011305.
- (117) Elser, V. Phase Retrieval by Iterated Projections. *J. Opt. Soc. Am. A* **2003**, *20*, 40.
- (118) Elser, V.; Lan, T.-Y.; Bendory, T. Benchmark Problems for Phase Retrieval. *SIAM J. Imaging Sci.* **2018**, *11*, 2429–2455.
- (119) Palatinus, L.; Chapis, G. SUPERFLIP – a Computer Program for the Solution of Crystal Structures by Charge Flipping in Arbitrary Dimensions. *J. Appl. Crystallogr.* **2007**, *40*, 786–790.
- (120) Jeon, S.; Jun, T.; Jo, S.; Ahn, H.; Lee, S.; Lee, B.; Ryu, D. Y. Frank–Kasper Phases Identified in PDMS- b -PTFEA Copolymers with High Conformational Asymmetry. *Macromol. Rapid Commun.* **2019**, *40*, 1900259.
- (121) Spontak, R. J.; Williams, M. C.; Agard, D. A. Three-Dimensional Study of Cylindrical Morphology in a Styrene-Butadiene-Styrene Block Copolymer. *Polymer* **1988**, *29*, 387–395.

- (122) Spontak, R. J.; Fung, J. C.; Braunfeld, M. B.; Sedat, J. W.; Agard, D. A.; Kane, L.; Smith, S. D.; Satkowski, M. M.; Ashraf, A.; Hajduk, D. A.; et al. Phase Behavior of Ordered Diblock Copolymer Blends: Effect of Compositional Heterogeneity. *Macromolecules* **1996**, *29*, 4494–4507.
- (123) Laurer, J. H.; Hajduk, D. A.; Fung, J. C.; Sedat, J. W.; Smith, S. D.; Gruner, S. M.; Agard, D. A.; Spontak, R. J. Microstructural Analysis of a Cubic Bicontinuous Morphology in a Neat SIS Triblock Copolymer. *Macromolecules* **1997**, *30*, 3938–3941.
- (124) *Electron Tomography: Three-Dimensional Imaging with the Transmission Electron Microscope*; Frank, J., Ed.; Plenum: New York, 1992.
- (125) Jinnai, H.; Spontak, R. J.; Nishi, T. Transmission Electron Microtomography and Polymer Nanostructures. *Macromolecules* **2010**, *43*, 1675–1688.
- (126) Jinnai, H.; Kajihara, T.; Watashiba, H.; Nishikawa, Y.; Spontak, R. J. Interfacial and Topological Measurements of Bicontinuous Polymer Morphologies. *Phys. Rev. E: Stat. Phys., Plasmas, Fluids, Relat. Interdiscip. Top.* **2001**, *64*, 018003.
- (127) Takagi, W.; Suzuki, J.; Aoyama, Y.; Mihira, T.; Takano, A.; Matsushita, Y. Bicontinuous Double-Diamond Structures Formed in Ternary Blends of AB Diblock Copolymers with Block Chains of Different Lengths. *Macromolecules* **2019**, *52*, 6633–6640.
- (128) Chu, C. Y.; Jiang, X.; Jinnai, H.; Pei, R. Y.; Lin, W. F.; Tsai, J. C.; Chen, H. L. Real-Space Evidence of the Equilibrium Ordered Bicontinuous Double Diamond Structure of a Diblock Copolymer. *Soft Matter* **2015**, *11*, 1871–1876.
- (129) Wang, Y.-C.; Inoue, A.; Hasegawa, H.; Takenaka, M. The Formation of OTDD Network Structure in PS-*b*-PI-*b*-PDMS Triblock Terpolymer. *Macromol. Chem. Phys.* **2017**, *218*, 1700008.
- (130) Feng, X.; Guo, H.; Thomas, E. L. Topological Defects in Tubular Network Block Copolymers. *Polymer* **2019**, *168*, 44–52.
- (131) Feng, X.; Zhuo, M.; Guo, H.; Thomas, E. L. Visualizing the Double-Gyroid Twin. *Proc. Natl. Acad. Sci. U. S. A.* **2021**, *118*, e2018977118.
- (132) Chang, C.-Y.; Manesi, G.-M.; Yang, C.-Y.; Hung, Y.-C.; Yang, K.-C.; Chiu, P.-T.; Avgeropoulos, A.; Ho, R.-M. Mesoscale Networks and Corresponding Transitions from Self-Assembly of Block Copolymers. *Proc. Natl. Acad. Sci. U. S. A.* **2021**, *118*, e2022275118.
- (133) Ouk Kim, S.; Solak, H. H.; Stoykovich, M. P.; Ferrier, N. J.; de Pablo, J. J.; Nealey, P. F. Epitaxial Self-Assembly of Block Copolymers on Lithographically Defined Nanopatterned Substrates. *Nature* **2003**, *424*, 411–414.
- (134) Ruiz, R.; Kang, H.; Detcheverry, F. A.; Dobisz, E.; Kercher, D. S.; Albrecht, T. R.; de Pablo, J. J.; Nealey, P. F. Density Multiplication and Improved Lithography by Directed Block Copolymer Assembly. *Science (Washington, DC, U. S.)* **2008**, *321*, 936–939.
- (135) Stoykovich, M. P. Directed Assembly of Block Copolymer Blends into Nonregular Device-Oriented Structures. *Science (Washington, DC, U. S.)* **2005**, *308*, 1442–1446.
- (136) Hu, H.; Gopinadhan, M.; Osuji, C. O. Directed Self-Assembly of Block Copolymers: A Tutorial Review of Strategies for Enabling Nanotechnology with Soft Matter. *Soft Matter* **2014**, *10*, 3867.
- (137) Hanley, K. J.; Lodge, T. P.; Huang, C.-I. Phase Behavior of a Block Copolymer in Solvents of Varying Selectivity. *Macromolecules* **2000**, *33*, 5918–5931.
- (138) Toombes, G. E. S.; Finnefrock, A. C.; Tate, M. W.; Ulrich, R.; Wiesner, U.; Gruner, S. M. A Re-Evaluation of the Morphology of a Bicontinuous Block Copolymer-Ceramic Material. *Macromolecules* **2007**, *40*, 8974.
- (139) Faber, M.; Hofman, A. H.; Loos, K.; ten Brinke, G. Highly Ordered Structure Formation in RAFT-Synthesized PtBOS-*b*-P4VP Diblock Copolymers. *Macromol. Rapid Commun.* **2016**, *37*, 911–919.
- (140) Dolan, J. A.; Korzeb, K.; Dehmel, R.; Gödel, K. C.; Stefik, M.; Wiesner, U.; Wilkinson, T. D.; Baumberg, J. J.; Wilts, B. D.; Steiner, U.; et al. Controlling Self-Assembly in Gyroid Terpolymer Films By Solvent Vapor Annealing. *Small* **2018**, *14*, 1802401.
- (141) Gido, S. P.; Lee, C.; Pochan, D. J.; Pispas, S.; Mays, J. W.; Hadjichristidis, N. Synthesis, Characterization, and Morphology of Model Graft Copolymers with Trifunctional Branch Points. *Macromolecules* **1996**, *29*, 7022–7028.
- (142) Pochan, D. J.; Gido, S. P.; Pispas, S.; Mays, J. W.; Ryan, A. J.; Fairclough, J. P. A.; Hamley, I. W.; Terrill, N. J. Morphologies of Microphase-Separated A₂B Simple Graft Copolymers. *Macromolecules* **1996**, *29*, 5091–5098.
- (143) Gido, S. P.; Wang, Z. G. Interfacial Curvature in Graft and Diblock Copolymers and Implications for Long-Range Order in Cylindrical Morphologies. *Macromolecules* **1997**, *30*, 6771.
- (144) Matsen, M. W. Effect of Architecture on the Phase Behavior of AB-Type Block Copolymer Melts. *Macromolecules* **2012**, *45*, 2161–2165.
- (145) Bates, M. W.; Barbon, S. M.; Levi, A. E.; Lewis, R. M.; Beech, H. K.; Vonk, K. M.; Zhang, C.; Fredrickson, G. H.; Hawker, C. J.; Bates, C. M. Synthesis and Self-Assembly of AB_n Miktoarm Star Polymers. *ACS Macro Lett.* **2020**, *9*, 396–403.
- (146) Pickett, G. T. *Macromolecules* **2002**, *35*, 1896–1904.
- (147) Milner, S. T.; Witten, T. A.; Cates, M. E. Effects of Polydispersity in the End-Grafted Polymer Brush. *Macromolecules* **1989**, *22*, 853–861.
- (148) Fischer, M. G.; de Campo, L.; Kirkensgaard, J. J. K.; Hyde, S. T.; Schröder-Turk, G. E. The Tricontinuous 3 Ths (5) Phase: A New Morphology in Copolymer Melts. *Macromolecules* **2014**, *47*, 7424–7430.
- (149) Dotera, T. Cell Crystals: Kelvin's Polyhedra in Block Copolymer Melts. *Phys. Rev. Lett.* **1999**, *82*, 105–108.
- (150) Takano, A.; Kawashima, W.; Noro, A.; Isono, Y.; Tanaka, N.; Dotera, T.; Matsushita, Y. A Mesoscopic Archimedean Tiling Having a New Complexity in an ABC Star Polymer. *J. Polym. Sci., Part B: Polym. Phys.* **2005**, *43*, 2427–2432.
- (151) Matsushita, Y.; Hayashida, K.; Dotera, T.; Takano, A. Kaleidoscopic Morphologies from ABC Star-Shaped Terpolymers. *J. Phys.: Condens. Matter* **2011**, *23*, 284111.
- (152) Lynd, N. A.; Meuler, A. J.; Hillmyer, M. A. Polydispersity and Block Copolymer Self-Assembly. *Prog. Polym. Sci.* **2008**, *33*, 875–893.
- (153) Lynd, N. A.; Hillmyer, M. A. Effects of Polydispersity on the Order–Disorder Transition in Block Copolymer Melts. *Macromolecules* **2007**, *40*, 8050–8055.
- (154) Noro, A.; Cho, D.; Takano, A.; Matsushita, Y. Effect of Molecular Weight Distribution on Microphase-Separated Structures from Block Copolymers. *Macromolecules* **2005**, *38*, 4371–4376.
- (155) Burger, C.; Ruland, W.; Semenov, A. N. Polydispersity Effects on the Microphase-Separation Transition in Block Copolymers. *Macromolecules* **1990**, *23*, 3339–3346.
- (156) Lynd, N. A.; Hillmyer, M. A.; Matsen, M. W. Theory of Polydisperse Block Copolymer Melts: Beyond the Schulz–Zimm Distribution. *Macromolecules* **2008**, *41*, 4531–4533.
- (157) Cooke, D. M.; Shi, A.-C. Effects of Polydispersity on Phase Behavior of Diblock Copolymers. *Macromolecules* **2006**, *39*, 6661–6671.
- (158) Matsen, M. W. Effect of Large Degrees of Polydispersity on Strongly Segregated Block Copolymers. *Eur. Phys. J. E: Soft Matter Biol. Phys.* **2006**, *21*, 199–207.
- (159) Sides, S. W.; Fredrickson, G. H. Continuous Polydispersity in a Self-Consistent Field Theory for Diblock Copolymers. *J. Chem. Phys.* **2004**, *121*, 4974–4986.
- (160) Belyi, V. A. Exclusion Zone of Convex Brushes in the Strong-Stretching Limit. *J. Chem. Phys.* **2004**, *121*, 6547–6554.
- (161) Matsen, M. W. Stabilizing New Morphologies by Blending Homopolymer with Block Copolymer. *Phys. Rev. Lett.* **1995**, *74*, 4225–4228.
- (162) Matsen, M. W. Phase Behavior of Block Copolymer/Homopolymer Blends. *Macromolecules* **1995**, *28*, 5765–5773.
- (163) Martinez-Veracoechea, F. J.; Escobedo, F. A. The Plumber's Nightmare Phase in Diblock Copolymer/Homopolymer Blends. A Self-Consistent Field Theory Study. *Macromolecules* **2009**, *42*, 9058–9062.

- (164) Takagi, H.; Yamamoto, K.; Okamoto, S. Ordered-Bicontinuous-Double-Diamond Structure in Block Copolymer/Homopolymer Blends. *EPL (Europhysics Lett.)* **2015**, *110*, 48003.
- (165) Takagi, H.; Takasaki, T.; Yamamoto, K. Phase Diagram for Block Copolymer and Homopolymer Blends: The Phase Boundary of the Ordered Bicontinuous Double Diamond Network Structure. *J. Nanosci. Nanotechnol.* **2017**, *17*, 9009–9014.
- (166) Cheong, G. K.; Bates, F. S.; Dorfman, K. D. Symmetry Breaking in Particle-Forming Diblock Polymer/Homopolymer Blends. *Proc. Natl. Acad. Sci. U. S. A.* **2020**, *117*, 16764–16769.
- (167) Xie, J.; Shi, A.-C. Formation of Complex Spherical Packing Phases in Diblock Copolymer/Homopolymer Blends. *Giant* **2021**, *5*, 100043.
- (168) Lu, L.; Fu, L.; Joannopoulos, J. D.; Soljačić, M. Weyl Points and Line Nodes in Gyroid Photonic Crystals. *Nat. Photonics* **2013**, *7*, 294–299.
- (169) Lu, L.; Wang, Z.; Ye, D.; Ran, L.; Fu, L.; Joannopoulos, J. D.; Soljačić, M. Experimental Observation of Weyl Points. *Science (Washington, DC, U. S.)* **2015**, *349*, 622–624.
- (170) Rechtsman, M. C.; Zeuner, J. M.; Plotnik, Y.; Lumer, Y.; Podolsky, D.; Dreisow, F.; Nolte, S.; Segev, M.; Szameit, A. Photonic Floquet Topological Insulators. *Nature* **2013**, *496*, 196–200.
- (171) Fruchart, M.; Jeon, S.-Y. Y.; Hur, K.; Cheianov, V.; Wiesner, U.; Vitelli, V. Soft Self-Assembly of Weyl Materials for Light and Sound. *Proc. Natl. Acad. Sci. U. S. A.* **2018**, *115*, E3655–E3664.
- (172) Zhang, W.-B.; Yu, X.; Wang, C.-L.; Sun, H.-J.; Hsieh, I.-F.; Li, Y.; Dong, X.-H.; Yue, K.; Van Horn, R.; Cheng, S. Z. D. Molecular Nanoparticles Are Unique Elements for Macromolecular Science: From “Nanoatoms” to Giant Molecules. *Macromolecules* **2014**, *47*, 1221–1239.
- (173) Su, Z.; Zhang, R.; Yan, X.-Y.; Guo, Q.-Y.; Huang, J.; Shan, W.; Liu, Y.; Liu, T.; Huang, M.; Cheng, S. Z. D. The Role of Architectural Engineering in Macromolecular Self-Assemblies via Non-Covalent Interactions: A Molecular LEGO Approach. *Prog. Polym. Sci.* **2020**, *103*, 101230.
- (174) Matsushita, Y.; Mori, K.; Mogi, Y.; Saguchi, R.; Noda, I.; Nagasawa, M.; Chang, T.; Glinka, C. J.; Han, C. C. Chain Conformation of a Block Polymer in a Microphase-Separated Structure. *Macromolecules* **1990**, *23*, 4317–4321.
- (175) Mayes, A. M.; Russell, T. P.; Deline, V. R.; Satija, S. K.; Majkrzak, C. F. Block Copolymer Mixtures As Revealed By Neutron Reflectivity. *Macromolecules* **1994**, *27*, 7447–7453.